DYNAMIC INVESTIGATION OF VIBRATORY SCREEN RESPONSE IN A FEM ENVIRONMENT

by **Robert Oliver Harat**

Submitted in partial fulfilment of the requirements for the degree

Master's in Mechanical Engineering

in the

Department of Mechanical and Aeronautical Engineering

Faculty of Engineering, Built Environment and Information Technology

University of Pretoria

August 2020

ABSTRACT

DYNAMIC INVESTIGATIONS OF A VIBRATORY SCREEN IN A FEM ENVIRONMENT

by

Robert Oliver Harat

Supervisor:	Prof. P. Stephan Heyns
Department:	Mechanical and Aeronautical Engineering
University:	University of Pretoria
Degree:	Masters in Mechanical Engineering

Keywords: Vibratory screens; Fault detection; FEM; Modal analysis

Effective models of vibratory screens which can capture the true response characteristics are crucial in the understanding of faults and failures which occur in vibratory screens. However, the current available models are usually simplified and have limited validation to that of a physical screen.

Much research has been conducted to optimise the screening efficiency of screens. The optimisation includes screen geometry, material processing of the screen and the dynamic response of the screen. These investigations have not been furthered to investigate the effects of different faults on the dynamic response of a vibratory screen.

To model a vibratory screen which can replicate the dynamics of a physical vibratory screen it is important to create a model with enough complexity to capture the dynamics of the screen. The model of the screen was validated using both modal analysis and the transient response of the screen.

The modal analysis was used to ensure that the physical characteristics of the model are consistent with that of the physical screen. Once this was completed, the second validation aimed to investigate if the model of the screen could capture transient faults which are measured experimentally. It was found that it was not possible to conclusively determine if the finite element methods model could

Finally, an intelligent method was used to distinguishing between different faults and classifying them accordingly. The intelligent method was also trained using the FEM data and then used to classify the physical screen data.

ACKNOWLEDGMENTS

I would like to acknowledge and thank the following people and organisations:

- Prof. PS Heyns for providing me with the opportunity to further my knowledge in the field under his supervision.
- Mr. Gary Styger for his support and sharing his experience.
- Mr. George Breitenbach and Mr. Herman Booysen for their assistance in the experimental set-up and during the implementation of the experiments.
- Ms. Bonolo Mokoka for her administrative support.

Table of Contents

Nomenclature

English Symbols

Symbol	Name	Unit
A	Area	m^2
c	Damping coefficient	$kg{\cdot}m^{-1}{\cdot}s^{-1}$
C_1 or c_{10}	Material constant	$kg{\cdot}\ m^{-1}\ {\cdot}s^{-2}$
C_2 or c_{01}	Material constant	$kg{\cdot}\ m^{-1}\ {\cdot}s^{-2}$
$c_{eq,normal}$	Equivalent damping in the normal direction	$kg{\cdot}m^{-1}{\cdot}s^{-1}$
$c_{eq,shear}$	Equivalent damping in the shear direction	$kg{\cdot}m^{-1}{\cdot}s^{-1}$
c_{eq}	Equivalent damping coefficient	$kg{\cdot}m^{-1}{\cdot}s^{-1}$
F	Force	$kg{\cdot}\ m\ {\cdot}s^{-2}$
$f(t)$	Force as a function of time	$kg{\cdot}\ m\ {\cdot}s^{-2}$
ΔF	Change in force	$kg{\cdot}\ m\ {\cdot}s^{-2}$
G	Shear modulus	kg· m-1 ·s-2
k	Stiffness coefficient	$kg{\cdot}s^{-2}$
k_1	First order stiffness	$kg{\cdot}s^{-2}$
k_2	Second order stiffness	$kg{\cdot}s^{-2}$
k_3	Third order stiffness	$kg{\cdot}s^{-2}$
k_{normal}	Stiffness in normal direction	$kg{\cdot}s^{-2}$
k_{shear}	Stiffness in shear direction	$kg{\cdot}s^{-2}$
l	Stretched spring length	m
l_0	Unstretched spring length	m
Δl	Change in length	m
m	Mass	Kg
P_{shear}	Pressure in shear direction	$kg{\cdot}\ m^{-1}\ {\cdot}s^{-2}$
W	Strain energy density	$kg{\cdot}m^2{\cdot}s^{-2}$
W_d	Area of F-D curve	$kg{\cdot}m^2{\cdot}s^{-2}$
x	Displacement	m
Δx	Change in displacement	m
$x(t)$	Displacement as a function of time	m
$\ddot{x}(t)$	Acceleration	m/s^2
$\dot{y}(t)$ or $\dot{x}(t)$	Velocity	m/s
y_{max}	Displacement amplitude	m

Greek Symbols

Symbol	Name	Unit
γ	Shear strain	
$\Delta\gamma$	Change in shear strain	
E	Young's modulus	$kg{\cdot}\ m^{-1}\ {\cdot}s^{-2}$
ϵ	Strain	
$\Delta\epsilon$	Change in strain	
σ	Stress	$kg{\cdot}\ m^{-1}\ {\cdot}s^{-2}$

$\Delta\sigma$	Change in stress	kg· m^{-1} ·s^{-2}
τ	Shear stress	kg· m^{-1} ·s^{-2}
$\Delta\tau$	Change in shear stress	kg· m^{-1} ·s^{-2}
ω_F	Operating frequency	rad·s^{-1}

1. Introduction

1.1. Background

Vibratory screens are used extensively in the mining industry to process and grade different materials. The material processing is achieved through the vibratory motion of the screen. Failures in a vibratory screen are dangerous, as failures lead to the screen becoming unbalanced, which may result in violent and erratic motion. This violent motion of the screen can result in the failure of other components, and the screen becoming a danger to people and other machines in the vicinity of the screen.

Modelling a vibratory screen using software can create a better understanding of the behaviour of a vibratory screen as well as provide an understanding of why failures occur.

In the past, elementary models have been created to replicate the dynamics of a vibratory screen. However, these models have been limited to a small number of degrees of freedom with little physical validation used. To ensure that the models can capture the physics governing the behaviour of the screen it is necessary to extensively validate the models.

There is a need for an effective model of vibratory screen which can capture the physical nature of a vibratory screen. It is also necessary to ensure that the model is validated appropriately against the physical vibratory screen.

1.2. Problem Statement

In recent times great interest has been shown in optimising the screening efficiency and the geometry of vibratory screens. However, little work has been done to investigate how a model of a screen can be used to assist in determining how the screen is performing and to aid in the detection of failures or damage in a vibratory screen.

With the dawn of industry 4.0, more intelligence is being imbedded in machines, which is revolutionising fault detection and maintenance of machines. Assets can now be monitored using a hands-off approach and their status constantly determined. This allows for components to be replaced only once they have deteriorated to a state where failure is imminent. This approach saves the industry large amounts of money in terms of being able to detect when an asset is about to fail and act accordingly.

The failure of a critical component on an operational screen can result in an imbalance in the motion or forces present in the screen. This often results in erratic and unstable motions of the screen which

can lead to the failure of other critical components if the screen is not shut off in time. It is therefore necessary to develop an understanding of how the vibratory screen responds to certain faults and failures. Faults which are common in vibratory screens are: soft foot; different height rubber buffers; one of the vibration motors not working and different damping and stiffness characteristics of the rubber buffers.

It is noted that some of the faults listed above cannot be easily tested on a physical vibratory screen, as turning off one of the vibration motors could result in severe damage to the screen. It is thus important to develop a model of the screen which can simulate the dynamics of the screen accurately so that severe failures can be investigated. By understanding how a numerical model responds to different failure scenarios this allows for better identification of the same failure scenarios on a physical screen.

The detection and identification of faults is best done using intelligent methods trained using collected data. Once trained, the intelligent system takes inputs from the screen and can detect whether or not there is a fault present in the screen. If there is a fault with the screen, then the system will be able to identify the type of fault.

To create a model of the vibratory screen it is necessary to accurately characterise the rubber buffers on which the screen rests. It is critical to measure the stiffness and damping of the rubber buffer accurately under the operating conditions of the screen to ensure that the model of the screen is accurate.

1.3. Literature Review

The literature study is broken up into five main topics: vibratory screens, Finite Element Method (FEM) model of the screen, characterisation of the rubber buffers, intelligent methods and feature extraction. Each of these sections will be investigated and compared to the current literature on the topics. At the end of each section, conclusions will be drawn on how the information will be able to assist in the project.

1.3.1. Vibratory Screens

This section investigates the topic of vibratory screens. Four distinct topics relating to vibratory screens were investigated. These topics include: basic functions and critical ideas, fault detection, modelling and the process of optimising a vibratory screen.

Basic Functions and Critical Ideas

Screening operations are an important part of the coal and material processing industry. Vibrating screens are the most extensively used screening tools in the industry due to their compact shape and ability to process large amounts of material. One of the critical functions of vibratory screens is to effectively separate material passing over the screen deck. This is achieved by the motion of the screen deck (Mogensen, 1992). There are several different deck motion types such as linear, circular and elliptical (HE and LIU, 2009).

It is necessary to isolate the motion of the screen deck from the base of the screen and the ground, as it is undesirable to transfer the vibration to the ground and screen base. This is done by supporting the screen deck at the four corners by helical springs or rubber buffers (Mogensen, 1992), (Gómez and Metrekine, 2017). If the screen is not isolated from the ground correctly, then vibrations will pass to the ground which can damage the foundations and could result in unwanted vibrations being transmitted around the screen (Kolykhmatov, 1992).

Vibratory screens are excited by unbalanced rotational weights which are powered by motors (Faiz *et al.*, 2009). The most common excitation type of the screen deck is either circular or rectilinear. A screen which is excited with only one motor-vibrator will have rectilinear oscillations whilst a set of two motor vibrators which are set to operate in anti-phase by rotating in opposite directions to create a circular or elliptical motion of the screen (Kolykhmatov, 1992). According to Guo, Lin and Huang, (2011) the motion of a vibratory screen could be regarded as the composition of two harmonic vibrations which are mutually perpendicular and have the same frequency.

Fault Detection in Vibratory Screens

Another important aspect of vibratory screens is the detection of faults in the screen. The faults occur as a result of the constant vibration of the screen during operation. There are several methods such as statistical, frequency, static, dynamic and transfer function methods which can be used for fault detection. The above listed methods are often used in tandem with intelligent methods to efficiently detect faults in a vibratory screen.

In the paper by Xue, Zhao and Wu, (2011) crack fault identification in vibratory screens was performed using transfer function laws. The paper investigated methods which allow for the transfer function of a vibratory screen with and without a lower beam crack to be distinguished. The process of identifying the aspects which distinguish a signal between the two or more scenarios is called feature extraction. These methods are explored in greater detail in section 1.3.4 of the literature review.

The simulation of faults in vibratory screens is an important factor to better understand the response of a vibratory screen when faults are present. The most common faults which occur in industry are cracks in the body of the screen, one of the corners of the screen being higher than the others and springs or rubber buffers with different stiffnesses and damping properties.

In Rodriguez *et al.*, (2016) the concept of one spring in the system having a lower stiffness than the other springs was investigated. The effect of changing the spring stiffness was then compared to the loss in separation efficiency of the screen. For the model to be investigated under different stiffness conditions it was first necessary to validate the motion of the screen under unmodified conditions. The paper used three methods to investigate the dynamic motion of the screen. These methods include mapping the trace of the screen, the amplitude of the screen and the angle of inclination of the screen. Once the model of the screen was validated, the effect of varying the stiffness of the springs were found to have a significant effect on the movement of the centre of mass of the vibratory screen. By the movement of the centre of mass of the screen varying, it resulted in a lower separation efficiency.

Modelling of a Vibratory Screen

The most common practice in designing vibratory screens is to first model the vibratory screen using Finite Element Method (FEM) software. Modelling the screen in a FEM environment allows for parameters to be varied without having to manufacture a new screen for each design variant. The development of a FEM model can be regarded as a cheap and simple alternative to varying parameters on a physical screen. The process whereby a FEM model of the screen is developed is used in both the optimisation of the material processing and the simulation of faults in a vibratory screen.

The paper by Ramatsetse, Mpofu and Makinde, (2017) discussed the failure and sensitivity analysis of a reconfigurable vibrating screen using FEM. This paper presents several aspects which need to be considered for the development of a FEM model, to correctly model the physics of the problem. These aspects include the process of generating the FEM model, how the loads are applied to the model, the type of solver, boundary conditions, material selection, meshing and the simulation of the model.

The dynamic response of a reconfigurable vibrating screen using Finite Element Analysis (FEA) is considered the most effective method in optimising the mass and structural strength of the screen. There are different types of FEA analysis which are currently employed: static analysis, modal analysis, harmonic analysis, transient dynamic analysis, spectrum analysis, buckling analysis and explicit dynamic analysis (Ramatsetse, Mpofu and Makinde, 2017).

It should be noted that Ramatsetse, Mpofu and Makinde, (2017) attempted to predict the stresses on the loaded and unloaded screen under steady conditions. This was done so that the screen could be optimised in terms of the stiffness and reliability. The simulated model neglects the effects of inertia and damping.

Optimisation of a Vibratory Screen

In recent times and with the ever-growing performance of computers, researchers and designers of vibratory screens have been able to commence significant research into the optimisation of vibratory screens. The end goal of the optimisation of the vibratory screens is simple: to increase the bottom line ('Vibration analysis of vibrating screens', 2012). The most common ways in which vibratory screens are being made more efficient include: energy consumption, productivity, down time and maintenance of the screen.

In the paper by Yue-Min *et al.*, (2009) the reliability of the vibrating screen was increased by optimising the structural size of stiffeners on the side plate under multiple frequency constraints. The optimisation resulted in the reduction of the weight of the side plates and the increase of the natural frequencies, whereby the natural frequencies were moved further from the operating frequency. By reducing the weight of the screen, the manufacturing costs were reduced. The results of moving the natural frequency further away from the operating frequency resulted in the better avoidance of resonance which reduced the destructiveness of the screen.

From the above-mentioned papers, it was noted that in recent times that a lot of work and time has been invested in the optimisation of the vibratory screen. This means that it was possible to assume that the current vibratory screens on the market are optimised well in terms of their configuration, shape and excitation.

Conclusion

The failure of a vibratory screen can have dire consequences, in the sense that the screen could destroy itself as well as injure people in its vicinity. It is a good proposition to monitor the response of the screen to be able to detect any abnormalities in its behaviour. A FEM model of the vibratory screen can also be generated to perform simulations which are too dangerous to perform on the physical screen.

1.3.2. Development of the FEM Model of the Vibratory Screen

This section investigates the topic of the development of a FEM model of a vibratory screen. This section is composed of two parts: the development of a FEM model and the validation of a FEM model.

Development of a FEM Model

The use of simulated numerical models of machines or components of interest has become the norm in design and optimisation. It is simpler and more cost effective to simulate and investigate a model on a computer than to run experiments on a physical component or machine.

It is necessary to first provide reasons as to why FEM was chosen as opposed to multibody dynamics. Multibody dynamics is an approach to solving structural problems using individual masses and loads. Multibody dynamics is capable of modelling flexible systems, but rigid systems are modelled most often. One of the major limitations of multibody dynamics is that the method cannot model deformations of bodies but only the rigid body displacements.

FEM modelling is the application of loads to a body modelled with discrete elements to determine the stresses and strains over the body along with specified boundary conditions. Analysis can be linear or non-linear based on material properties and contact properties (Sharcnet.ca, 2018). FEM can model deformations as well displacements in the bodies. It was therefore decided to model the vibratory screen using FEM, as FEM can incorporate non-linear material models as well as measure stress and strain responses in a body. It was also observed from literature that the use of FEM was preferred over multi body dynamics when modelling vibratory screens.

The procedure to create a FEM model is to first construct a Computer-Aided Design (CAD) model of the component or machine of interest. It is important to note that the model constructed should be simplified in terms of the geometry by eliminating unnecessary detail. Once the CAD model has been constructed the model is imported into the FEM package. The next step is then to mesh the model. It is important to ensure that the meshing of the model is done correctly. If the model is meshed badly then the solution will either be a poor representation of the model or the solution will take a long time to solve (Mcmillan, Papadopoulos, 2011).

Before the model can be solved, the material properties and the boundary conditions need to be added to the model. If the model is symmetric, symmetry conditions can be applied to the model. This will reduce the solving time. Loading conditions are added to the model which reflect the same loads

as in the physical screen. In a vibratory screen the loads are created by the eccentric weights which are excited by the electric motors (Mcmillan, Papadopoulos, 2011).

Once the model has been set-up it can be solved in several different ways depending on the desired output. The different solvers were discussed above in section 1.3.1 by Ramatsetse, Mpofu and Makinde, (2017).

In the paper by Ronghua, Liuqing and Chenyu, (2011) FEM was used to find the optimal configuration of a vibratory screen by modifying the shape of the beam components. The optimality of the screen was measured by the maximum loads produced in each of the individual components. This is a good measure to determine where a screen is most likely to fail. Two types of analysis were performed in this paper; static and dynamic analysis.

The static analysis was performed to identify the location of the maximum displacement and maximum stress in the screen body. It was found that the maximum static stress in the vibratory screen was much less than the allowable stress of the materials, thus static failure was not a concern. The dynamic investigation of the screen was conducted in two different stages, the first stage was to determine the natural frequencies of the screen. This was done using the Block Lanczos method. The natural frequencies were then compared to the working frequency of the screen. It was found that the working frequency does not correspond or lie close to any of the natural frequencies. It can thus be concluded that resonance was not a factor in normal operating conditions of the screen (Yuan and Liu, 2014). The second part of the dynamic investigation was to excite the screen at its operating frequency and measure the structural displacement and stress. It was found that the deformation of the screen under operating frequency were small and that the entire screen has sufficient dynamic stiffness as to not be affected by fatigue.

Yue-Min *et al.*, (2009) followed the same process as Ronghua, Liuqing and Chenyu, (2011) in ensuring that the natural frequencies were not close to the excitation frequency. Insight was provided in the selection of the elements for the screen. The screen was modelled in ANSYS. The main structure adopted solid elements SOLID95 and SOLID92. The spring used COMBINE14 and the vibration generator was simplified as lumped mass element MASS21 (Yue-Min *et al.*, 2009).

Ramatsetse, Mpofu and Makinde, (2017) provide insight into the methodology of adding the boundary conditions, loads, material selection, meshing and simulation of a reconfigurable vibratory screen in ANSYS. The boundary conditions were applied to the screen to ensure that the FEM model could represent the physical attributes of the screen correctly. Boundary conditions were also added to

prevent the screen from moving in space. The loading of the screen was added to represent the loading from the vibrating motors. Harmonic loads were added to the screen as point loads.

The selection of the material properties of the screen is important. In the event of incorrect material being selected the results produced by the simulation could result in a poor representation of reality. The most important material properties for simulations are the modulus of elasticity, density and the Poisson's ratio.

It is noted that to minimise the time taken to run the simulation the features that were not relevant to the analysis and add needless complexities such as bolts, welds and holes were removed. The quality of the results produced by the simulation were directly proportional to the quality and size of the meshed components (Ramatsetse, Mpofu and Makinde, 2017).

Validation of a FEM Model

The development of a FEM model was covered in the above section; however, it is still not known if the FEM model could replicate the dynamics of the physical screen. To address this, methods have been produced to validate the model and to ensure that the model results are accurate. FEM models can be validated using two commonly used procedures; computing and comparing the natural frequencies of the FEM model with that of the physical screen and comparing the dynamic motion of the FEM model with the dynamic motion of the physical screen.

In the paper by Guo, Guo and Luo, (2010) a large vibratory screen was modelled in ANSYS. The mode shapes and natural frequencies of the vibratory screen were analysed to validate the FEM model of the screen. This was done by comparing the first twenty-six natural frequencies of the model to the first twenty-six known natural frequencies of the physical vibratory screen. If there was a strong correlation between the mode shapes and natural frequencies of FEM model and physical screen, it shows that the geometry and stiffness properties of the physical screen have been captured by the FEM model.

One of the possible methods to calculate the natural frequencies of the vibratory screen is to perform a modal hammer test. A modal hammer test works by impacting the screen body using a modal hammer. This impact then causes the screen to vibrate at a large range of frequencies. By measuring the response of the screen and converting the measured result into the frequency domain, the natural frequencies can be identified as peaks in the frequency domain. The peaks are caused by the body resonating at the specific frequency values (He and Xian, 2013), (Gómez and Metrekine, 2017). The second method which can be used to measure the natural frequencies of a structure is to simply excite

the body of the vibratory screen at a range of frequencies and measure the response of the screen. This procedure is more accurate than a modal hammer test as it allows the system to spend a longer time at each frequency and reach resonance better. However, this method requires a more elaborate set-up as opposed to the simple set-up of the modal hammer test.

One of the main gaps in the research is that there has been no interest placed in the development of a FEM model with the intent of replicating the dynamics of a physical screen. This gap in the research means that there are no models of vibratory screens available to investigate the effects of faults in vibratory screens accurately. Another use of such a model of a screen is in the event of a physical vibratory screen presenting a fault with an unknown cause. The model of the screen can be modified in different ways to attempt to replicate the fault and by replicating the fault, understand the nature of the fault in the physical screen.

Conclusion

It was found that there is a need for a model to be constructed that can replicate the dynamics of a vibratory screen. The development of such a model of a screen will allow for the simulation of extreme faults and failures in vibratory screens as well as the investigation of unknown faults in a screen.

FEM is the best method to use for the modelling of a vibratory screen. The simplification of the model of the vibratory screen will play a large role in the solution time as well as the solution accuracy. Thus, a large amount of time should be invested to ensure that the FEM model is constructed correctly.

It is necessary to ensure that the model can replicate the physics of the screen well. A two-fold validation can be done to ensure that the FEM model of the screen is accurate. The two-fold validation consists of a modal analysis to ensure that the natural frequencies of the physical screen and the FEM model correlate. The second validation will be a transient analysis of the screen. The transient analysis of the screen will be done to ensure that the motions of the physical screen and the FEM model correlate.

1.3.3. Characterisation of the Rubber Buffer

The process of characterising a spring is where the stiffness and damping values of the spring are calculated. In this section of the literature the processes and procedures for characterising a rubber buffer for a vibratory screen were investigated. This section is composed of four parts; what is spring stiffness and damping, measuring stiffness, measuring damping and FEM modelling of a rubber buffer.

What is Spring Stiffness and Damping

The stiffness of a spring is defined as the measure of resistance offered by an elastic body to deformation. There are two distinct characteristics of stiffness, namely linear stiffness and non-linear stiffness. Linear stiffness is described as the linear correlation between the force applied to an object and the deformation response of the object. Non-linear stiffness is when the force-displacement correlation is non-linear. Objects can also have force-deformation curves in which there is a linear relationship for small displacements and a non-linear relationship for large displacements (Champion and Champion, 2011).

The second property required to define a spring or rubber buffer is damping. Damping is a significantly more complicated property than stiffness, as it is a function of velocity (Lakhlani and Yadav, 2017). Mevada and Patel, (2016) provided a conclusive definition of damping: Damping is the phenomenon by which mechanical energy is dissipated (usually converted into internal thermal energy) in dynamic systems.

Knowledge of the level of damping in a dynamic system is important in the utilisation, analysis, and testing of the system. Damping is the energy dissipation of a material or system under cyclic stress. Several types of damping are inherently present in a mechanical system. They are: internal (material) damping, structural damping and fluid damping. Internal (material) damping results from mechanical-energy dissipation within the material due to various microscopic and macroscopic processes. Structural damping is caused by mechanical energy dissipation resulting from relative motion between components in a mechanical structure that has common points of contact, joints or supports. Fluid damping arises from the mechanical energy dissipation resulting from drag forces and associated dynamic interactions when a mechanical system or its components move in a fluid (Mevada and Patel, 2016).

The function of the rubber buffers in a vibratory screen is to isolate the motion of the screen from the ground without having a significant impact on the acceleration of the screen (Du Plooy and Heyns, 2001). There are several methods which are used to isolate the motion of a screen, the most common being vibration absorbers. The main design factors that impact the design of an isolator are ensuring that the isolator is as light as possible to reduce the mass ratio of the system, the damping of the absorber should also be as small as possible and the spring or buffer should be as soft as possible (Du Plooy and Heyns, 2001).

Measuring of Stiffness

The measurement of the stiffness of a rubber buffer or spring is simple as the stiffness parameter is predominantly dependent on the displacement of the body. However, it is also noted that the stiffness behaviour of rubber buffers varies as a function of temperature. Energy is dissipated in a rubber buffer due to damping. This results in the rubber buffer heating up during operation, whereby the stiffness properties of the buffer are altered. This needs to be considered during experimentation when using the rubber buffers.

The simplest way to characterise the stiffness is to perform a static test on the rubber buffer. The static test can be performed by adding masses to the rubber buffer and measuring the displacement as a function of the masses added. Once the function has been created the stiffness of the rubber buffer can be derived as the gradient of the function. Another method to apply the loading is to use a hydraulic press with a load cell which can measure the load versus the displacement (Cronjé *et al.*, 2005).

In the case of the force-displacement relationship being linear, the resulting gradient of the curve is a constant, thus only a single value is required to characterise the stiffness of the rubber buffer. In the event of the force-displacement curve being non-linear, methods have been developed to represent the non-linear functions. Figure 1-1 shows the two different types of force-displacement relationships. The calculation of the stiffness of a linear force-displacement relationship is done using equation 1.1.

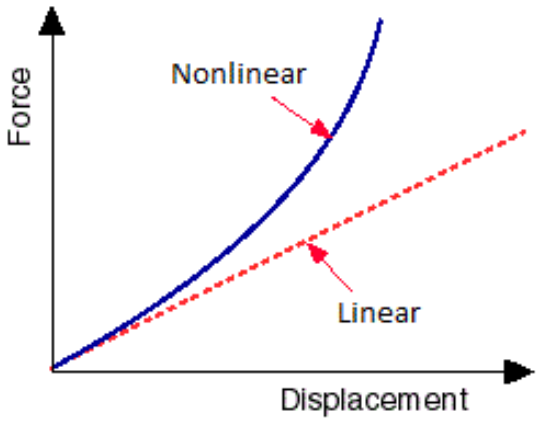

Figure 1-1 Plot showing the difference between linear and non-linear stiffness characteristics (Andrew, 2018).

$$k = \frac{F}{x} \tag{1.1}$$

There are two common ways to represent non-linear stiffness namely fitting a function through the data and using a hyperelastic material model. The curve fitting approach is where a function is fitted to the relationship between the force and the displacement of the spring. Champion and Champion, (2011) provide a Taylor series expansion of the elasticity equations that govern the action of a helical spring under axial loads as shown in equation 1.2. The error is significantly reduced by using the third order Taylor series expansion coupled with a least squares regression fit in relation to simply using the linear Hooks law expansion. It is noted that this method works well to map the non-linear behaviour in helical springs, however, in the case of rubber buffers a more diverse approximation method could be required.

$$F = k_1(l - l_0) + k_2(l - l_0)^2 + k_3(l - l_0)^3 \tag{1.2}$$

The most common hyperelastic models or strain energy functions are Mooney-Rivlin and Ogden. Fuller, Gough and Ahmadi, (1999) investigated which of these methods are better able to represent a rubber material. The investigation was conducted in both normal and shear directions on a laminated elastomeric bearing. The material was found to be non-linear, as the force-displacement function produced when the rubber was subjected to sinusoidal excitation was found to be hysteretic. Mooney-Rivlin and Ogden material models were used to define the stress-strain behaviour of the rubber. The results showed that the Mooney-Rivlin material model with a five-term expansion was able to best approximate the stiffening of the modulus of the rubber disc under compression and shear loads.

Measuring the Damping

The measurement of the damping is a significantly more challenging task than measuring the stiffness. Damping is dependent on the velocity of the body as well as the frequency of the excitation as can be seen in figure 1-2. The best way to visualise damping is through a force-displacement curve. If a system has damping present, then the force-displacement plot will be in the form of a hysteresis loop. The nature of the force-displacement curve is due to the different paths followed during the loading and unloading cycles. Figure 1-2 below shows a hysteresis loop, the top part of the hysteresis loop is the loading and the bottom part is the unloading (Bian and Jing, 2017).

The area enclosed by the hysteresis loop represents the energy dissipated by damping. It has been shown that damping is a function of the enclosed region in a hysteresis loop. The procedures used to calculate the damping values using a hysteresis loop are show in equations 1.3 to 1.4. The enclosed area of the hysteresis loop is calculated using the cyclic integral of the load and the velocity in terms of displacement. With the enclosed area of the hysteresis loop calculated the equivalent damping constant is calculated using equation 1.5 (Milašinović, 2007).

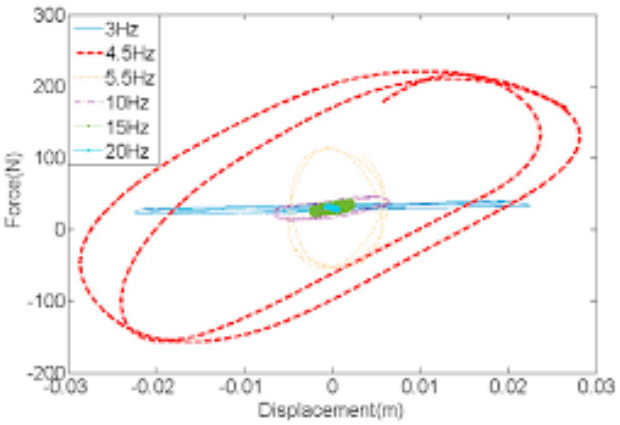

Figure 1-2 Plot showing the effects of frequency on a force displacement curve (Bian and Jing, 2017).

$$W_d = \oint F_d \dot{y}(t) dy \tag{1.3}$$

$$W_d = \pi c_{eq} \omega_F y_{max}^2 \tag{1.4}$$

$$c_{eq} = \frac{W_d}{\pi \omega_F y_{max}^2} \tag{1.5}$$

Modelling a Rubber Buffer in a FEM Environment

It is important to be able to model a rubber buffer accurately in a FEM environment as the displacement and deformation properties of rubber behave differently to other materials. The first step is to determine what type of material model should be used. Luo, 2017 and Luo and Wu, (2006) used a Mooney-Rivlin material model to model rubber used in an axle-box pivot bush with voids. The material properties for the Mooney-Rivlin material model were determined using the built-in calculator that most FEM packages provide. The FEM models were created and solved using the same applied loads as in the data. The results were compared, and it was found that the FEM model can model the torsional load vs displacement of the data perfectly. The same result was found from the radial and axial models. Luo, Wu and Mortel, (2000) performed a similar study as above, but on a different geometry. This investigation also made use of modal analysis as well as a static test to ensure that the FEM model of the rubber bolster spring responded in a correct manner.

Conclusion

The characterisation of a rubber buffer involves the calculation of the stiffness and the damping. The stiffness can be calculated using the displacement of the rubber buffer. Depending on the nature of the stiffness plot; either a linear stiffness or non-linear stiffness model should be used. The damping of the rubber is measured using the energy dissipation in the hysteresis loop. The measured characteristics will be validated against experimental results of the deformation of the rubber buffer.

1.3.4. Intelligent Methods to Detect Faults

Intelligent methods are methods which can be used to detect differences between various inputs. These inputs are referred to as features. The different features extracted from the data are used as inputs into the intelligent system. The aim is to differentiate between normal operating conditions and operating conditions where a fault is present in the screen (Lee *et al.*, 2014). The intelligent methods section is composed of two parts; a breakdown of intelligent methods and the application of intelligent methods in fault detection.

Breakdown of Intelligent Methods

There are many intelligent methods available, with new methods being developed and old methods being adapted constantly. The most common intelligent methods used for fault detection in vibration signals are: artificial neural networks, convolutional neural networks, support vector machines, Bayesian networks, Gaussian process regression, fuzzy logic and manifold learning. These methods are explored in greater detail below.

Artificial neural networks (NN) are one of the best and most commonly used machine learning methods in prognostics as well as fault detection of dynamic structures. Chang *et al.*, (2002) provide an NN analogy to the brain, NN models are made up of interconnected processing elements called neurons which respond in parallel to a set of input signals given to each. An NN model consists of three main parts: neurons, weighted interconnections between neurons and activation functions that act on the set of input signals at neurons to produce output signals. Training is essential to NN models. Training of an NN model involves determining the weights of the interconnections between the nodes using a training algorithm. Training samples are needed to train an NN model. There is a strong correlation between the quality and number of training samples and how well the NN classifies new data.

The most common uses of NN in prognostics are to identify damage in a system from the changes in the structural signatures. The NN is trained using signals from an undamaged system and a system that has damage present. By training the system on the different types of faults, an NN is be able to distinguish between the nature of the faults. The use of Convolutional Neural Networks (CNN) is similar to that of NN whereby the activation function of the neurons is now convolutional. One of the most common implementations of CNN is in image processing. Image processing can be used in identifying differences in frequency spectrums (Xiong, Yang and Gan, 2012).

Support vector machines (SVM) are also known as maximum margin classifiers. SVM act to optimise the boundary between several different classes of data. The function of an SVM is to create a multidimensional plane which separates the data points or features of the different classes. The plane which separates the data is called a hyperplane. The hyperplane is generated using training data so that the hyperplane lies in a position of maximum distance between the feature data in the different classes. Once created, the hyperplane can then be used to classify new data using the side of the hyperplane the data values fall (Kan, Tan and Mathew, 2015).

Bayesian networks is an intelligent method which is widely utilised in fields such as fault diagnosis, fault prediction, military decision-making, information fusion, data mining and many other industries. Bayesian networks work by making use of probabilistic graphical models. These models represent specific parameters and their conditional dependencies. Bayesian networks operate by comparing a known set of data from a specific class to a new set of data from an unknown class. The Bayesian network then produces a probability of the data falling part of a specific class. Using the output of the network the class with the highest probability can then be selected as the class where the unknown data most likely fits, this is known as the maximum likelihood (Xiao *et al.*, 2016).

Gaussian process regression is a machine learning method that uses Gaussian processes to measure the difference between sets of data. A Gaussian process regression model is completely described by the mean and covariance function of a data set. The classification of data points is done by comparing the mean and covariance information of data with a known class, with that of data from an unknown class. The classification is conducted using a probabilistic approach. The probability is calculated by subtracting the specific class mean and covariance from the mean and covariance of new data. The smaller the difference between the means and covariances, the higher the probability of the data falling in that specific class. Gaussian process regression is a good method to use when the number of samples in the training set is small as well as for high dimensional data. One of the major drawbacks of Gaussian process regression is the computational demand due to the non-parametric nature of the method (Kan, Tan and Mathew, 2015).

Fuzzy logic is an intelligent method which was developed to overcome the problems associated with NNs, as fuzzy logic allows for a higher level of transparency and openness in the processing of data. Fuzzy logic incorporates non-linear mapping of an input data with a scalar output. Fuzzy logic works on the premise of a degree of truth, the degree of truth in a process can be described as a range of the continually overlapping states. The continuously overlapping states are used as an output measure to determine how well a new set of data can describe a known set of data. The overlapping states also allow for a degree of uncertainty to be measured (Kan, Tan and Mathew, 2015).

Manifold learning is an intelligent method most commonly used in the classification of data, most commonly image recognition and image processing. However, in recent times manifold learning has become increasingly implemented in fault detection and diagnosis in machinery. Manifold learning works by investigating the inherent low-dimensional manifolds embedded in high-dimensional observation spaces. The general manifold learning strategy for fault diagnosis is as follows: first the data needs to be pre-processed, this is done by setting up a pattern space. The next step is to perform the feature extraction of the data using S-LapEig algorithm, this captures the intrinsic manifold property and translates the samples into low-dimensional feature space. The third step is to implement the pattern classification of the samples. This is to construct a category space of the data. The final step is to perform the classification of new data types and to determine the nature of the fault in the data (Jiang *et al.*, 2009).

Application of Intelligent Methods in Fault Detection

Intelligent methods are often applied to fault detection as intelligent methods can detect higher order patterns than humans are often unable to understand. Intelligent methods are used to identify the faults by first training the methods. The training of the methods is done using data from signals which have specific types of known faults as well as signals without any faults. It is noted that the class of the faults is known during the training process. Using the knowledge of the class of the fault, the intelligent method is taught to distinguish between signals without a fault present and signals with a fault present. The intelligent methods can also be trained to identify the specific type of fault present as well as how severe the fault is.

It is often not possible to train the intelligent method using the entire signal. It is thus necessary to isolate certain parts or aspects of the signal which carry the critical information of the signal. Using these parts or aspects allows for the identification of whether a fault is present in the signal and if a fault is present, the nature of the fault. These parts or aspects of the signal are known as features. The process of feature extraction was covered in section 1.3.5 of the literature study.

Gan, Wang and Zhu, (2015) investigated the validity of multiple-domain manifold learning to detect bearing and gear faults. Their study aimed to investigate the best way to analyse a signal in the time, frequency and time-frequency domains. The procedure used to develop the multiple-domain manifold is as follows: divide the data into training and testing sets, construct the multiple-domain space on the training data so that there is enough information about the domains, perform as singular value decomposition on each of the multiple domains, calculate the intrinsic dimension using maximum likelihood estimation, calculate the multiple-domain manifold features for the testing samples using

the same procedure as for the testing samples and lastly, train the classifier using the training data and test it using the testing data. Once this is completed the classifier can be used to classify new data. The results show that the multiple-domain manifold method was able to classify faults well in vibrating machines.

Kan, Tan and Mathew, (2015) investigated how different intelligent systems perform on different types of machines. The results showed that different methods perform better for different machines. This shows that there is no set intelligent method that is superior in all applications. It is thus important to consider a range of intelligent methods in fault detection. Kan, Tan and Mathew, (2015) investigated the advantages and disadvantages of several common intelligent methods.

Kumar and Kumar, (2017) investigated the use of support vector machines to classify failures in the bearings and impellers. A range of optimisation methods were used to find the optimum parameters for the support vector machine algorithm. The results showed that the best method was to use a genetic algorithm.

Chang *et al.*, (2002) investigated the development of an iterative NN technique for updating structures. The investigation included the number of training samples needed to adequately train an NN. Chang *et al.*, (2002) aimed to investigate the updating process of the flexural rigidities of a simply supported beam, the material properties and boundary conditions of a circular plate. An iterative process of updating the model was used. The updating procedure is figure 1-3. It is found that the liner selection method for sample selection resulted in the fastest convergence rate of the flexural rigidities. The same results were found for the circular plate.

Conclusion

Several different intelligent methods were investigated. It was found that different intelligent methods offer different advantages and disadvantages depending on the application. According to the above section the best intelligent methods to classify vibration signal faults are NN, SVM and multiple-domain manifold learning. Due to the nature of vibration signals it is necessary to extract features from the signals to reduce the size of the inputs. The extraction of features from signals was explored in greater depth in the next section.

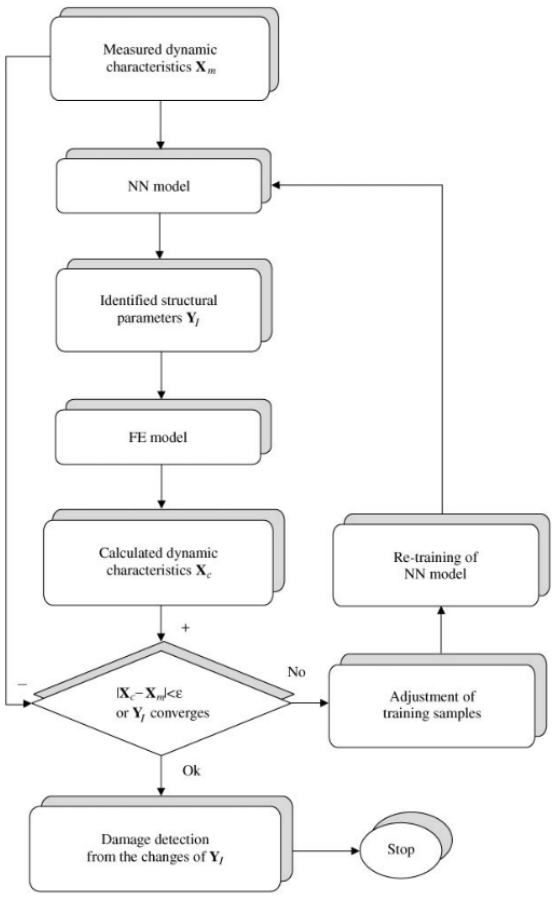

Figure 1-3 Iterative NN process for identification of structural parameters (Chang *et al.*, 2002).

1.3.5. Feature extraction and use in fault detection

This section investigates feature extraction. Four distinct topics about feature extraction and fault detection were investigated. These include: feature extraction, signal processing, methods to extract features and the use of features to classify faults.

Feature Extraction

Feature extraction is an important part of deciphering where the critical information about the fault is being carried in the signal (Guyon and Elisseeff, 2006) and (Jiang *et al.*, 2009). The idea behind what a feature is was mentioned in the paper by Xue, Zhao and Wu, (2011) in the section 1.3.1 where features were used to distinguish between whether the vibratory screen deck had a crack or not. Examples of features commonly extracted from vibration signals are: mean, standard deviation, kurtosis, skewness, minimum, maximum, frequency information, as well as many other features.

It can be noted that the selection of feature is important in the success in determining whether there is an anomaly in the performance and operation of the investigated object. By using certain features

as opposed to the entire signal, the speed at which the signal is investigated will be increased and the accuracy of the results attained from the signal become more accurate (Guyon and Elisseeff, 2006).

Signal Processing

There are many methods available in literature for feature extraction from data signals. However, before features can be identified, detected and used to determine the type of fault, it is often necessary to process the signal. Processing the signal is used to enhance certain parts of the signal, more specifically the parts of the signal which carry the information about the faults (Liu, Peng and Li, 2011).

Signal processing can be broken up into two categories: stationary signal processing and non-stationary signal processing. Stationary signal processing is done when the signal has a constant frequency, amplitude and phase. The current processing methods most often used for stationary signals are weighted Zoom Fast Fourier Transform (ZFFT) and the self-adaptive extraction ZFFT. A non-stationary signal can be characterised as a signal whose statistical properties are time dependent. Non-stationary signal processing is done with an entirely different set of methods. The methods used combine both the time and frequency domain together. These methods include the Winger-Ville time-frequency distribution and Wavelet transform processing (Liu, Peng and Li, 2011), (Wang *et al.*, 2016).

The Wigner-Ville time-frequency distribution makes use of several steps to process the signal. These steps include, adding different kernel functions to the signal and the application of band-pass pre-filters to ensure the frequency components are retained for the signal. The Wigner-Ville time-frequency distribution is mainly used for signals that have low frequency components or distant-distributed frequency components. Wavelet Transform (WT) processing is currently the most used time-frequency analysis method. WT processing uses a variable scale sliding window to intercept the signal into segments for analysis. By the window having a variable scaling, it allows for the time and frequency resolution to be modified according to the characteristics of the signal (Liu, Peng and Li, 2011).

Other signal processing methods include the procedure to separate the fast and slow motions of a mechanical system. The procedure to achieve this separation was outlined in the paper by Blekhman and Sorokin, (2010). The separation of the fast and slow motions was done using the method of direct separation of motions. This was done for problems where the high frequency range was velocity dependent.

Fault Extraction Methods

In machinery fault diagnostics it is critical to define the type and nature of the faults which appear. In further investigating the faults it is often found that the motion and vibration of the system with the fault is often more chaotic than that of a machine without a fault. Using this knowledge, it is possible to identify when a fault is present in a machine (WANG *et al.*, 2001).

The most common currently used methods for feature extraction are orbit portrait, FFT spectra, cepstra and time frequency analysis. These methods coupled together allow for identification of faults in machines. If the methods are fine-tuned and there is a large amount of information about the different faults, then it is possible to use one or more features to identify and distinguish between different faults as well as measure the severity of the faults.

Use of Features to Classify Faults

With the concept of features established, it was important to understand what the uses of these features were. The features are used as detection mechanisms of when a fault has occurred in a machine. Features can be further investigated and developed so that it is possible to detect several different faults on a single machine.

Chang *et al.*, (2002) provide insight into how features could be used as inputs of an NN. The feature values were used to train an NN so that it could predict outputs from the new inputs. The NN was trained to detect faults in a simply supported beam. A comparison between the orthogonal array method and four other methods was illustrated using two numerical examples from section 1.3.4. The results indicate that the orthogonal arrays method could significantly reduce the number of training samples without significantly affecting the accuracy of the NN prediction.

Conclusion

The extraction of features which provide information about faults in a vibratory screen are invaluable. The use of these features allows for the identification of faults and prediction of when failures could occur. Some of the most viable faults which could be used for the screen are the trace, displacement, velocity and acceleration of the screen at different points on the screen deck. The fault information in the signal can also be enhanced using signal processing techniques.

1.4. Scope of Research

The scope of the work is divided into three sections: the development of a FEM model, the calibration of the FEM model and the validation of the FEM model against experimental results.

The main part of the investigation involves the development of a FEM model which can replicate the dynamic motion of a physical screen. Such a model has not yet been developed and will allow for growth in the understanding of the dynamics of a vibratory screen as well as the detection and understanding of faults in a vibratory screen.

1.4.1. Development of the FEM Model

The development of the FEM modes is where the physical characteristics of the screen are captured. To ensure that the FEM model is an accurate representation of the physical screen it was necessary to characterise the rubber buffers which isolate the screen from the base, as well as model the geometry and material properties of the screen body. The rubber buffers were characterised in terms of their stiffness and damping characteristics. These characteristics were then used in the FEM model of the screen to represent the rubber buffers. Next, the geometry of the main body of the screen was developed. This was done by simplifying an already existing CAD geometry of the screen. The geometry was simplified to ensure that the FEM model does not contain components which add little to the accuracy of the simulation but greatly increase the complexity in solving the problem. Once the geometry of the screen had been established, the next step was to add the material properties as well as the constraints and loading conditions.

1.4.2. Calibration of the FEM Model

The calibration of the FEM model was done to ensure that the physics of the model were the same as that of the physical screen. The end goal in the development of the FEM model was to be able to simulate extreme conditions and faults using the FEM model, since performing such simulations on the physical screen could result in damage and/or accelerated fatigue of the screen.

A two-step calibration process was done to ensure that the model of the screen was as similar to the physical model as possible. The use of a two-step calibration to ensure that a vibratory screen model captures the physics of a physical screen has not been investigated before.

The first step was to perform a modal analysis of the physical screen as well as on the FEM model of the screen. The modal frequencies and mode shapes were compared. This was done to ensure that the geometry and material properties of the FEM model were the same as that of the physical screen.

The second calibration method was to excite the FEM model using the same excitation force as in the physical screen. A transient analysis of the screen was done to ensure that the dynamic response of the FEM model was the same as the dynamic response of the physical screen. The dynamic properties investigated were the displacement, velocity and acceleration of the screen. These properties were investigated at the four locations where the rubber buffers meet the vibratory screen deck. The dynamics of the FEM model were correlated to that of the physical screen by varying the loads on the screen to ensure that the dynamics matched up.

1.4.3. Validation of the FEM Model

The FEM model validation was performed to investigate if the FEM model could simulate faults correctly. The faults investigated were changing the rubber buffer stiffness and damping characteristics. The validation of the FEM model was done by investigating how well the model replicated the dynamics of the physical screen under similar faults. This was done by developing an intelligent system that could classify the different faults.

Once the intelligent system had been investigated, the final step was to validate the FEM model against that of the physical screen. This was done by training an intelligent system using the FEM data and then classifying the experimental data using the FEM data trained intelligent system. Doing this highlighted any short falls in the FEM model as well as identified aspects which contributed to the validation of the FEM model.

1.5. Document Overview

This document is composed of four sections: characterisation of the rubber buffers and the modelling of the vibratory screen, experiments on the screen, extraction of the results and validation of the screen model and the development of intelligent systems to classify faults on the screen.

Characterisation of the Rubber Buffers and Modelling of the Vibratory Screen

This chapter includes two sections: the characterisation of the rubber buffers and the modelling of the vibratory screen. The modelling of the vibratory screen section includes the experimental investigation, where the data about the stiffness and damping response of the rubber buffers was gathered. The experiments were conducted in both the normal and shear directions of the rubber buffers. Once the experiments on the buffers were conducted the next step was to use the experimental data to calculate the stiffness and damping values. The stiffness and damping values of the screen were then used in the FEM model of the screen.

The second section in the chapter was the development of the model of the vibratory screen. This was done using ANSYS. First a CAD geometry was simplified by removing unnecessary detail and imported into ANSYS. Next, the springs were modelled, and the geometry was cut to make for better meshing. The screen was meshed, and a modal analysis was conducted on the screen. The modal analysis results were used later in the document to validate the geometry of the model. Finally, the loads which act on the screen deck were calculated and added to the model.

Experiments on the Screen

In this chapter the experiments on the physical screen were conducted. The first experiment on the screen was a modal analysis which was used to correlate the FEM model to the physical screen. Next, experiments to measure the dynamic response of the screen were performed. These experiments included: measuring the response of the screen under different stiffness rubber buffer configurations and experiments on the screen with weights. The experiments with the different stiffness rubber buffers were conducted to measure the steady state as well as the run-up and run-down response of the screen.

Extraction of Results and Validation of the Screen Model

This chapter involved the extraction of the results gathered in the previous chapter as well as the validation of the FEM model using the experimental results. The modal analysis results were extracted, and the resonant frequencies were found. Next, the results from the experimental modal analysis and the FEM modal analysis were correlated to ensure that the FEM model captured the physics of the physical screen. Next, the results from the response of the screen were extracted and processed using filters and the acceleration results were integrated. The results were then used to correlate the transient response of the FEM model by manipulating the loading conditions of the FEM model. This procedure was followed until the FEM model displacement was the same as that of the experimental results. The correlation of the FEM model was only done using the results from the base simulation.

The validation of the FEM model was done by comparing the results from the transient response of the screen with the transient results of the FEM model. It was found that the validation was not viable by simply looking at the responses together. It was thus decided to use and compare the various features of the responses.

Development of Intelligent Systems to Classify Faults on the Screen

In this chapter intelligent systems were developed to correlate features from the FEM and experimental data. This was done to validate the response of the screen. It was decided to train an intelligent system using the FEM data and then test how well this system was able to classify the experimental data. Before this was investigated, it was necessary to show that an intelligent system could be trained to classify faults on a vibratory screen. This was done on the experimental data for the different stiffnesses, run-up and run-down experimental data, masses on the screen and the FEM data for the different stiffnesses. It was found that it was possible to train an intelligent system to classify the faults on the above-mentioned data. With this done the experimental results were classified using the experimental data. It was found that there were inconsistencies in the response of the physical screen that made the classification impossible.

2. Practical Investigation

The investigation comprises of two sections. The first section is the investigation and characterisation of the rubber buffers and the second section is the development and validation of a FEM model of the vibratory screen.

The function of the rubber buffers is to support the screen and to isolate the motion of the screen from the support frame and ground. There are 4 rubber buffers used, each at a corner of the screen. The arrangement of the rubber buffers in the screen can be seen in figure 2-1. The characterisation of the rubber buffers included measuring the stiffness as well as the damping of the rubber buffers in both the normal and shear directions.

The vibratory screen pictured in figure 2-1 is a small test screen used for material dewatering. The screen has a mass of 691kg and is excited using two Invicta vibrating motors. The operating frequency of the screen is 16Hz. The FEM model was developed on this particular screen. This screen was developed and constructed by Weir Minerals and is used to perform experiments to further the understanding of vibratory screens as well as to investigate and test new technologies. ANSYS was the chosen FEM package which was used to develop the FEM model of the screen.

Figure 2-1 Picture of the vibratory screen which was investigated.

2.1. Characterisation of the Rubber Buffer

The characterisation of the rubber buffers is important as the stiffness and damping values are required in the FEM model of the screen. The stiffness and damping values of the rubber buffers need to be calculated in both the normal and shear directions. Two rubber buffers were cut down for future experiments on the screen. These rubber buffers are subsequently characterised.

The rubber buffers used by the screen are made from vulcanised rubber moulded to form. The dimensions of rubber buffers are 135mm high, 52mm inner diameter a 121mm outer diameter under unloaded conditions.

In this investigation the rubber buffers were modelled using ANSYS FEM software as well as using analytical equations. The analytical approach involved solving the equation of motion of the spring-mass-damper system shown in equation 2.1. The goal of the FEM and analytical models was to measure the characteristics of the rubber buffer correctly so that the models produced the same force displacement graph as the experimental results of the rubber buffer in both the normal and shear directions.

$$m\ddot{x}(t) + c\dot{x}(t) + kx(t) = f(t) \tag{2.1}$$

In the interest of ensuring that the characterisation of the rubber buffer was a suitable representation of the true dynamics of the rubber buffer, the limits of the rubber buffer were investigated. The aim of this investigation was to find out under what deformation magnitudes the behaviour of the rubber buffer was linear. For this investigation a displacement amplitude of 20mm was applied in both the normal and shear directions. The displacement amplitude of the physical screen is 3-4mm under steady state conditions. It is noted that the displacement of the screen is much larger under run-up and run-down conditions. Due to limitations in the laboratory the maximum frequency at which the system could be excited was 1Hz, this is obviously very different to the excitation frequency of the screen. It was expected that the loads in the rubber buffers were dominated by the stiffness of the rubber buffers as opposed to the damping. It was decided to only perform the investigation at the maximum frequency achievable by the setup as it would provide the best information in relation to that of using a range of lower frequencies.

2.1.1. Experiments on the Rubber Buffers

Experiments were conducted on the rubber buffers in order to measure the stiffness and damping properties. The experiments were conducted on the uncut normal rubber buffers from the screen as well as two cut down rubber buffers.

Experiments on the Rubber Buffers in Normal Direction

The rubber buffers were excited by applying a set displacement, the magnitude of the displacement was controlled using a signal generator. The applied displacement to the rubber buffers resulted in the compression of the rubber buffers. The resultant force was measured as a function of time using a load cell. The top and bottom plates were assumed to be a rigid due to the plates having a much larger stiffness than that of the rubber buffer. Thus, the displacement was assumed to be exclusively due to the compression or elongation of the rubber buffer. The set-up of the experiment can be seen in Figure 2-2 below.

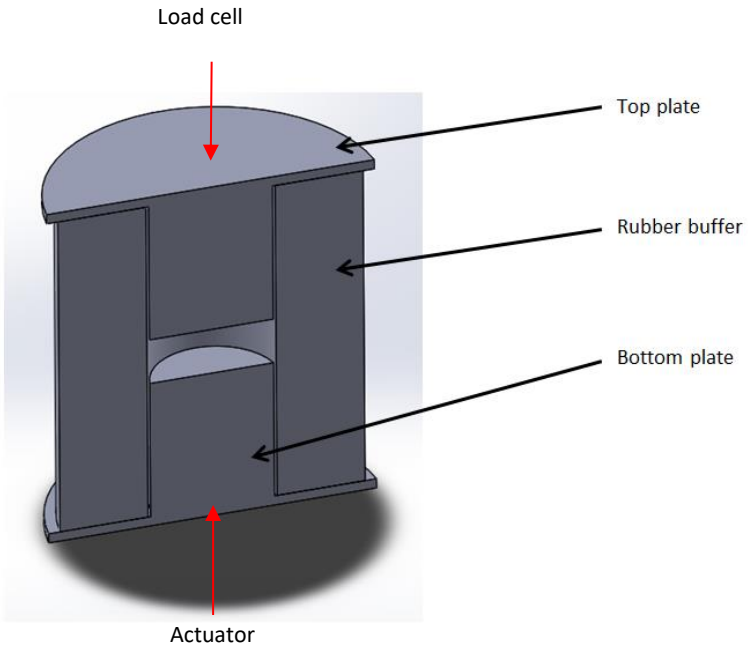

Figure 2-2 Cross-section of the experiment in the normal direction.

This experiment was conducted on the uncut rubber buffer as well as the two cut down rubber buffers. The rubber buffers were cut down using a lathe in the laboratory to reduce the volume of the rubber by approximately 30%. This value was used as it would have a definite impact on the characteristics of the rubber buffers but not risk the rubber buffers being too soft as for the screen to come off its supports. The cut down rubber buffers were investigated individuality as there were likely to be differences in their properties due to the buffers not being identical. Figure 2-3 shows the two cut down rubber buffers which were used in the experiments. The height and inner diameter of the cut down rubber buffers are the same as the original rubber buffers. The new outer diameters of the buffers are 103mm for the buffer on the left and 104mm for the buffer on the right.

Figure 2-3 The two cut down rubber buffers.

Apparatus:

1. 1x uncut rubber buffer, 2x cutdown rubber buffer
2. Schenck 100kN Hydraulic Actuator
3. Control software
4. Computer
5. Load cell
6. Top plate
7. Bottom plate
8. Tape
9. Signal generator

Experimental Procedure:

1. Remove a rubber buffer from the vibratory screen.
2. Place the bottom plate on top of the excited surface of the actuator.
3. Mount the rubber buffer on the pin that protrudes from the bottom plate.
4. Place the top plate so that the pin goes inside of the rubber buffer.
5. Ensure that the load cell is touching the top surface of the top plate.
6. Make sure the rubber buffer and the plate pin have a tight fit (a tight fit is achieved by wrapping tape around the pin).
7. Set the amplitude of the actuator displacement to be 20mm.
8. Set the computer to record the time, force and displacement data.
9. Turn on the actuator to gather data.
10. Repeat steps 9 and 10 three or more times to get more data points that can be compared to confirm that the experiment is repeatable.

11. Repeat steps 2 to 10 for the two cut down rubber buffers.

Experiment on Rubber Buffers in the Shear Direction

The rubber buffers were excited by applying a set displacement using the actuator in the lateral direction. The magnitude of the displacement was controlled using the signal generator. The applied displacement to the rubber buffer resulted in the displacement of the rubber buffer in the lateral direction. The top and bottom plates were assumed to be rigid due to the plates having a much larger stiffness than the rubber buffer. The experimental set-up is shown in figure 2-4.

The force was measured as a function of time using the load cell. It is noted that it was not possible to measure the force and the displacement at the same time. Therefore, the force and the displacement were measured separately and then collated together.

To measure the amount of force that the actuator imparted on the rubber buffer in the shear direction the rubber buffer shear force arrangement was set-up in such a way that the top part of the bottom plate was acting against the load cell. The actuator was then excited at the same displacement as in the previous experiment in the normal direction. The actuator was moved down the displacement level and then returned to its initial position. When the actuator returned to its initial position, it imparted a load of the same magnitude against the load cell, while the displacement of the system remained zero.

This experiment was conducted on the uncut rubber buffer as well as the two cut down rubber buffers. The cut down rubber buffers were investigated individually as there were likely differences in their properties due to the buffers not being identical.

Apparatus:

1. 1x rubber buffer, 2x cutdown rubber buffer
2. Schenck 100kN Hydraulic Actuator
3. Fixed mounting plate
4. Free mounting plate
5. Control software
6. Computer
7. Tape
8. Load cell
9. Signal generator

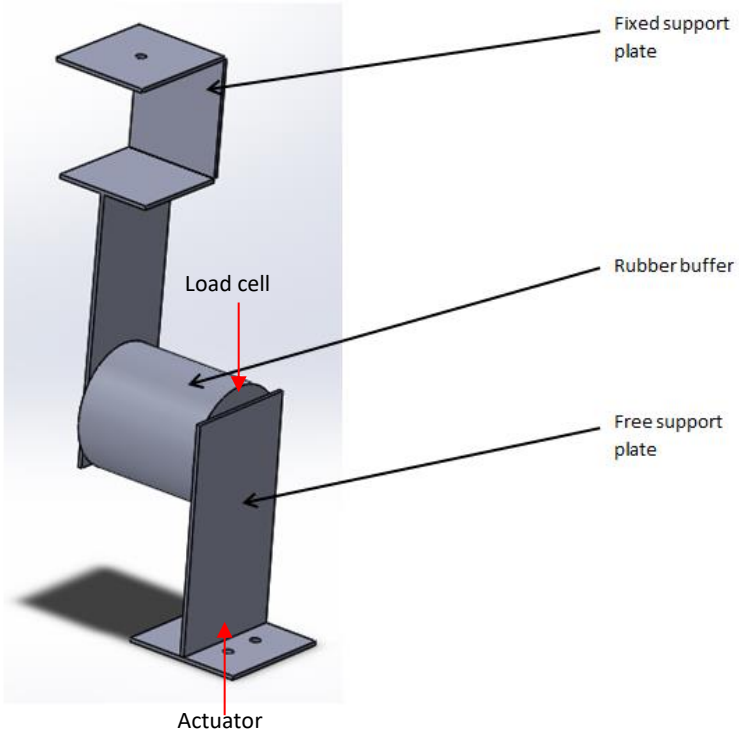

Figure 2-4 Experimental setup in the shear direction.

Experimental Procedure to Measure the Displacement:

1. Remove one rubber buffer from the screen.
2. Mount the bottom plate to the actuator by means of 4xM10 bolts.
3. Mount the top plate to the beam above the actuator and tighten the single M10 bolt to keep the plate in place.
4. Place the rubber buffer over the pins of the top and bottom plates.
5. If the rubber buffer is loose, then tape around the pins to ensure that the rubber buffer has a tight fit.
6. Enter the required displacement amplitude into the actuator.
7. Set the computer to record the time and displacement data.
8. Turn on the actuator to gather data.
9. Repeat steps 8 and 9 three or more times to get more data points that can be compared to confirm that the experiment is repeatable.
10. Repeat steps 2 to 9 for the two cut down rubber buffers.

Experimental Procedure to Measure the Force:

1. Repeat steps 1 to 7 from the experimental procedure to measure the displacement.
2. Adjust the height of the actuator so that the top of the bottom plate is resting against the load cell.

3. Set the computer to record the time, force and displacement data.
4. Turn on the actuator to gather data.
5. Repeat steps 3 and 4 three or more times to get more data points that can be compared to confirm that the experiment is repeatable.
6. Repeat steps for the two cut down rubber buffers.

2.1.2. Results

In this section the results from the experiments are processed and the damping and stiffness values calculated.

Experiments were done for much larger deflections for the uncut rubber buffer in the normal and shear directions. Looking at figure 2-5 and figure 2-8 the response of the rubber buffers in both the normal and shear direction are essentially linear over the displacement range.

It can be seen from figure 2-5 to 2-10 that the relationship between the force and displacement is essentially linear under normal and shear loading conditions. It can be concluded that the stiffness behaviour of the rubber buffers can be assumed to be linear for both small and large deflections. To ensure that the relationship of the rubber buffer is linear over the entire range.

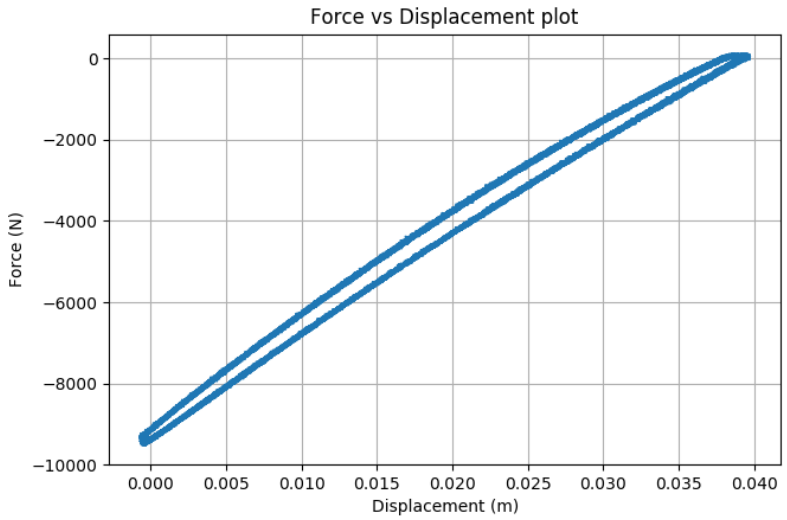

Figure 2-5 Plot showing the force-displacement curve of the experimental data for the uncut rubber buffer in the normal direction under quasi-static loading conditions.

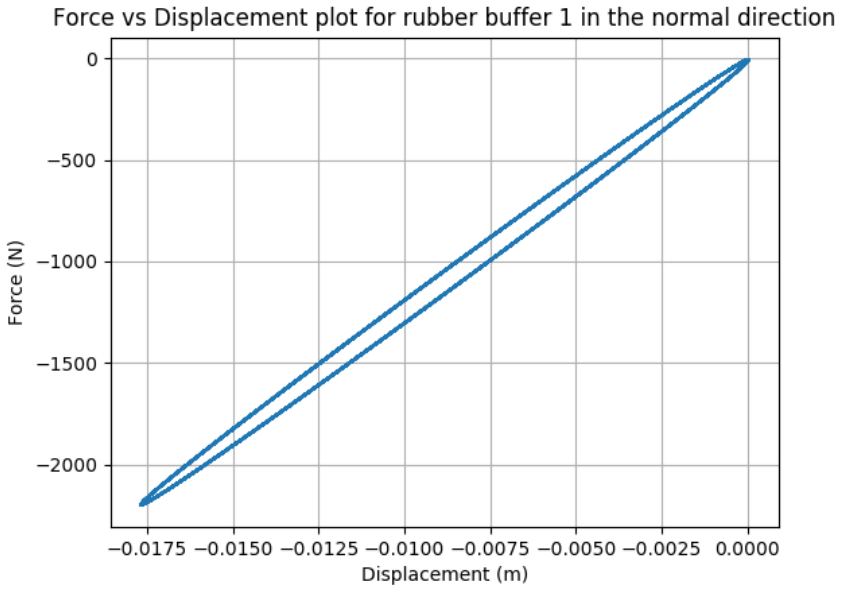

Figure 2-6 Plot showing the force-displacement curve of the experimental data for rubber buffer 1 in the normal direction under quasi-static loading conditions.

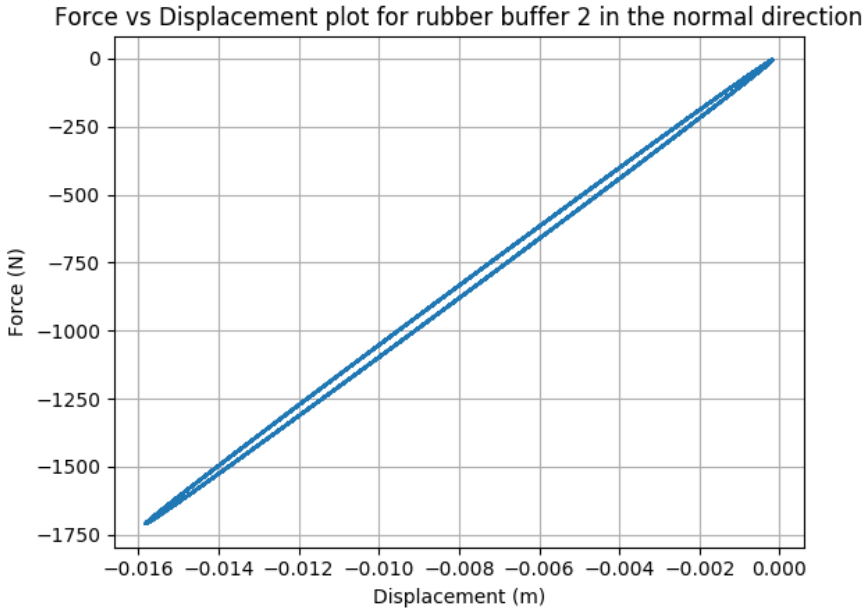

Figure 2-7 Plot showing the force-displacement curve of the experimental data for rubber buffer 2 in the normal direction under quasi-static loading conditions.

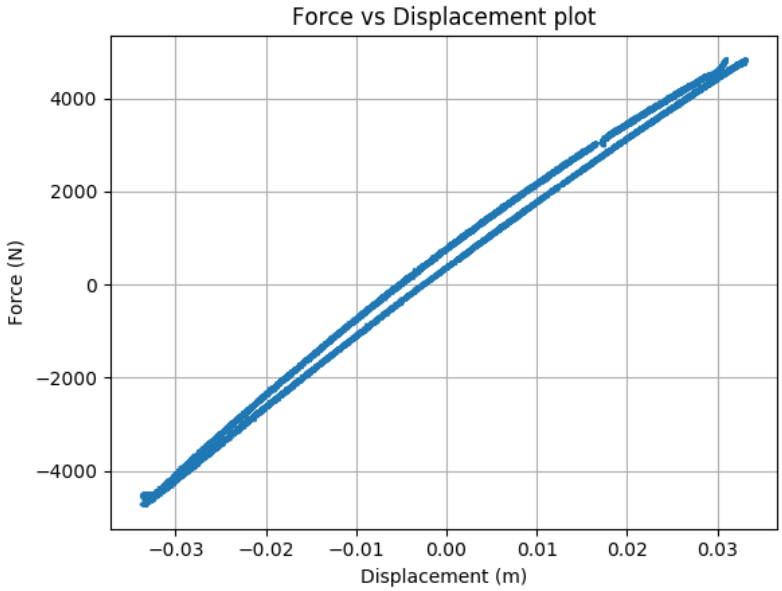

Figure 2-8 Plot showing the force-displacement curve of the experimental data for the uncut rubber buffer in the shear direction under quasi-static loading conditions.

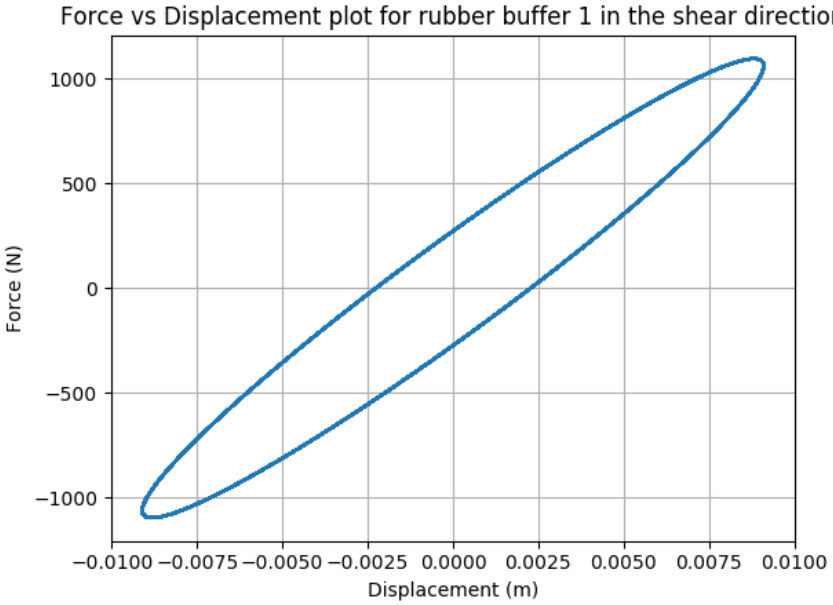

Figure 2-9 Plot showing the force-displacement curve of the experimental data for rubber buffer 1 in the shear direction under quasi-static loading conditions.

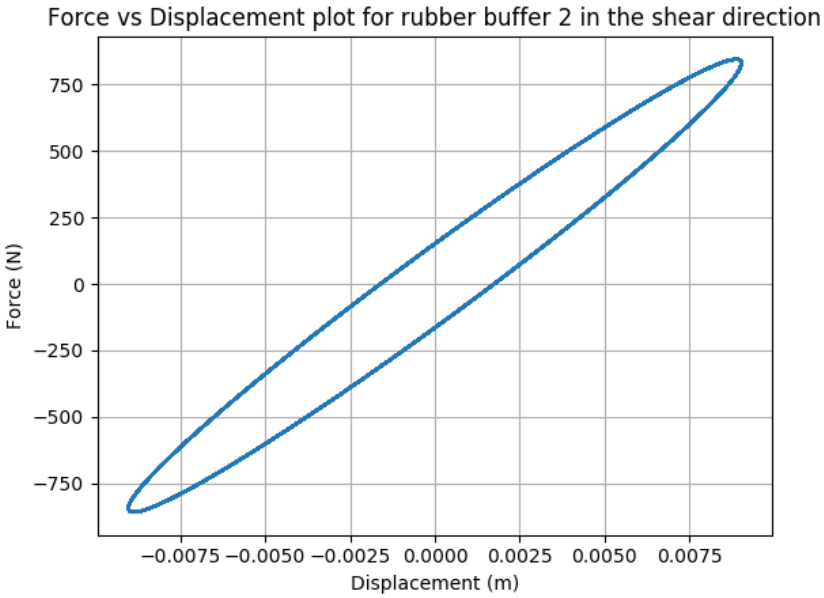

Figure 2-10 Plot showing the force-displacement curve of the experimental data for rubber buffer 2 in the shear direction under quasi-static loading conditions.

The characterisation of the rubber buffers was composed of two steps calculating the stiffness and the damping. The characterisation of the rubber buffers was done on the data from figures 2-5 to 2-10.

The stiffness was calculated using equation 2.2. This was done for both the normal and shear directions. The minimum and maximum displacement and stiffness values were used to ensure that the stiffness calculated was a good representation of the stiffness over the entire displacement domain.

$$k = \frac{\Delta F}{\Delta x} \tag{2.2}$$

The stiffness in the normal and shear directions for the uncut buffers was calculated to be 210 000N/m. The specified stiffness of the rubber buffer in the normal direction according to the manufacturer is 196 000N/m. The measured stiffness has an error of less than 1% from that of the specified value. Looking at table 1 it is noted that the stiffness in the shear direction is less than the normal direction. This is due to there being less material in the shear direction than in the normal direction. The cut down rubber buffers were less stiff than the uncut rubber buffer in both directions. Rubber buffer 2 was significantly less stiff than rubber buffer 1. This was due to rubber buffer 1 being cut 1mm thinner than rubber buffer 2.

The damping in the rubber buffer was measured by calculating the visco-elastic energy in the hysteresis loop. The visco-elastic energy is equal to the area enclosed in the loop. This was calculated using equations 1.3 to 1.5 as well as equation 2.3.

Table 1 Stiffness results for the rubber buffers.

Rubber buffer	**Stiffness in normal** (N/m)	**Stiffness in shear** (N/m)
Uncut rubber buffer	210 000	151 000
Rubber buffer 1	123 700	119 500
Rubber buffer 2	108 750	94 600

$$y_{max} = \frac{abs(\max(\text{disp}) - \min(\text{disp}))}{2} \tag{2.3}$$

The visco-elastic energy was calculated by fitting an ellipse to the force displacement data. The ellipse was broken up into two sections; where the ellipse has a positive gradient and where the ellipse has a negative gradient. The two parts of the ellipse were then integrated using the cumtrapz function in Python and subtracted from each other to get the area enclosed by the ellipse. This area was then used to calculate the damping using equation 1.5. The calculated damping values are shown in table 2. The damping values in the shear direction are larger than the damping values in the normal direction. This can be explained by the rubber buffer being longer in the vertical direction and thus when deformed in the shear direction, it is able to absorb more energy than that of the normal direction.

Table 2 Damping results for the rubber buffers.

Rubber buffer	**Damping in normal** (Ns/m)	**Damping in shear** (Ns/m)
Uncut rubber buffer	2 081	4 252
Rubber buffer 1	1 123	4546
Rubber buffer 2	478	2663

The response of the rubber buffer in the normal and shear directions was found to be linear and thus did not require further investigation in the form of non-linear models. For the sake of completeness, the uncut rubber buffer was fully characterised using non-linear models. The Young's modulus as well as the shear modulus of the rubber buffer were also calculated. The calculated stiffness and damping values were also used to solve the analytical equations of motion of a spring-mass-damper system. It

was found that the analytical equations solve for the displacement of the rubber buffers perfectly. These investigations as well as the results are included in appendix A.

2.1.3. Conclusion

Using the experimental data, the rubber buffers were characterised by approximating their stiffness and damping. It was found that the stiffness behaviour of the rubber buffers is linear. This greatly simplified the process of modelling the rubber buffers as spring elements could be used to model the rubber buffers in the FEM model. It was also found that the stiffness was greatly affected when the diameter was cut down.

2.2. Generation of the FEM Model of the Screen

With the characterisation of the rubber buffer complete, the next step was to model the vibratory screen in ANSYS. A CAD model of the VS-356 dewatering screen was provided by Weir Minerals. The CAD model was used as the basis of the model of the screen. It is noted that the screen is small in relation to screens which are more commonly used in industry. By the screen being small and compact, this results in the screen being significantly stiffer than larger screens. It was thus expected that there would only be small deviations from rigid body behaviour in the screen.

2.2.1. Importing and Modifying the Geometry

Before the process of generating the FEM model was conducted it was necessary to define a coordinate system which was used to define the orientation of the vibratory screen. The different sides of the screen were named to ensure that there was a conformal naming standard. This naming standard is shown below in figure 2-11.

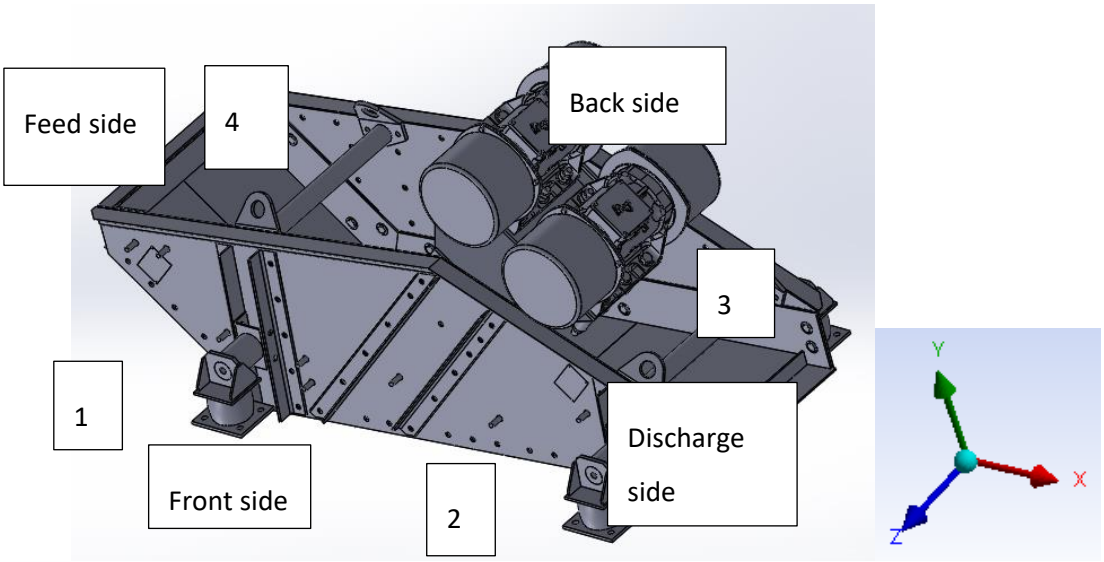

Figure 2-11 The naming standard of the screen which will be used throughout the report.

Before the screen could be modelled in ANSYS it was necessary to defeature the screen model. This was done by removing all the welds, holes and radii. The geometry was then simplified by removing the plastic mats, rubber lining and any other geometric features that were redundant in FEM simulations. Figure 2-12 shows the simplified CAD geometry of the vibratory screen with all the unnecessary features and components removed.

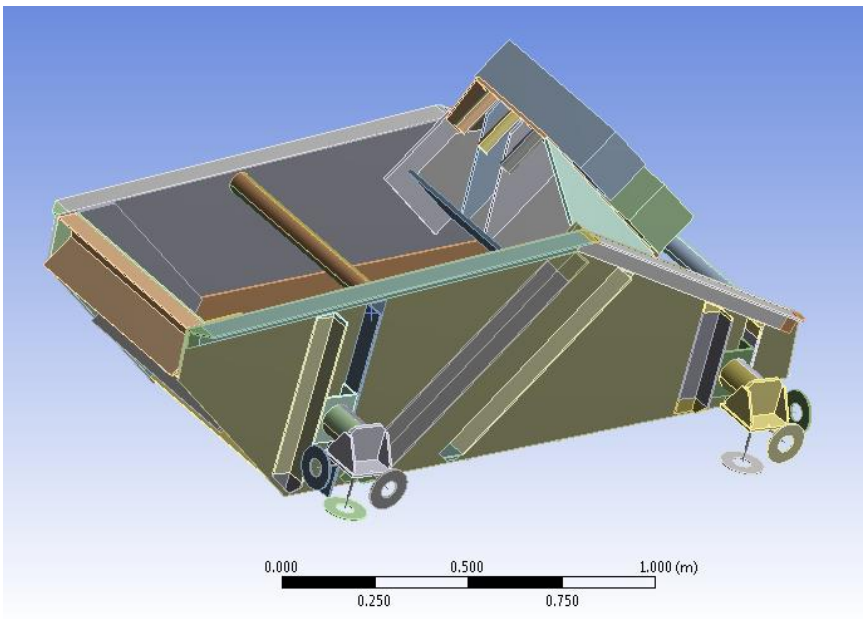

Figure 2-12 The simplified model of the vibratory screen in the FEM environment.

Once the geometry had been simplified the FEM model of the screen could be constructed in ANSYS. The first step was to import the geometry in INGS format. Next, SPACE CLAIME was used to clean up the geometry by simplifying edges, detecting missing faces, merging split edges and merging faces.

Once the geometry had been modified to ensure economical as well as accurate simulating, the next step was to add surfaces to the model for the spring elements to attach to. The surfaces were the same size as the contact regions between the screen and the rubber buffers. This was done to ensure that the force distribution in the FEM model was identical to that of the physical screen. It is noted that to represent the rubber buffers three sets of springs were used. This was done to ensure that the model was restrained in all three directions. The stiffness and damping values measured in section 2.1 were used.

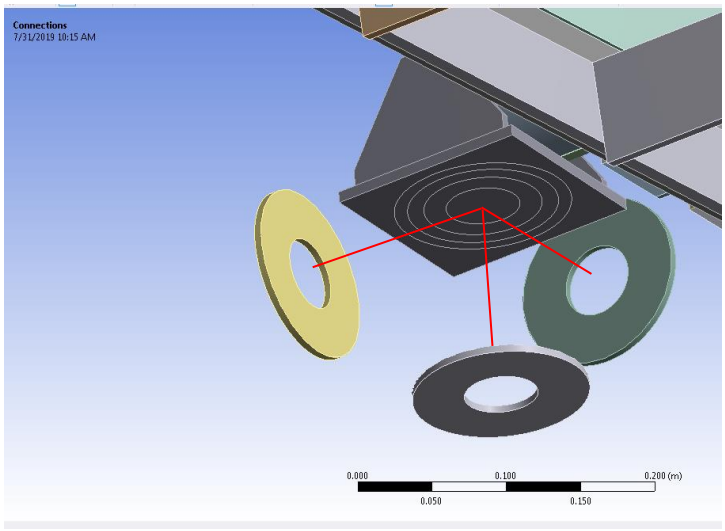

Figure 2-13 The locations where the springs are attached to in the FEM model.

The springs were connected to the screen as shown by the red lines in figure 2-13. Individual springs were used to represent the stiffness and damping of the rubber buffers in the X, Y and Z directions. The stiffness of the rubber buffers is the same in the Z and Y directions due to the rubber buffer being symmetric in the Z and Y directions.

One of the issues experienced in ANSYS was that the three springs could not be connected to the same surface. It was thus decided to split the surface into three concentric regions, each having the same area as shown in figure 2-13.

To ensure maximum accuracy from the FEM model it was necessary to split some of the more complicated geometries into bodies which were easier to mesh. The bodies which were split were all the cylindrical geometry as well as the L shaped plates on the sides of the screen. The cylindrical parts were split into 4 individual sweepable bodies as shown on the left of figure 2-14. The L shaped plates were then split so that the body could be meshed with quad elements and the more complicated geometry could be meshed with tetrahedron elements as shown on the right of figure 2-14.

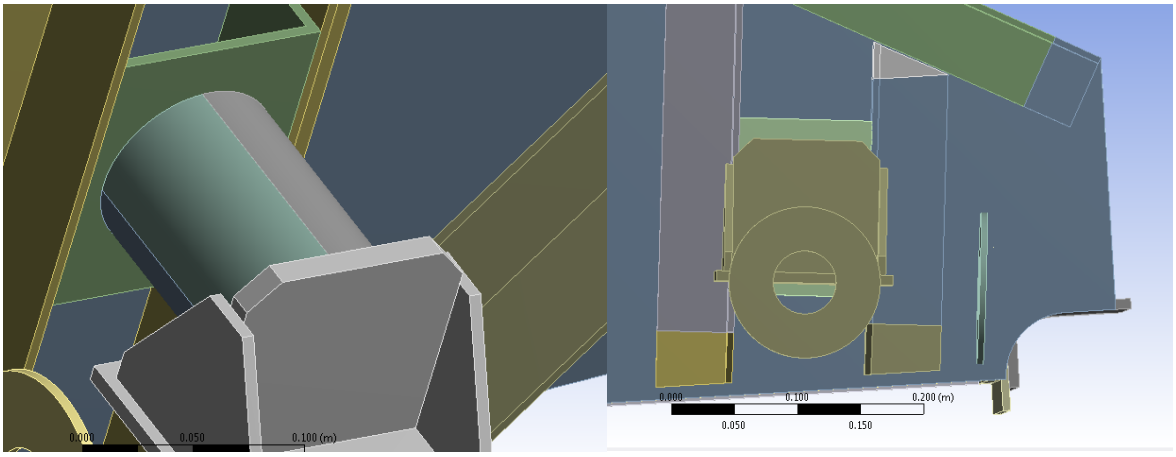

Figure 2-14 The way in which bodies were split up in order to more effectively mesh them.

During the simplification process, the eccentric motors were removed as their geometry was complicated. The two motors and eccentric weights were replaced by two lumped masses. The lumped masses were set so that the weight of the lumped masses ensured that the screen model had a total mass of 691kg.

2.2.2. Development of the Mechanical Model

In ANSYS Mechanical the appropriate materials were allocated to the screen. It is noted that in the geometry simplification section all the rubber components on the screen were removed as well as the motors. It was assumed that the remainder of the screen was composed of a single material. Structural steel S355 with material properties, E=200GPa and v=0.3 was used. These material properties are the same as structural steel in ANSYS.

Contact regions were automatically created in ANSYS, whereby all components which are in proximity were allocated a bonded contact region. Fixed supports were created on the outer surfaces of the plates shown in figure 2-13. This was a good approximation, as the lower frame of the screen on which the rubber buffers lie is isolated from the main screen deck. Standard gravitational acceleration of 9.81m/s^2 was applied to the model in the downward direction.

The mass distribution of the screen is also important as a significant amount of material was removed when the geometry was simplified. This resulted in a change in the centre of gravity of the screen. This was rectified by changing the size of the blocks which replaced the motors and eccentric weights. When the size of the blocks was changed it was important to change the density of the material allocation of the block to ensure that the mass of the screen remained constant.

The static loading conditions of the screen play a role in the solving of the model as well as the results. The springs in the vertical direction have a preload added to account for the static loading conditions of the screen. The preload value for the feed side of the screen was 1 883.5N and the preload at the discharge side was 1 510.7N. The values were obtained from a schematic of the screen provided by Weir Mineral.

The meshing of the screen is critical as the quality and size of the mesh has a large impact on the accuracy of the model. It was thus decided to use the orthogonal mesh quality as an indicator of how good the mesh is. Orthogonal quality is a method that is used to determine the quality of a given cell. The higher the orthogonal quality of a mesh, the better the stability and accuracy of the numerical computations.

First the model was meshed using the automatic mesher in ANSYS. This resulted in many of the bodies with simple geometries having good orthogonal quality. However, the bodies with more complicated geometry required remeshing. Multizone and tetrahedron elements were used to mesh the bodies with poor quality. Body sizing was also implemented to control the number of elements in each body. Manipulating the size of the mesh allowed the validity of the solutions to be investigated by reducing the size of the mesh until the solution results did not change. Figure 2-15 shows the final geometry as well as the mesh which were used in the simulations.

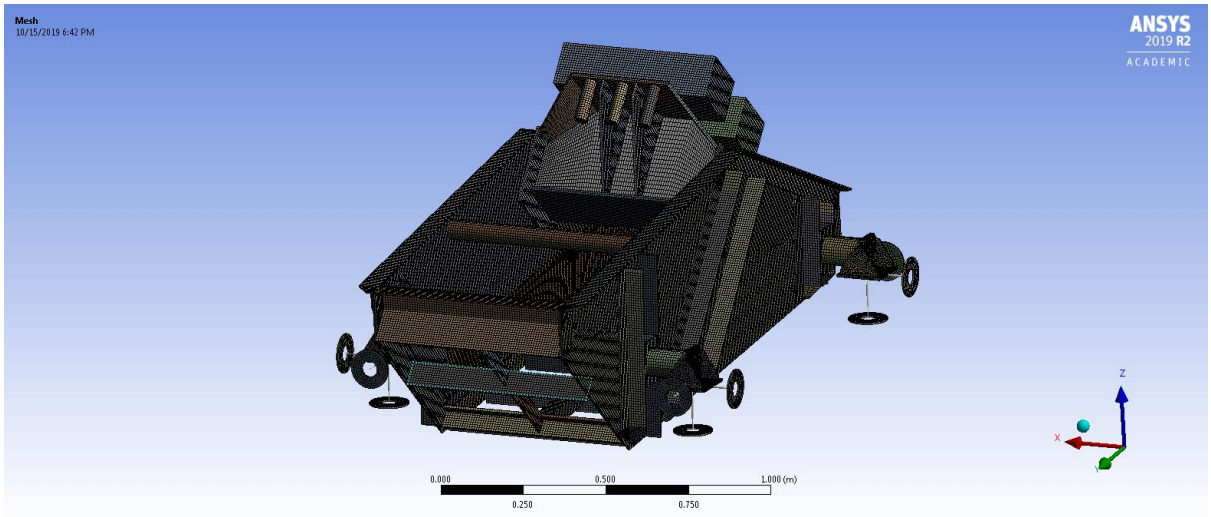

Figure 2-15 final mesh of the simplified screen geometry.

2.2.3. Modal Analysis

Once the FEM model of the screen was created, the next step was to perform a modal analysis on the FEM model. The aim of the modal analysis was to validate the physics of the FEM model against the

physics of the real model. This ensured that the stiffness, mass and geometry of the screen were correct. It was expected that the modal analysis would result in six rigid body modes and several flexible body modes.

To ensure that the modal analysis produced accurate modal results it was necessary to perform mesh refinement on the model. The goal of the mesh refinement was to make the mesh smaller until the modal frequencies converge.

Once the mesh refinement was completed, the simulation was run to calculate the first 9 modes. The first 9 modal frequencies are shown in table 3 below. The animated mode shapes of the model are shown below in figure 2-16 below.

Table 3 Modal frequency results from the FEM modal analysis.

Mode number	**1**	**2**	**3**	**4**	**5**	**6**	**7**	**8**	**9**
Frequency (Hz)	3.87	4.13	5.39	6.04	7.46	8.45	52.18	60.97	87.55

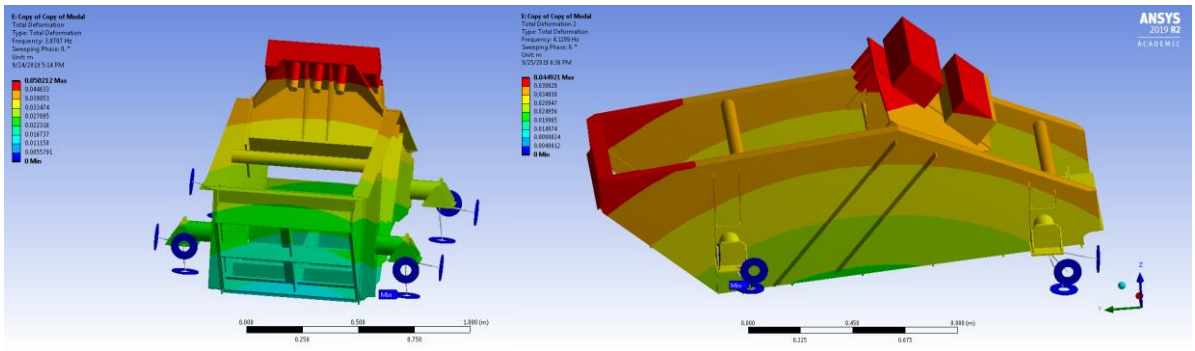

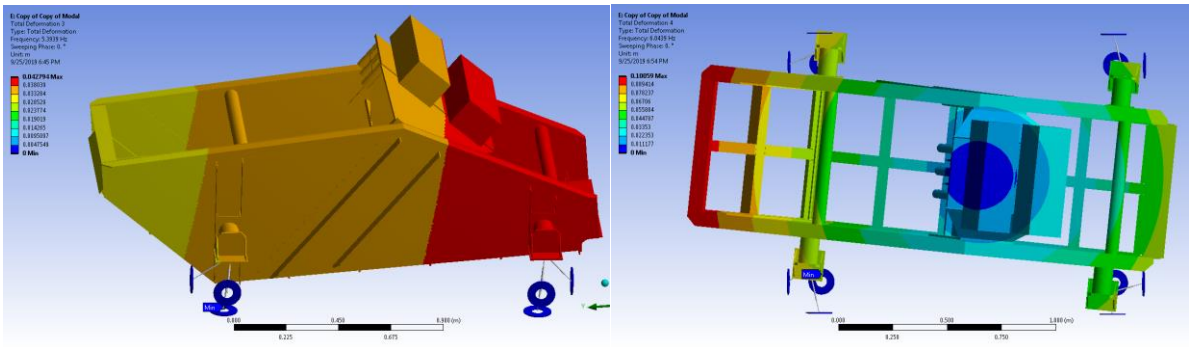

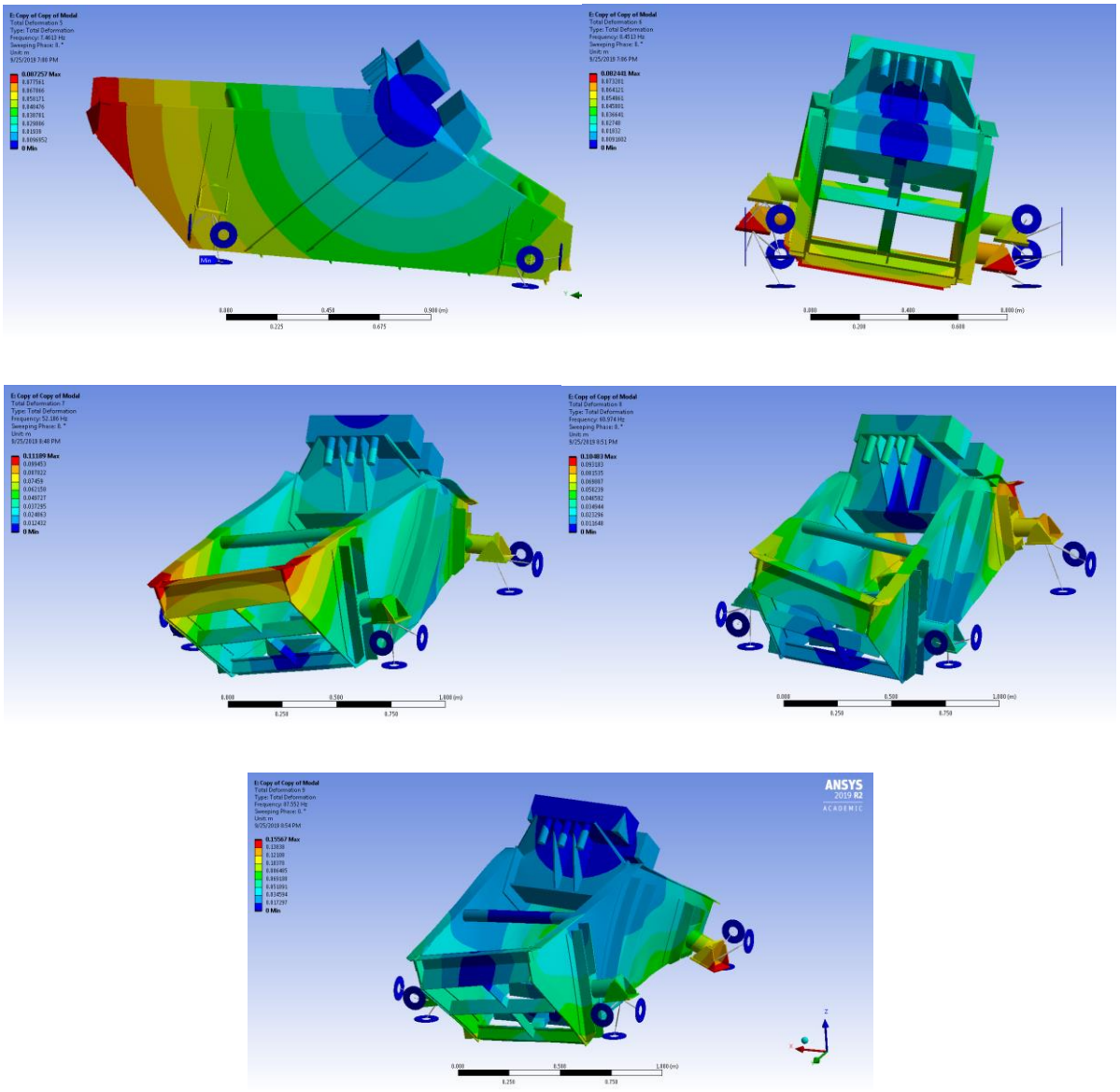

Figure 2-16 The animated mode shapes at their most extreme displacements for modes 1 to 9.

It can be seen from the mode shape results in figure 2-16 above that the first 3 modes are the rigid body translational modes. The next 3 modes are the rigid body rotational modes and the final 3 modes are flexible body modes. It was expected that the first 6 modes would be rigid body modes as the screen is very stiff. In the case of larger more flexible screens it is not uncommon to have some, of the flexible body modes come before the rigid modes.

These mode shape results were used later in the investigation to compare the results from the FEM modal analysis to the experimental modal analysis.

Once the meshing of the screen was completed and the orthogonal quality was of a desired value, the next step was to add the forces produced by the eccentric weights and motors.

Two Invicta FBL40-16/6 vibrators were used to excite the vibratory screen. A schematic diagram of the vibrator is shown in Figure 2-17.

The centrifugal force generated by the vibrator was found to be 15 323N according to figure 2-18. This force was broken up into components below using the inclination of the vibrating motors relative to the horizontal.

$$F_y = 15\,323 \cdot \sin(50°) = 11\,728N$$

$$F_x = 15\,323 \cdot \cos(50°) = 9\,949N$$

It is noted that the mass rotated in a circular motion. Therefore, the force is a time dependent sinusoidal function. Two identical vibrators as shown in figure 2-17 were used to excite the screen thus the force was multiplied by two. This was done as the two exciters rotate in opposite directions e.g. one rotates clockwise and the other counterclockwise.

$$F_y = -23\,476 \cdot \sin(100.531 \cdot t)\ N$$

$$F_x = 19\,700 \cdot \sin(100.531 \cdot t)\ N$$

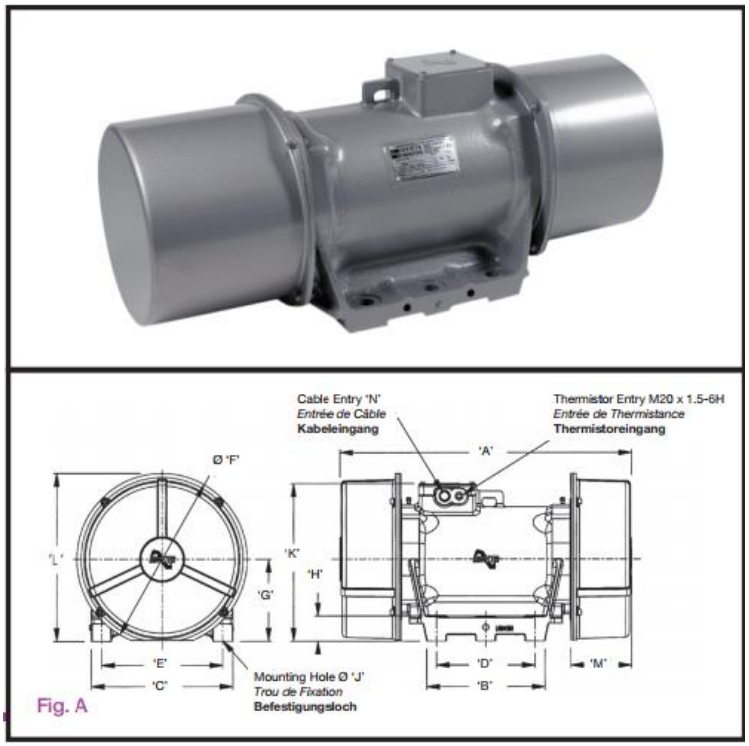

Figure 2-17 Schematic diagram and image of the Invicta vibrator (FBL Series VIBRATORS, 2017).

Description *Description* **Beschreibung**			Mechanical Specification *Spécifications Mécaniques* **Mechanische Spezifikation**						Electrical Specification *Spécifications Électriques* **Elektrische Daten**		
Frame Size *Type* **Gehäusegröße**			Centrifugal Force *Force Centrifuge* **Fliehkraft**		Working Moment *Moment de Travail* **Arbeitsmoment** Kg.cm. (x2)		Weight *Poids* **Gewicht** (Kg)		Watts *Puissance* **Leistung**		Full Load Current *Le Courant plein de Chargement* **Volle Lastströmung** 400v
			Kg	Newtons	50 Hz.	60 Hz.	50 Hz.	60 Hz.	Input *D'entré* **Auf**	Output *De Sortie* **Ab**	50 Hz.
FBL25	-8/6		792	7769	154	-	57*	-	747	510	1.6
FBL30	-11/6		1081	10605	210	150	89*	86*	1165	900	3
FBL30	-15/6	◊	1490	14617	-	201	-	95*	1165	900	3
FBL30	-18/6		1757	17236	341	-	102*	-	1165	900	3
FBL40	-16/6		1562	15323	303	-	119*	-	2290	1800	5
FBL 40	-23/6	◊	2341	22965	-	319	-	131*	2290	1800	-
FBL 40	-23/6	Q5	2341	22965	-	319	-	131*	2290	1800	-
FBLz 40	-25/6		2568	25195	498	-	139	-	2290	1800	5
FBLz 40	-27/6		2699	26477	524	-	145*	-	2290	1800	5
FBLz 40	-35/6		3500	34335	680	468	154	147	2290	1800	5
FBL 40	-38/6	◊	3770	36990	-	508	-	144*	tba	tba	-
FBLz 45	-42/6		4200	41202	815	566	195	185	2690	2310	6.3
FBLz 45	-50/6		5000	49050	970	673	209	200	2690	2310	6.3
FBL50	-38/6		3710	36395	720	500	268*	258*	4530	4000	8.8
FBL50	-38/6	Q5	3710	36396	720	500	268*	258*	4530	4000	8.8
FBL50	-42/6		4202	41222	816	-	274*	-	4530	4000	8.8
FBL50	-42/6	Q5	4202	41222	816	-	260	-	4530	4000	8.8
FBLz 50	-60/6		5985	58716	1174	820	300	289	4530	4000	8.8
FBLz 50	-72/6		7200	70632	1398	971	312	298	4530	4000	8.8

Figure 2-18 Invicta vibrator catalogue (FBL Series VIBRATORS, 2017).

3. Experimental Investigation

Experiments were conducted on the vibratory screen; these experiments involved the modal analysis of the screen as well as experiments on the screen while it was running. The aim of the experiments was to gather information about the dynamics of the screen so that the FEM model of the screen could be validated correctly.

3.1. Modal Analysis

The aim of the modal analysis was to extract the modal frequencies as well as the mode shapes from the physical screen. It is important to note that to ensure that the all the mode shapes and frequencies were measured correctly the tests were performed at different locations on the screen. This ensured that the data gave a good indication of the nature of the mode shapes and negated the possibilities of measuring on a modal line where the displacement of the screen is zero.

The modal analysis was conducted by means of an impact hammer test. The impact hammer test was chosen for its simplicity and the ease of measuring at different locations on the screen. The selection of the impact hammer was important as the size of the impact hammer as well as the impact tip determine the frequency range at which the screen was excited. For the modal analysis, the largest modal hammer was selected combined with the softest modal hammer tip. This selection was made as the frequency response of the screen was expected to be in the conservative frequency range of 0Hz-200Hz. This interval was selected based on the data from the modal analysis on the FEM model where the 9^{th} mode was found to be at 87Hz.

To ensure that the modal analysis was accurate and provided enough information about the mode frequencies as well as the mode shapes the location of the impact as well as the location of the accelerometer were varied. To enhance the placement of the accelerometer as well as the locations where the modal hammer would impact it was first necessary to bear in mind the nature of the mode shapes. The accelerometer locations on the screen are shown in figure 3-1 below. These locations were chosen to ensure that the mode shapes and frequencies were captured from the experimental modal analysis.

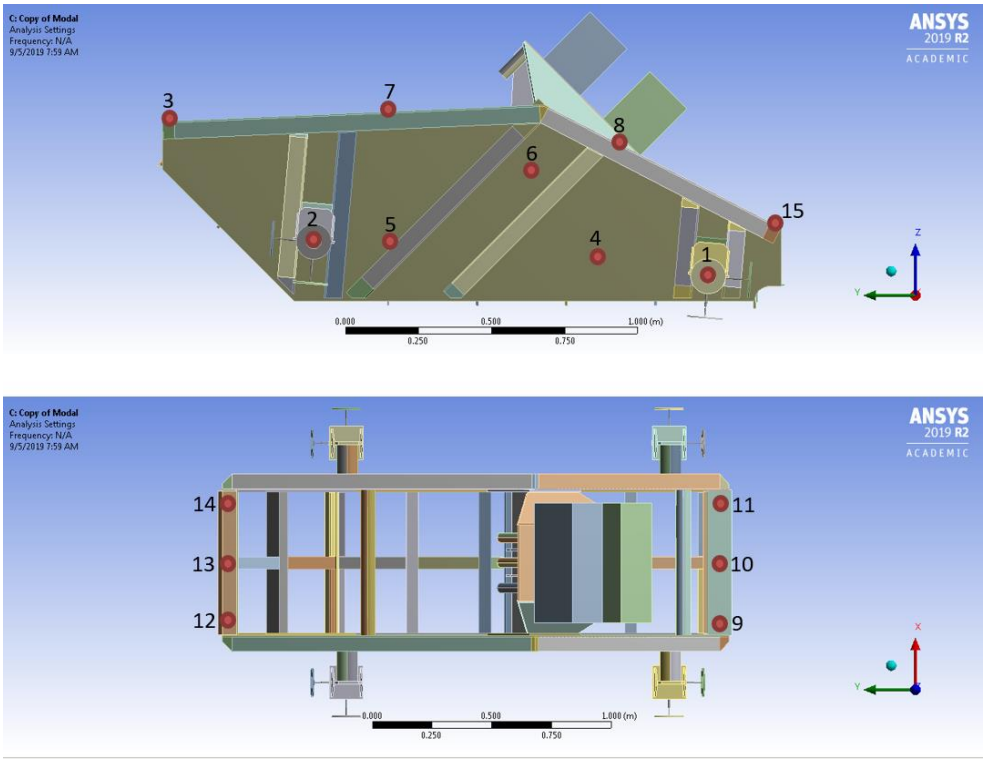

Figure 3-1 The locations of the accelerometer for the modal investigation of the screen.

It was expected that the rigid body modal frequencies of the screen would be less than the operating frequency of the screen as was found in the FEM modal analysis. A preliminary investigation was conducted to determine the best frequency range to conduct the investigation over.

The impact points of the modal hammer were also varied. The procedure used to select the locations where the screen was hit in relation to the accelerometer was done in a way to maximize the amount of information gathered about the different modes and their shapes. There were between 4 and 5 different locations selected to impact the screen for each of the different accelerometer placements. The selection of the impact locations followed the following general parameters; impact the screen in a location which is close to the accelerometer in the X, Y and Z directions and the opposite side of the screen. The general idea behind these locations was to excite the rigid body modes by hitting it in the three different planes as well as excite the flexible body modes.

Apparatus:

1. Vibratory screen
2. PCB 086D50 12lb modal hammer with the soft tip
3. CoCo-80X Dynamic signal analyser
4. Dytran 3263A1 6368 triaxial accelerometer
5. Wax to mount the accelerometer

Figures 3-2 to 3-4 show the apparatus used in the modal analysis. This setup was implemented for all the tests and was kept the same for the whole investigation.

Figure 3-2 The modal hammer and the triaxial accelerometer.

Figure 3-3 How the accelerometers are mounted on the screen.

Before the modal analysis was conducted it was necessary to do tests to ensure that the parameters were set up correctly. The preliminary investigation was composed of selecting a valid block size for the test as well as establishing a frequency range to measure over.

Setting up of the CoCo-80X was done by setting it to the Frequency Response Function (FRF) mode. The FRF was used as it allowed for manual frequency response analysis of the screen. Next, the block size needed was investigated. The size of the block was determined by investigating how long it took for an impact of the hammer on the screen to dissipate. This was done by simply plotting the displacement response of the screen after an impact by the modal hammer. The plots shown in figure 3-5 show the force measured by the modal hammer as well as the response of the screen in the X, Y and Z directions. The readings of the force and displacement were set to be measured with a delay of

0.1s before the impact of the hammer. This was done to ensure that no information was lost in the timeframe from the impact until the CoCo started measuring.

Figure 3-4 CoCo-80X Dynamic signal analyser.

It can be seen from figure 3-5 that the force measured by the hammer is very close to an impulse. It is noted that the force experienced by the hammer after the initial impact can be attributed to the stopping motion of the hammer after the impact. Figures 3-5 show that the responses of the screen dissipated entirely after 4.5s. It was decided that a block that spanned 5s would be best for the modal analysis. A block size of 1024 was used with a sampling rate of 200Hz. A Force-Exponential window was used to sample the signal and the results were averaged over 4 modal hammer impacts. The settings used in the experiments are shown in table 4 below.

Determining the frequency range of interest was done by placing the accelerometer at a few locations around the screen and measuring the frequency response of the screen. This was performed using frequency bands ranging from 500Hz to 50Hz. It was found that a frequency band from 0Hz to 88Hz captures enough information to perform the modal analysis. The results from one of the investigations are shown in figure 3-6. The peaks in the magnitude plot correspond well to changes of phase in the phase plot. It is noted that there also appear to be many spikes in the low and middle frequency phase domain. This can be attributed to the wrapping.

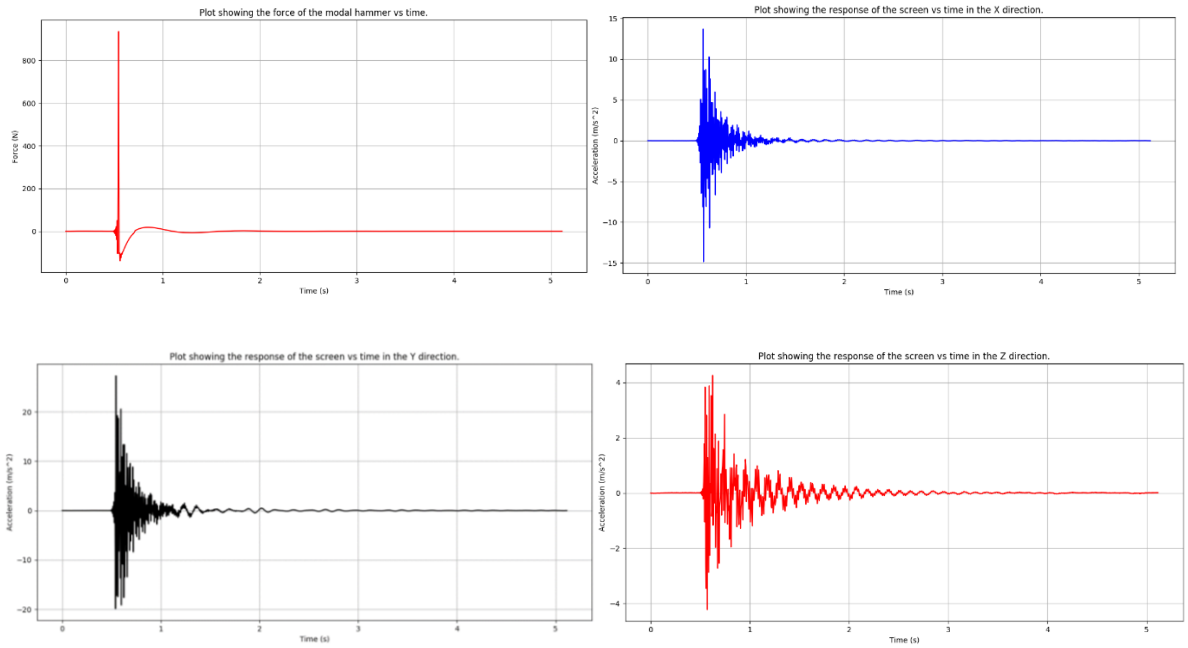

Figure 3-5 Plots showing the force signal and the X, Y and Z accelerometer readings for a measurement block.

Table 4 Settings for the CoCo-80X.

Block size	1024
Window type	Force exponential
Sampling frequency	200Hz
Frequency range	88Hz
Average number	4
Accelerometer sensitivity X-direction	10.33mV/g
Accelerometer sensitivity Y-direction	10.56mV/g
Accelerometer sensitivity Z-direction	10.84mV/g

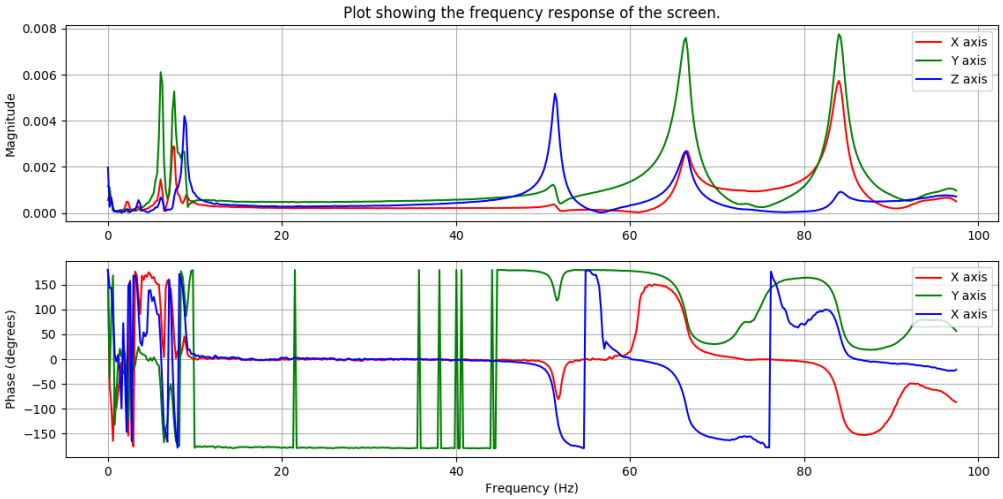

Figure 3-6 FRF showing the X, Y and X readings from an impact on a screen.

The procedure used for conducting the modal analysis on the vibratory screen is as follows:

1. Prepare the surface where the accelerometer will be placed by cleaning any residue, oil or contaminants which could have an impact on the readings.
2. Apply a thin layer of the wax to the accelerometer and attach it to the surface of the first measurement location.
3. Set the CoCo to wait for the trigger and impact the screen at the desired location.
4. It is important to ensure that the impact by the modal hammer is clean as to reduce the amount of noise in the system. This was done by analysing the force impact of the hammer vs time which was displayed on the screen of the CoCo once the block has been measured.
5. If the impact of the modal hammer is good, the next reading can be taken by repeating steps 3 and 4. If the impact is not good enough then, data block must be rejected and steps 3 and 4 must be conducted again.
6. Once 4 sets of good impact have been collected the results can be saved.
7. Steps 3 to 6 are conducted for each of the decided locations to hit the screen with the modal hammer.
8. Once the data from the different impact locations have been saved, the accelerometer is moved to the next position and the steps are repeated until all the accelerometer locations have been investigated.

3.2. Dynamic Investigation of the Vibratory Screen

The dynamic investigations of the screen were performed to gather experimental information about the response of the screen under different rubber buffer stiffness and loading configurations. The run-up and run-down response of the screen was also measured.

These measurements were conducted for several reasons; to validate the dynamic response of the screen so that it could be compared to the FEM model as well as provide data about the response of the screen to train an intelligent system.

3.2.1. Investigation of the Response with Unique Rubber Buffer Characteristics

The objectives of performing these experiments was to gather information about the response of the vibratory screen when different stiffness rubber buffers were used. These results were used to better the response results of the FEM model to ensure that the FEM model could replicate the physics of the screen.

The experiments on the screen involved measuring the response of the four corners of the screen under start-up, steady state operation and the run-down of the screen. The responses were measured for different stiffness configurations of the rubber buffers.

The rubber buffer configurations investigated included a base run where all the rubber buffers were the same stiffness, replacing one of the rubber buffers on each of the 4 corners of the screen and all the possible stiffness configurations possible with two cut down rubber buffers and two normal stiffness rubber buffers.

To gather a large amount of information about the dynamic response of the vibratory screen it was important to select an appropriate simulation time. It was decided to use a total measuring time of approximately 6 minutes. This duration was selected as it allowed for approximately 5 minutes of steady state operation in between the run-up and run-down of the screen.

It is noted that the CoCo can only measure 8 channels at the same time. This led to problems whereby if triaxial accelerometers were placed on each corner of the screen, 12 channels would be required. It was thus decided to rove a single triaxial accelerometer around the 4 corners of the screen. The settings used for the transient analysis in the CoCo are show in table 5. A sampling frequency of 1000Hz was selected as the data gathered was used to train the intelligent system as well as validate the model of the screen. Thus, it was necessary to have a signal with a high resolution to ensure better classification and to aid in accurately validating the FEM model.

Table 5 Settings for the CoCo-80X.

Sampling frequency	1000Hz
Accelerometer sensitivity X-direction	10.33mV/g
Accelerometer sensitivity Y-direction	10.56mV/g
Accelerometer sensitivity Z-direction	10.84mV/g

Apparatus:

1. Vibratory screen
2. 2x cut down rubber buffers
3. Jack to lift the screen
4. CoCo-80X Dynamic signal analyser
5. Dytran 3263A1 6368 triaxial accelerometer
6. Wax to mount the accelerometer

Experimental Procedure to Conduct the Dynamic Analysis:

The procedure used for conducting the dynamic analysis on the vibratory screen is as follows:

1. Prepare the surface where the accelerometer will be placed by cleaning any residue, oil or contaminants which could have an impact on the readings.
2. Apply a thin layer of the wax to the accelerometer and attach it to the surface of the first measurement location.
3. Click record on the CoCo.
4. Switch on the screen.
5. Once the timer on the CoCo has reached 5 minutes turn the screen off at the wall.
6. Wait for the screen to entirely stop, this can be monitored using the display on the CoCo.
7. Once the screen has completely stopped save the data from the simulation.
8. Complete steps 1 to 7 for all 4 corners of the screen.
9. Once the data has been saved for all the corners the next step is to lift the screen using the jack and replace one of the normal rubber buffers with a cut down rubber buffer.
10. Complete steps 1 to 9 for all the different rubber buffer configurations.

3.2.2. Experiment of the Loaded Screen

The investigation of the effects of material was done to get a better understanding of whether it was possible to distinguish between different material loading configurations. This investigation was conducted using the uncut rubber buffers as it was expected that most screening operations in industry would be conducted on a screen without faults.

It was decided that the best way to simulate the effects of material over the screen deck was to load the screen with metal plates. This decision was made as the plates were a lot easier to control than a more realistic material like sand or rocks. The plates also gave a close representation of material over the screen.

The metal plates used are shown in figure 3-8. The dimensions of the plates are 356 x 356 x 50mm with a mass of 49kg each.

Different loading conditions were simulated using seven different loading conditions. These loading conditions are: 1 weight at the feed, 1 weight in the middle, 1 weight at the discharge, 1 weight at the feed and 1 weight at the discharge, 1 weight in the middle and 1 weight at the feed, 1 weight in the middle and 1 weight at the discharge and lastly 1 weight at the feed 1 weight at the middle and 1 weight at the discharge.

It was necessary to keep the plates secure in their location during the duration of the experiments. This was done by securing two ropes to the plates as shown in figure 3-8. The ropes were then tied to the frame at the feed end. It is noted that by using ropes, it allowed the plates to bounce and move small amounts over the screen deck. This created a more realistic simulation of material over the screen deck as opposed to fixing the plates rigidly to the screen deck.

Apparatus:

1. Vibratory screen
2. 3x metal plates
3. Rope
4. CoCo-80X Dynamic signal analyser
5. Dytran 3263A1 6368 triaxial accelerometer
6. Wax to mount the accelerometer

Figure 3-7 Loading of the screen with the plates and how the plates are attached to the screen.

The procedure for the dynamic analysis on the vibratory screen with the weights is as follows:

1. Place the plate on the screen at the first location and secure the plate to the screen using ropes.

2. Prepare the surface where the accelerometer will be placed by cleaning any residue, oil or contaminants which could have an impact on the readings.
3. Apply a thin layer of the wax to the accelerometer and attach it to the surface of the first measurement location.
4. Click record on the CoCo.
5. Switch on the screen.
6. Once the timer on the CoCo has reached 2 minutes turn the screen off at the wall.
7. Wait for the screen to entirely stop, this can be monitored on the display of the CoCo.
8. Once the screen has completely stopped save the data from the simulation.
9. Complete steps 2 to 8 for all 4 corners of the screen.
10. Once the data has been saved for all the corners the next step is to load the screen with the next metal plate loading configuration
11. Complete steps 1 to 10 for all the different screen loading configurations.

The configuration of the CoCo and the accelerometer sensitivities are the same as for the dynamic investigation with the less stiff rubber buffers in table 5.

It is noted that the results from the above experiments on the screen were in the form of acceleration values. These values needed to be integrated to get displacement values. It was necessary to ensure that the calculated displacement values correlate with the displacement of the screen. This was done with the aid of a laser displacement transducer. The experimental procedure and the calibration of the displacement data is included in appendix B.

4. Results

In this section the results from the experimental analysis are processed and reviewed. The results from the modal analysis were processed and used to validate the results produced by the modal analysis of the FEM model. Next, the data from the dynamic investigation on the screen was processed. The results from the dynamic investigation were then used to correlate and validate the results from the transient analysis of the FEM model of the screen.

4.1. Results from the Modal Analysis

After the completion of the modal analysis it was necessary to extract the resonant frequencies as well as the mode shapes from the data. The data from the CoCo was in the form of a CSV document which was opened using Python. The data from each of the impacts by the modal hammer was in the form of the block data from each of the 4 channels (force, X acceleration, Y acceleration and Z acceleration). The file also included 3 frequency response functions calculated using the responses in the three directions and the force measured by the modal hammer. The frequency response function data in each of the three directions included the frequency, magnitude and phase information. The data was plotted using two graphs, namely the magnitude and the phase graphs. Both graphs have the frequency on the X axis and the magnitude or phase on the Y axis.

Once the data had been extracted and plotted the next step was to identify the resonant frequencies from the frequency response functions. This was done by looking at the magnitude and phase plots and identifying peaks in the magnitude plot. It was also important to ensure that there was a phase change associated with each of the different peaks in the magnitude plot. Figure 4-1 shows an example of a frequency response function measured in the experiments.

From FRF data the resonant frequencies were read off from the plots. The resonant frequencies are displayed in table 6 with the results from the FEM modal analysis. The mode results from the FEM model and the experimental results were compared further down in this section.

One aspect that was noted from the modal analysis was that there is a large gap in the frequency domain between the rigid modes and the flexible modes. This was expected as the operating frequency of the screen is 16Hz. This was part of the design of the screen to ensure that the resonant frequencies are as far as possible from the operating frequency. This ensures that the screen can operate in a controlled and predictable manner.

By looking at table 6 there are some small differences in the modal frequencies between the experimental results and the FEM results. This can be attributed to a few reasons, such as asymmetries in the physical screen, differences in the stiffness of the screen deck and the FEM model, differences in the geometry between the FEM model and the physical screen due to the simplification of the FEM geometry and small differences in the stiffnesses of the rubber buffers.

Table 6 Modal frequency results from the experimental and FEM modal analysis.

Mode number		**1**	**2**	**3**	**4**	**5**	**6**	**7**	**8**	**9**
Frequency (Hz)	Experimental	2.2	3.3	5.2	6.1	7.6	8.9	51.6	66.7	83.8
	FEM	3.87	4.13	5.39	6.04	7.46	8.45	52.18	60.97	87.55

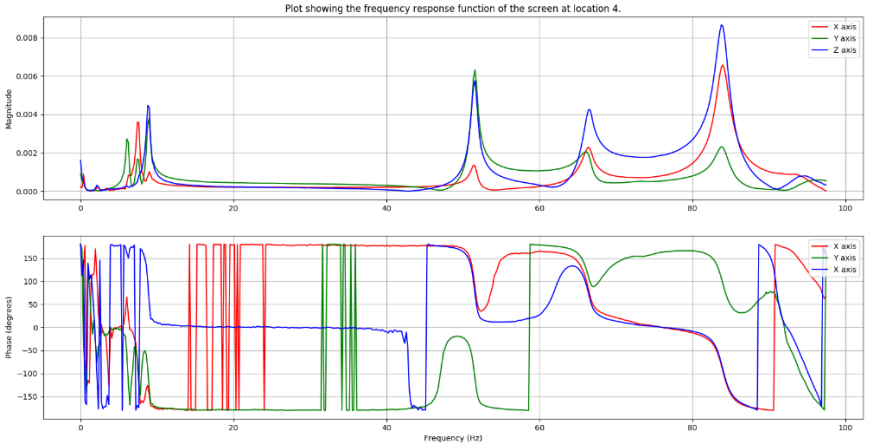

Figure 4-1 Results from the experimental modal analysis showing peaks and phase change of the different modes.

Once the modal analysis experiments had been investigated for the physical model the next step was to ensure that the modal analysis results from the FEM model correlate. The correlation of the experimental results and the FEM model was done in two ways: by matching the resonant frequencies and ensuring that the mode shapes correlate. Table 7 describes the mode shapes produced by the FEM model.

The procedure to investigate the correlation of the mode shapes was to correlate the mode shapes produced by the FEM model to that of the peaks measured in the modal analysis on the physical screen. This was done by ensuring that the motions of the various modes correlate to the expected peaks in the modal data.

Once the shapes of the FEM modal analysis were established the next step was to investigate the peaks for the different accelerometer placements on the physical screen to establish a correlation between the FEM model and the physical model. This section is included in appendix C. It was found that the mode shapes of the FEM modal and the experimental results corelate well.

Table 7 The modes shapes from the FEM modal analysis.

Mode	FEM model shape
1	Rigid body translational mode along the Z-axis
2	Rigid body translational mode along the X-axis
3	Rigid body translational mode along the Y-axis
4	Rigid body rotational mode about the Y-axis
5	Rigid body rotational mode about the Z-axis
6	Rigid body rotational mode about the X-axis
7	Flexible body mode
8	Flexible body mode
9	Flexible body mode

4.2. Results from the Dynamic Analysis

In this section the results from the dynamic investigation on the screen were processed and investigated. Once the results had been validated the next step was to compare the response of the physical screen to that of the FEM model. If the dynamic response of FEM model and the physical screen did not correlate this was rectified by modifying the loads on the FEM model so that the uncut rubber buffer results from the physical screen and the FEM model correlate.

It was necessary to ensure that the integrated results from the dynamic investigation using the accelerometer represented the displacement of the screen correctly. This was done by comparing the integrated displacement data to the displacement data from the laser displacement transducer in the Y direction.

The first step in processing the laser transducer data was to ensure that the data was calibrated. To calibrate the laser transducer data the results from the calibration experiment were used to determine a function between the laser transducer voltage output and the displacement in millimetres. Figure 4-2 shows the result from the calibration of the laser transducer. It is noted that the relationship between the voltage and displacement is linear with a gradient of 5.2mm/V. The results from the experiments using the laser transducer were multiplied by the gradient to convert the readings to millimetres.

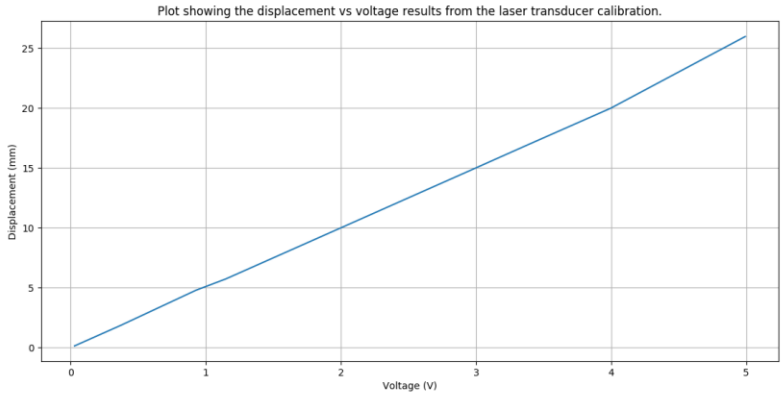

Figure 4-2 Calibration results for the laser displacement transducer.

To extract the displacement data from the accelerometer data it was necessary to integrate the data twice. Upon integrating the data using the built-in integration function in Python it was found that there was a DC offset occurring with the displacement data. This was solved by using numerical FFT integration.

Numerical FFT integration is a tool used to eliminate the DC offset found when integrating accelerometer data. When using the numerical FFT integration it is important to ensure that the low frequency cut-off value is selected correctly. The low frequency cut-off value in the frequency domain integration is important as it allows for the DC offset to be removed from the signal. However, it is important to ensure that the frequency used is low enough to preserve critical signal information.

To ensure that the signal investigated was a true response of the dynamics of the screen it was necessary to filter the signals. The signal filtering was done with the aid of a Butterworth bandpass filter.

The Butterworth bandpass filter removed all the frequency information that did not fall in the region of interest. The same rational applied for the low cut-off frequency in the Butterworth filter as in the low cut-off frequency for the FFT integrator. The high cut-off frequency for the Butterworth filter was to ensure that high frequency noise does not compromise the data.

The next step after correctly integrating the acceleration data to displacement data was to validate the displacements against the results obtained from the laser displacement transducer. The filter frequencies of both the FFT integrator and the Butterworth filter were adjusted to ensure that the start-up and run-down displacements matched up. The low frequency cut-off for the FFT integrator was selected to be 1.2Hz and the Butterworth bandpass filter low and high frequency cut-off values were selected as 3Hz and 95Hz. By ensuring that the start-up and run-down peaks match up this

showed that low frequency aspects of the signal were preserved. This can be seen in figure 4-3. It is noted that the duration of the two experiments were not the same.

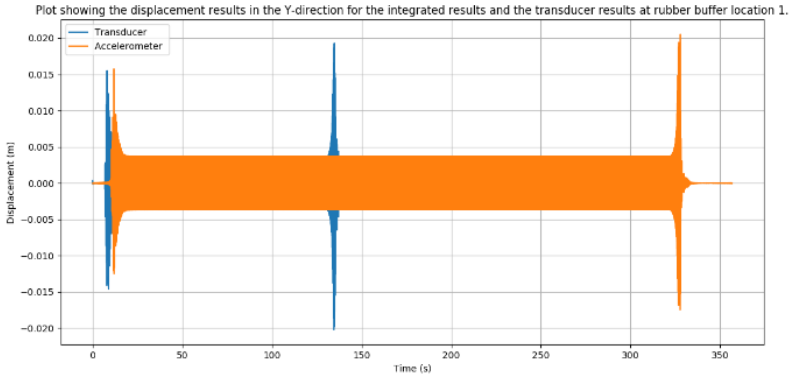

Figure 4-3 The data from the accelerometer and the laser displacement transducer showing how the peaks correlate.

Upon completing the above process, it was found that the displacement values from the accelerometer and the laser displacement transducer were slightly out. This was rectified by multiplying the accelerometer displacement value by a scaling constant of 0.96. The unscaled and scaled results are shown in figure 4-4 below. Figure 4-4 only shows the data at rubber buffer location 1. This procedure was completed for all 4 rubber buffer locations.

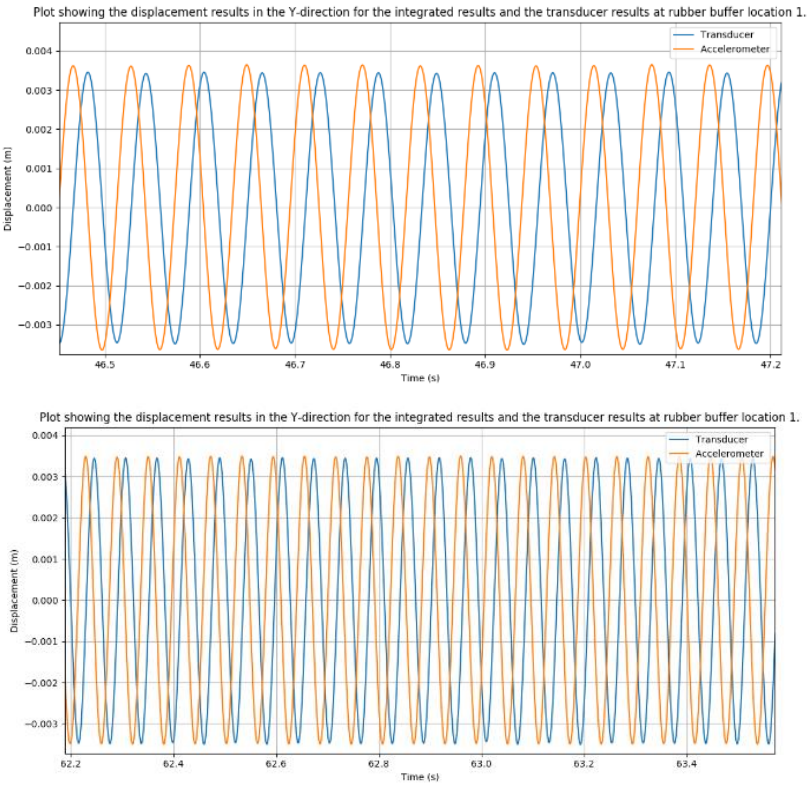

Figure 4-4 The scaled and unscaled results for rubber buffer location 1.

It is noted from the figures above that the locations of the peaks do not align. This is due to the readings coming from different signals taken at different times. The signals were simply plotted together to compare the scaling of the displacement results.

The filtered, integrated and scaled accelerometer results are shown in figure 4-5. The top graph shows the whole displacement signal measured at rubber buffer location 1 in the X, Y and Z directions. It is noted that the transient regions at the beginning and end of the signal represent the run-up and run-down sections of the signal. The graph at the bottom is a zoomed in region of steady state response of the top graph. The displacement in the X and Y directions are much larger than the displacement in the Z direction. This is attributed to the screen being excited in the X-Y plane. It is also noted that the X and Y displacement values are 180° out of phase. This is required to transport the material over the screen deck from the feed to the discharge.

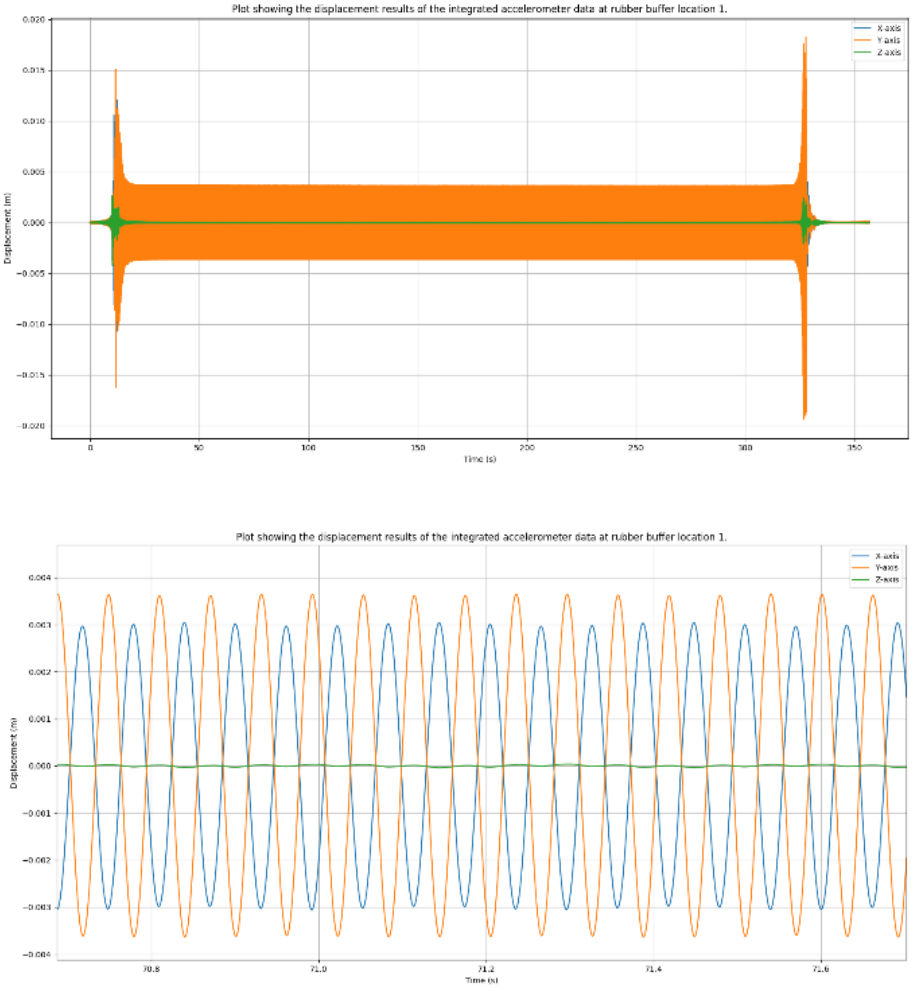

Figure 4-5 Acceleration, velocity and displacement results from the filtered and scaled accelerometer data.

One of the largest problems encountered was that the response of the screen was not symmetric. In the case of a perfectly symmetric screen the response measured at both rubber buffers on the feed

side of the screen will be identical. The same can be said for the rubber buffers on the discharge side of the screen. These differences are shown in figure 4-6. The discharge side displacement values match up well in the X and Z directions but there is a clear discrepancy in the Y direction. The results for the feed side of the screen are different in all the directions.

These discrepancies resulted in issues with the comparison of the FEM model displacements as well as attempting to classify the experimental data using an intelligent system trained on the FEM data.

This can be caused by several reasons such as manufacturing discrepancies, inexact stiffness values of the rubber buffers and general wear and tear on the screen. One manufacturing problem that was noticed on the vibratory screen was that the frame on which the screen sits was manufactured at different heights. This resulted in the screen not being even on its supports. This was rectified by inserting steel plates under the rubber buffers to ensure that the screen was level and that the rubber buffers compressed equal amounts.

The response of the screen not being symmetric was something that could not be controlled and was bound to have negative effects on the comparison of the FEM model to the experimental results. However, this was the only option other than getting a new screen, which was impossible.

After the completion of the dynamic analysis experiments the next step was to process the data. The data from the CoCo was in the form of a CSV document which was opened using Python. The data from each of the dynamic investigations was in the form of the block data from each of the 3 channels (X acceleration, Y acceleration and Z acceleration). The new scaled and filtered data was used to investigate the dynamic response of the FEM model of the vibratory screen.

In section 4.1 it was found from the modal analysis that the mass, stiffness and geometry of the FEM model capture the correct physics of the screen. It was thus proposed that the only parameter remaining to adjust for the FEM model to capture the dynamics of the physical screen were the loads applied to the screen.

With the experimental data collected, the next step was to ensure that the FEM model produced the same steady state response as the physical screen. This was investigated by performing a transient analysis on the FEM model. It was found that computational limitations limited the duration of the transient analysis to 0.7s. This was enough time for the FEM model to reach steady state operation. By looking at figures 4-7 and 4-8 the displacement results from positions on the feed side and the discharge side have the same displacements with the lines being perfectly overlaid on each other. This result was expected as the FEM model of the screen is perfectly symmetric.

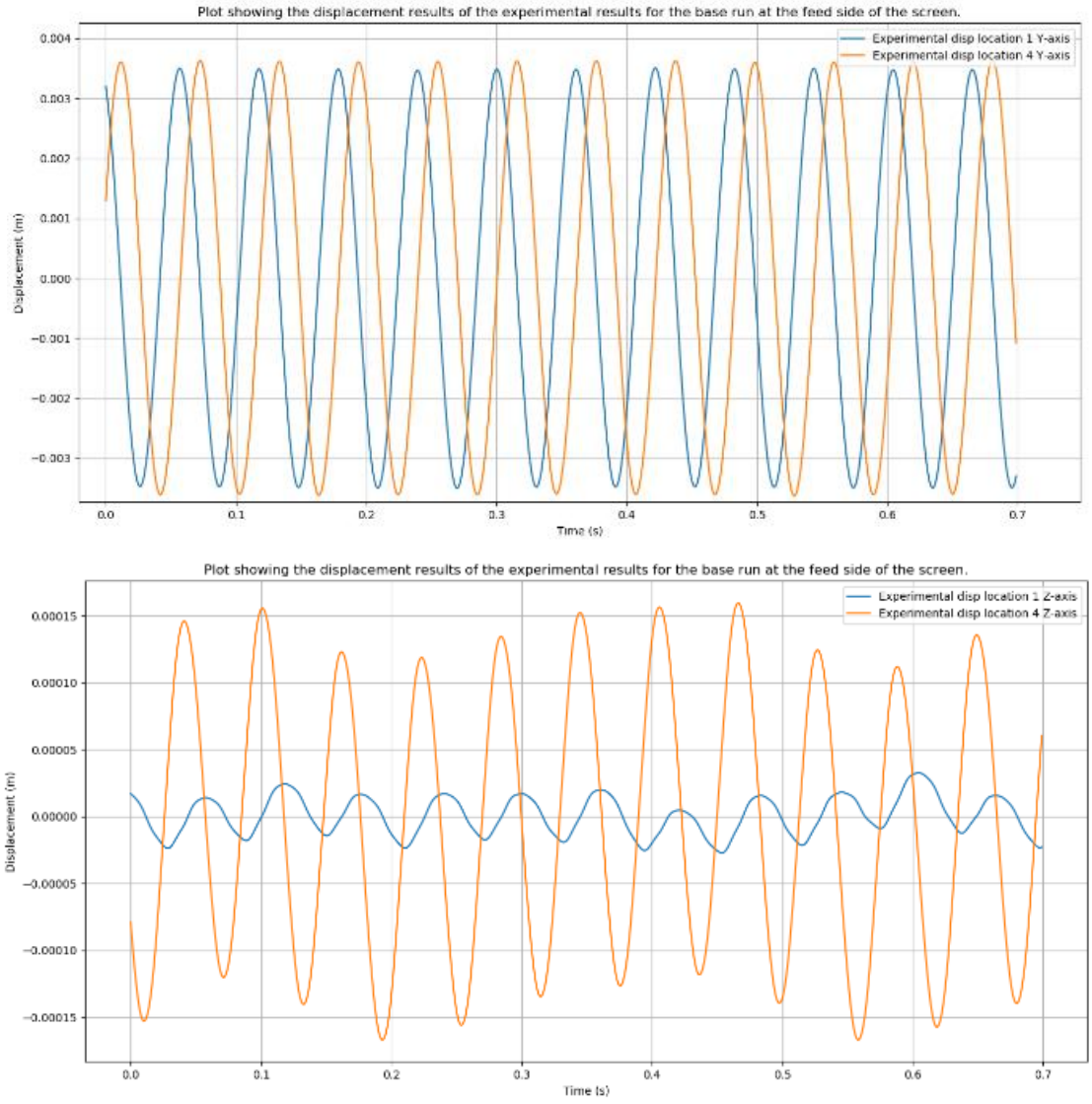

Figure 4-6 Plots showing the main differences in the displacements of the screen.

It is noted that the first portion of the signal in figures 4-7 and 4-8 is transient, with the results only reaching steady state after approximately 0.4s. The remainder of the investigation chapter will deal exclusively with the steady state portion of the signals.

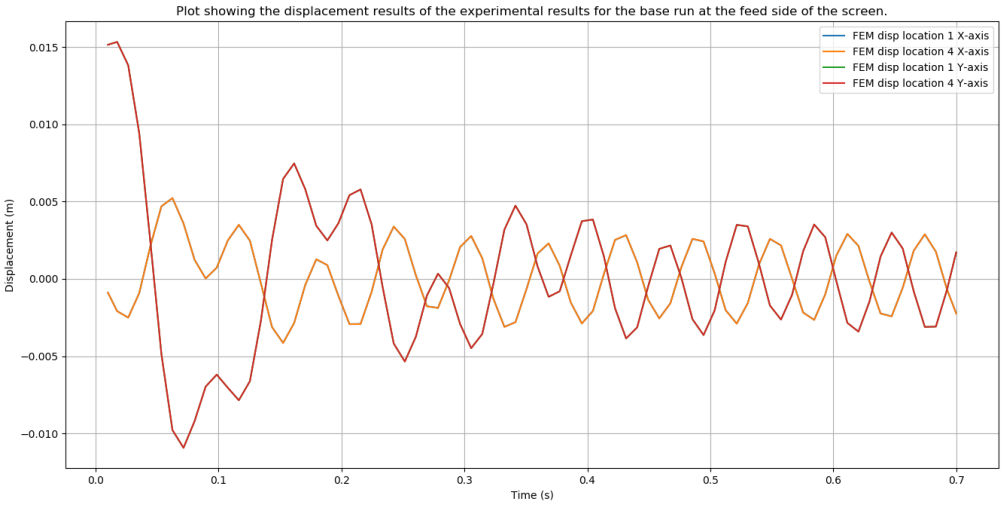

Figure 4-7 FEM results showing the X and Y displacements from the feed side of the screen.

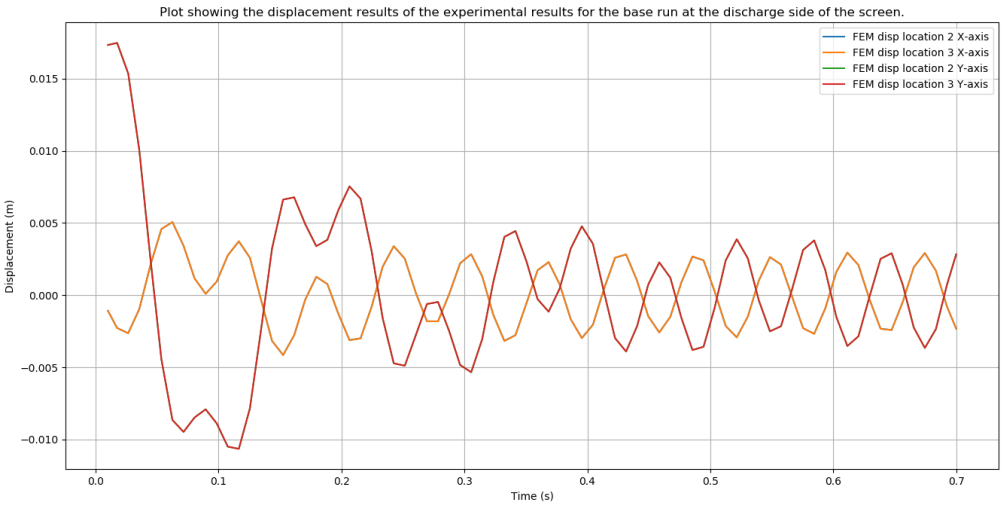

Figure 4-8 FEM results showing the X and Y displacements from the discharge side of the screen.

The next step was to compare the displacement, velocity and acceleration of the base FEM model with the steady state experimental results from the base investigation. It can be seen in figures 4-9 and 4-10 below that the displacement results from the FEM model and the experimental results do not match up. This was rectified by adjusting the excitation force loading conditions so that the displacements were the same. To compensate for the asymmetry in the physical screen, it was decided to modify the loading conditions so that the FEM results were in-between the experimental data for the two buffers on the feed side and the two buffers on the discharge side of the screen.

The results from the FEM model were smaller than that of the experiments. It was thus necessary to modify the forces applied to the FEM model. For this investigation only the displacement values in the

X and Y directions were of interest as there were no forces being applied in the Z direction of the screen.

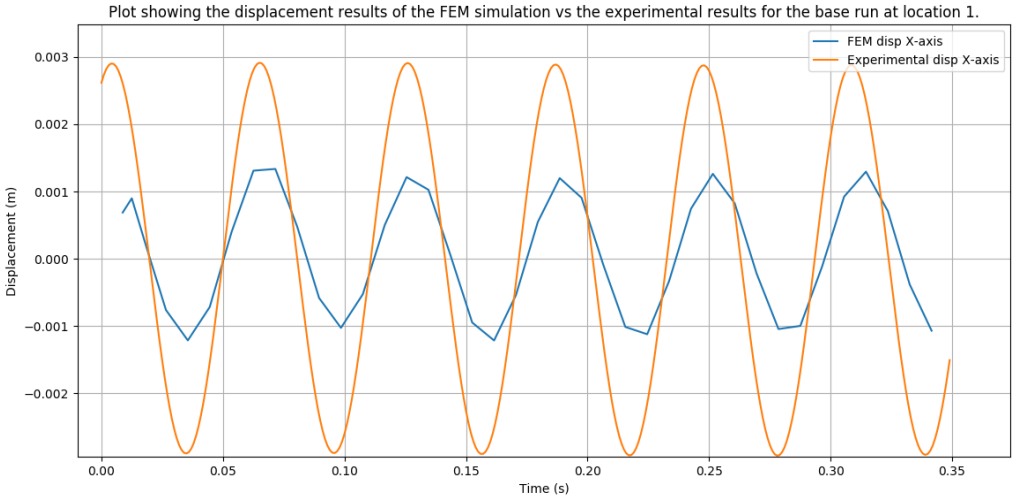

Figure 4-9 Plots showing the base simulation date for the FEM and the experimental displacements in the X direction at rubber buffer location 1.

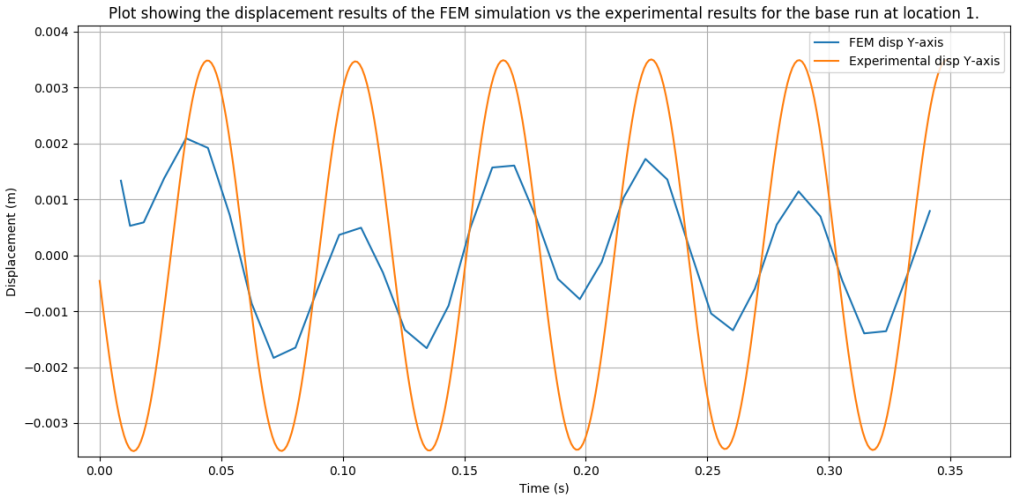

Figure 4-10 Plots showing the base simulation date for the FEM and the experimental displacements in the Y direction at rubber buffer location 1.

The loads on the FEM model were adjusted to ensure that the displacements in the X and Y directions at the 4 corners of the screen were the same as the experimental results. Upon iterating through the process, load magnitudes of 27 000N and 23 640N in the Y and X directions respectively, were found to give the best results. The loads on the screen were not that different to that of the loads calculated in section 2 for the eccentric motors. Figures 4-11 and 4-12 show the comparison between the calibrated FEM base simulation and the experimental base experimental results for rubber buffer location 1. It can be seen in figure 4-11 and 4-12 that the FEM model replicates the dynamic motion

of the physical screen well for the base simulation. It is noted that the calibration of the FEM model at the other 3 rubber buffer locations also line up with the experimental results.

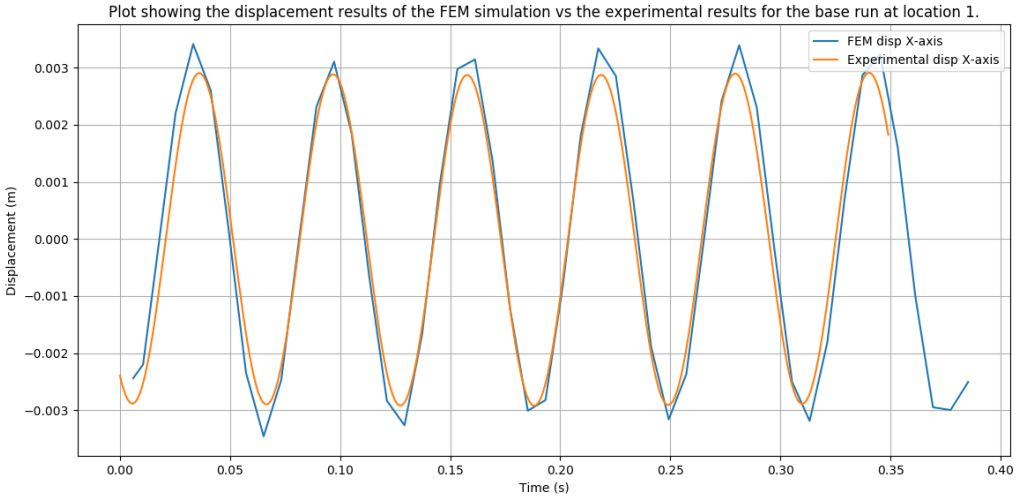

Figure 4-11 Plots showing the calibrated base simulation date for the FEM and the experimental displacements in the X direction at rubber buffer location 1.

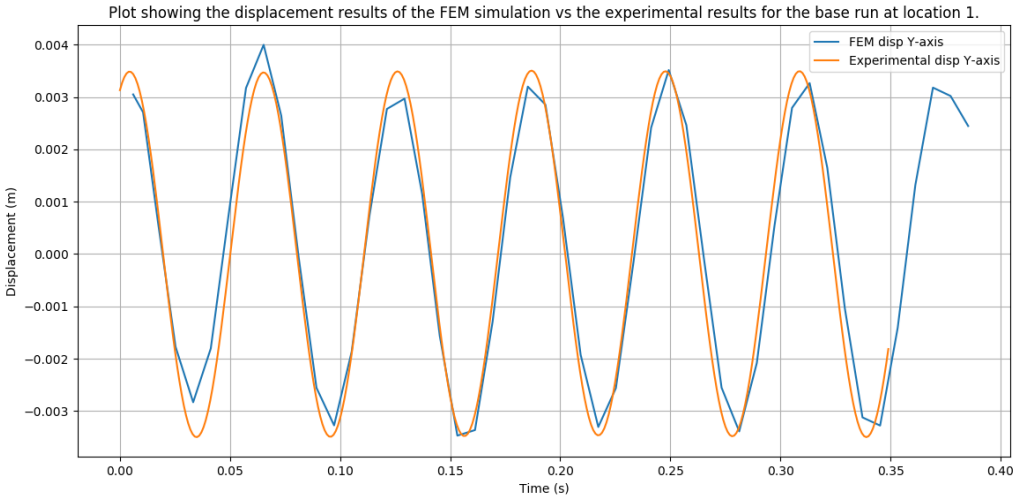

Figure 4-12 Plots showing calibrated the base simulation date for the FEM and the experimental displacements in the Y direction at rubber buffer location 1.

With the response of the dynamic model calibrated, the next step was to investigate the response of the screen under different rubber buffer configurations. The same rubber buffer configurations were investigated as in the experiments.

The next step was to compare the results from the FEM analysis for the different rubber buffer configurations with the experimental results for the same rubber buffer configurations. The aim of this was to investigate if the FEM model can replicate the physics of the screen under different permutations (different stiffness rubber buffer configurations). If the FEM model replicates the results

under the different stiffness rubber buffer configurations it is permissible to say that the FEM model captures the physics of the physical screen.

The displacement results of the FEM and experimental results for 1 less stiff rubber buffer and measurements taken at rubber buffer location 1 in the X and Y directions are plotted in figures 4-13 and 4-14. The results for the remainder of the measurement locations and the different rubber buffer configurations are similar to figure 4-13 and 4-14.

It can also be seen in figure 4-13 and 4-14 as well as in the remainder of the results, that the displacements do somewhat correlate between the FEM model and the experimental results. However, it is not possible to say with confidence that the FEM model was able to replicate the physics of the screen under the different stiffness configurations as the differences in the dynamic response are small. It was proposed to investigate the correlation further in the classification of the screen data, where an intelligent system was trained using the FEM data and the experimental data was then classified using the same intelligent system. This approach would provide more insight into how well the FEM model replicates the physics of the screen.

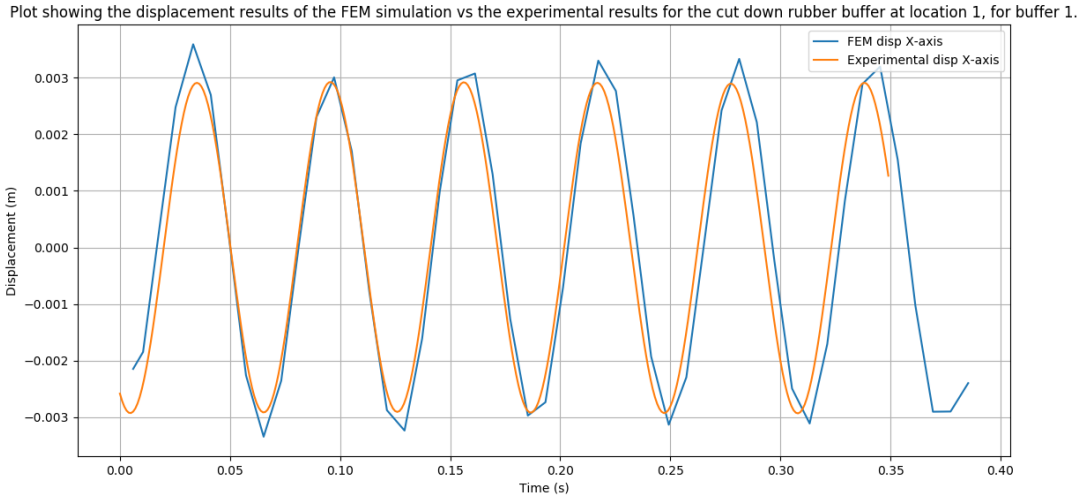

Figure 4-13 Plots showing the 1 cut down rubber buffer simulation date for the FEM and the experimental displacements in the X direction at rubber buffer location 1.

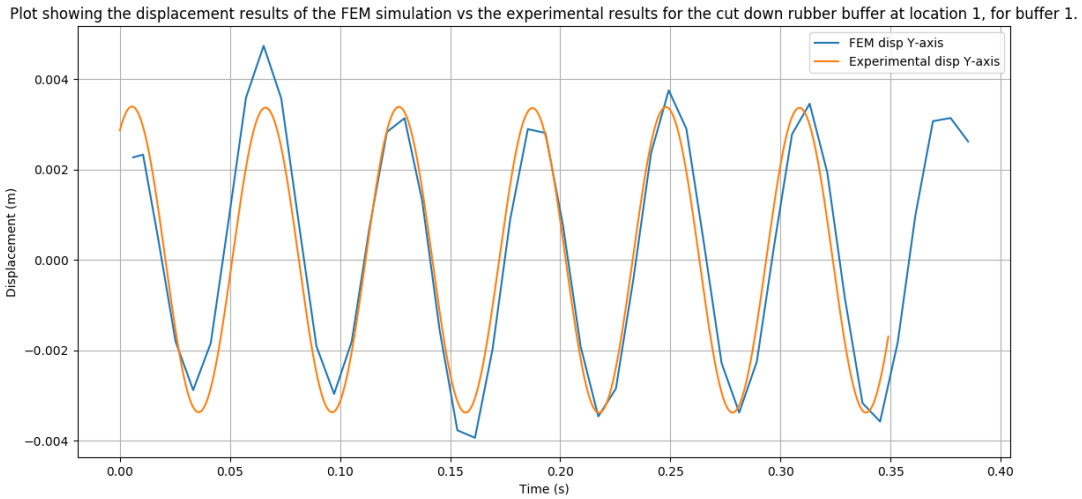

Figure 4-14 Plots showing the 1 cut down rubber buffer simulation date for the FEM and the experimental displacements in the Y direction at rubber buffer location 1.

4.3. Conclusion

In this chapter the mode shapes of the FEM model were compared to that of the physical screen. It was found that the mode shapes of the FEM model and the physical screen correlate well. The resonant frequencies were found to be similar for the FEM model and the experimental modal analysis. The mode shapes were also found to be the same for each of the rigid body modes. This confirmed that the FEM model of the screen was a good representation of the physical screen.

The second part of this chapter involved calibrating the dynamics of the FEM model so that the results were similar to the physical screen for the unmodified base rubber buffer stiffness configuration. The calibration was done by modifying the loads on the screen. The final loads which gave the best dynamic response were similar to the calculated loads. Once the dynamics of the screen were calibrated against the experimental results, the next step was to measure how well the FEM model captured the dynamics of the screen under different stiffness rubber buffer configurations. It was found that the differences in the dynamic responses for the different rubber buffer stiffness configurations were too small to accurately conclude if the FEM model captured the dynamics of the screen.

It was decided that it was impractical to simply plot the FEM results and the experimental results together. It was thus decided to use an intelligent system to help validate the FEM model.

5. Classification of the Screen Data

The aim of the intelligent fault classifier was to investigate if it was possible to detect faults on a vibratory screen. The faults on the screen that were investigated include the different stiffness configurations with different rubbers as well as the investigations with the weights on the screen.

This investigation was conducted as a simple proof of concept with the intent of one day being able to train an intelligent system using faults induced on the FEM model.

Two signal investigations were conducted on the gathered data for the different rubber buffer stiffness configurations, namely, the steady state operation of the screen as well as the run-up and run-down procedures of the screen. These two sets of data were used to train an intelligent system which was able to classify the different rubber buffer stiffness configurations.

The final aspect of the classification of the data was to investigate how well the FEM model replicated the motion of the physical screen under the different rubber buffer stiffness configurations. It was found to be very challenging to draw conclusions by simply looking at the responses of the FEM model and experimental results directly. It was thus decided to process the data from the two signals and extract features from the signals. These features were then compared with each other. Comparing the features provided a significantly simpler methodology of investigating the correlation between the FEM model and the physical screen.

It was also decided to investigate whether it was possible to train an intelligent system using the FEM data and then to classify the experimental data using the same intelligent system. This is a concept which is relevant to industry as it is often not easy to halt screening operations so that experiments can be conducted on the physical screen. It was thus proposed to use a FEM model of a vibratory screen and to induce faults on the screen. The response of the screen was then used to train an intelligent system. The intelligent system would then be employed on the physical screen to classify faults without having to perform experiments on the physical screen.

It is noted that these investigations of the faults are not a real-world scenarios. It is expected that the faults would not happen individually, but the faults would happen in different degrees of severity. For example, in the real world one of the rubber buffers could be at 80% of the desired stiffness and another could be at 50% of the desired stiffness. There would also be material constantly passing over the deck of the screen with varying mass flow rates. This example would be extremely difficult to classify as the factors at play are extremely complicated. The material passing over the surface of the screen not only induces more complexity to the classification, but it also makes the signal very noisy.

In this investigation, only the two cut down rubber buffers were investigated, and the material classification was done using the un-cut rubber buffers. This simplification was made to simplify the classification of the faults as the investigation was primarily interested in the development and validation of the FEM model.

5.1. Investigation of the Run-up and Run-down Data

The first investigation of fault classification was done on the run-up and run-down data from the screen as it was expected to be the simplest method to get good results from. The experimental results measured in section 3.2.1 from the different rubber buffer stiffness configurations as well as the base run make up the 11 individual classes.

The first step was to extract, filter and integrate the data accordingly. The run-up and run-down data was split up into individual classes so that the features could be extracted, and correct labels generated. Once the data was split up it was found that the data sources were still in order with all the base scenarios together. To ensure the validity of the investigation, the training and testing data samples were randomly shuffled. By shuffling the data, it ensured that the intelligent system can classify the test data no matter the order of the faults.

It was important to note that the data for each class was broken up into two distinct sets; training set and testing set. This was important to do as it is not a valid approach to test the method on the same data that it was trained on.

The feature extraction process was critical as this condenses a long-time signal into smaller bits of information which can retain as much of the discerning characteristics of the signal as possible. The features which were investigated for the run-up and run-down were the mean value of the signal, frequency value which corresponds to the largest peak in the FFT, the skewness of the signal, maximum value in the signal, minimal value in the signal, variance, kurtosis and the standard deviation. Each of the features was calculated for the displacement, velocity and acceleration in the X, Y and Z directions.

It was expected that the features would produce different results in different arrangements and configurations. However, for this investigation the classification process was not optimised as it is purely a proof of concept and is not the main interest of the dissertation.

Once the data had been processed, the final step was to train and test the results using an intelligent method. There are many built in intelligent methods in the sklearn package in Python. These packages

were investigated to see which method was best suited to classifying the data. The accuracy of the different methods was assessed based on the test set classification accuracy.

Different sklearn packages were investigated to see which gave the best classification accuracy. The most successful method was the linear Support Vector Machine classifier. This classifier was quick and used minimal computational resources in comparison to that of a neural network.

Initially the classification of the faults was in the 70%-90% range. It was decided to investigate the effect of changing the tolerance of the classifier. It was found that by changing the tolerance of the classifier to 1.1e-02 the classification accuracy became perfect.

Using this classifier, the resulting classification accuracy of the different rubber buffer configurations for the run-up portion of the signal was perfect. The same result was found for the run-down portion of the signal.

The classification of the data was based on the nature of the features and how effective the classifier could distinguish between different features. With a result of perfect classification being achieved with minimal effort, it was necessary to validate the perfect classification result. This was done by plotting the data produced by different features against each other for the different rubber buffer stiffness configurations. The results were expected to show distinct regions which are occupied by the different configurations in feature space, thus verifying the perfect classification.

It is noted that it was a large task to plot each of the features against each of the remaining features. It can be seen from figure 5-1 below that there is a strong distinction between the different features, hence the perfect classification accuracy. This result was found for the other features as well.

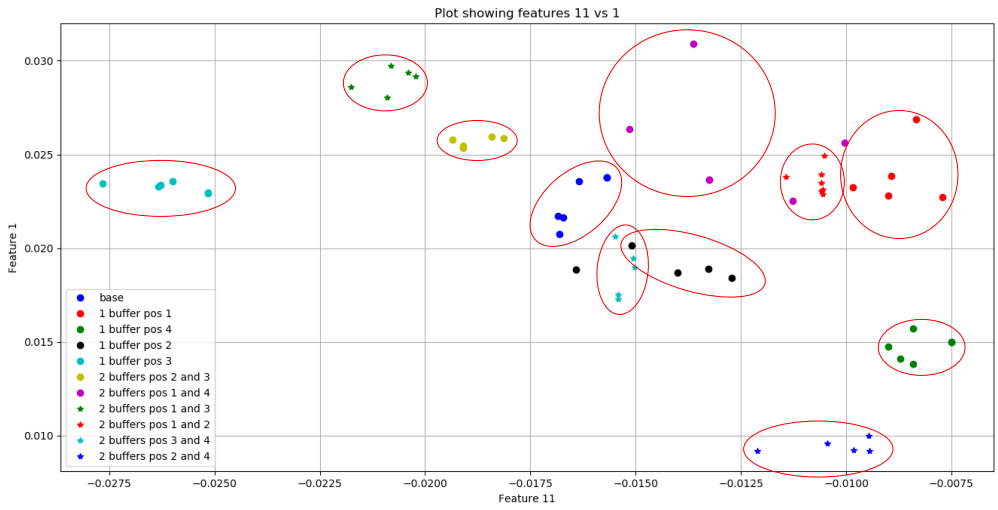

Figure 5-1 Plot showing the comparison between feature 11 and feature 1.

5.2. Investigation of the Steady State Signal

The next step was the classification of the steady state signal. For this classification the same approach was taken as for the classification of the run-up and run-down signals. The only difference was that the steady state signals measured were very long. This allowed the signals to be broken up into sections with each section being treated as an individual bit of information for testing or training. By breaking up the signals, this allowed for large amounts of data to be used to train and to test the results.

Other than splitting the signal, all the parameters and approaches were kept the same as from the run-up and run-down investigation. The same classifier was used initially as it was a good starting point. The initial classification accuracy was 72%. Changing the 'multi_class' parameter to 'ovr' resulted in a classification of 100%.

In the investigation, the most important features were investigated. It was found that there was a strong independence between the features under the different rubber buffer configurations. This proved that there is a measurable and quantifiable difference under the different buffer configurations. It can be seen form the figures 5-2 that there is a strong distinction between the different features, hence the perfect classification accuracy.

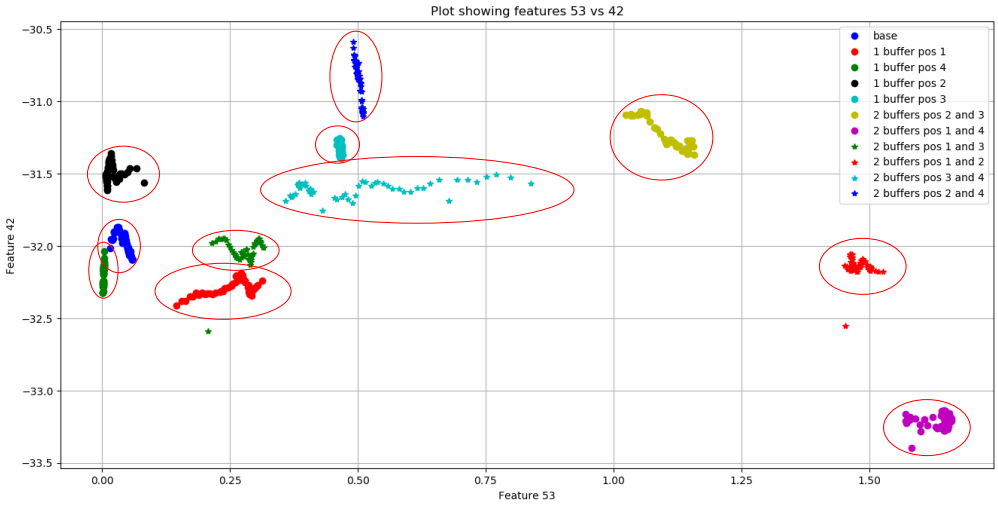

Figure 5-2 Plot showing the comparison between feature 53 and feature 42.

5.3. Investigation of the Steady State Signal with Weights

The next setup was to investigate the classification of the weights on the surface of the screen. This investigation was based on the same premise as the steady state investigation where each signal was

broken up into shorter signals to increase the size of the data set. The classification accuracy was found to be 97%.

This investigation proved to be challenging as there were large amounts of noise introduced by the weights impacting the screen and bouncing in different erratic ways. Another issue that was encountered in the experiments was that the location of the weights on the screen deck was not consistent with time. The weights tended to move small amounts towards the discharge side and then back to the feed side. This behaviour introduced a variable response signal where the location of the plates varies throughout the experiment.

Granted, these inconsistencies in the experimental data act as a more real-life experiment where the loading of the screen is ever changing. With a classification accuracy of 97% achieved, this shows the robustness of the classification even under noisy conditions.

In the figures 5-3 and 5-4 below it can be seen that there was more scattering of the data for each of the different loading classes, where many of the different features overlap. This was different to the results from the run-up, run-down and the steady state operation of the screen where the different rubber buffer stiffness classes had clear distinctions.

Even under the more erratic nature of the features there are still some features which aid in distinguishing between the different classes. Some of these distinguishing features are shown in figures 5-3 and 5-4 below. It is noted that the figures below only represent a small portion of the feature investigated. The linear Support Vector Machine classifier used all the features investigated to create a hyperface in which each of the classes are defined independently from the outer classes.

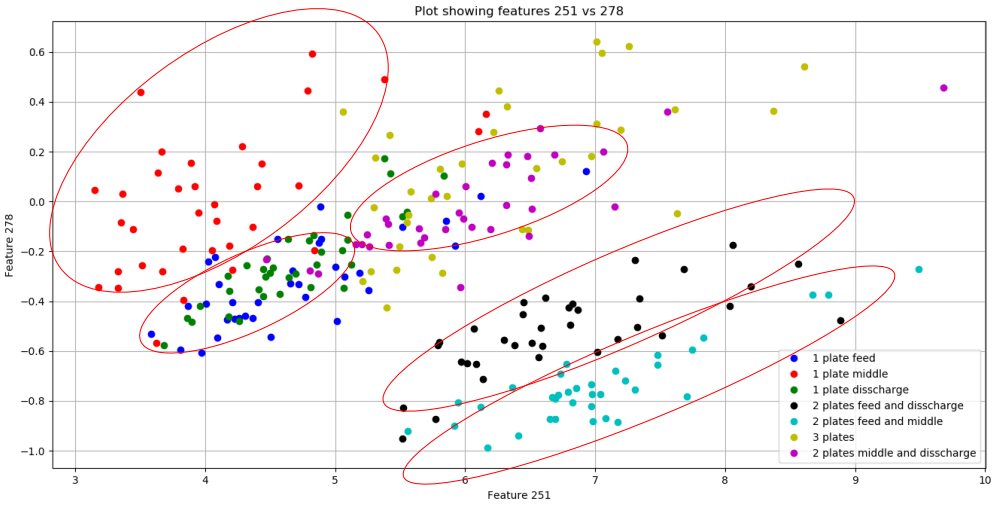

Figure 5-3 Plot showing the comparison between feature 251 and feature 278.

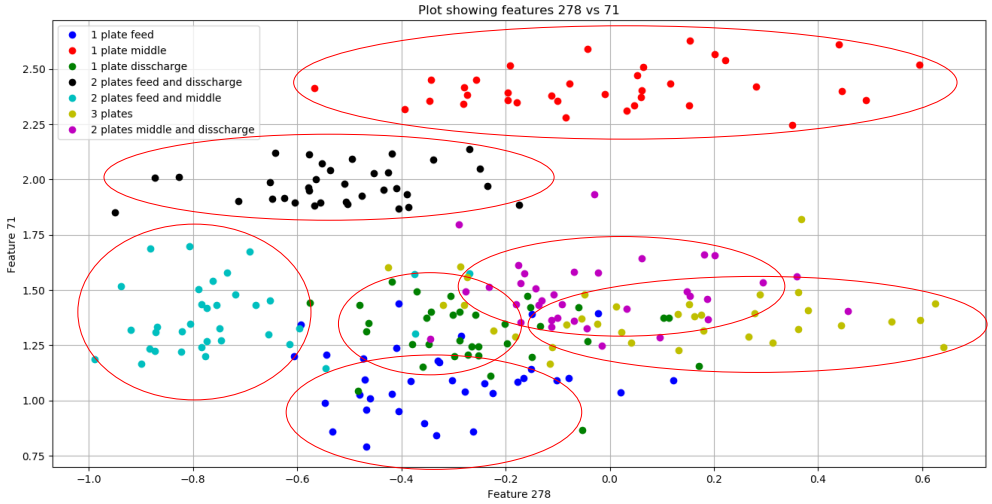

Figure 5-4 Plot showing the comparison between feature 278 and feature 71.

5.4. FEM Classifier

The final test was to investigate whether a classifier trained on the FEM data could be used to classify experimental data. This investigation was not expected to yield the best results as the FEM data was precise about the axis of symmetry and does not contain any external noise. This leads to a discrepancy between the FEM data and the experimental data. Another issue encountered was that the total duration of the steady state portion of the FEM simulation equated to approximately 0.4s of steady state operation, as opposed to 5 minutes of steady state operation for the experimental data.

The solution to balance out the discrepancy between the simulation length of the FEM models and that of the experiments was to increase the length of the FEM simulation. This was done by fitting and optimising a sine wave through the steady state part of the signal. The curve fitting was done with the aid of the curve fit function in scipy. This was done for the displacement data in the X, Y and Z directions. The sine curves were fitted over the last 0.3s of the FEM signal to ensure that the function was fitted to the steady state part of the FEM signal. Once the function was fitted to the signals, the signal could be made as long as needed by simply changing the number of time steps. The results of the curve fitting are shown in figure 5-5. This process was repeated for the remainder of the FEM data with equally good results.

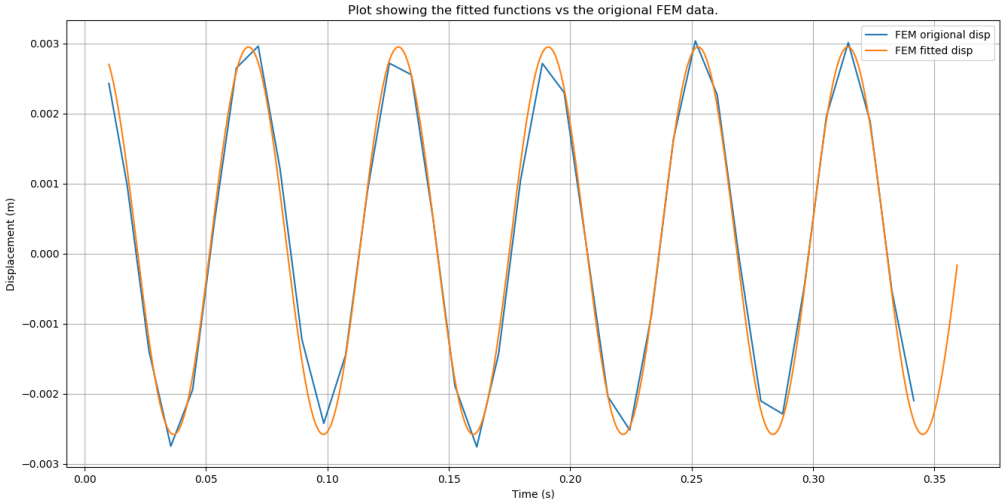

Figure 5-5 Plot showing the curve fitting results for the fem data.

Before the experimental data could be classified using the FEM trained classifier it was first necessary to train a classifier. The same classifier was used as for the steady state investigation. The findings show a 100% classification accuracy. This confirms that the FEM results are independent and unique for each of the different rubber buffer configurations. Figure 5-6 below confirms the perfect classification accuracy as the different classes are all independent with no overlapping. This independence in the features was found for the other features as well.

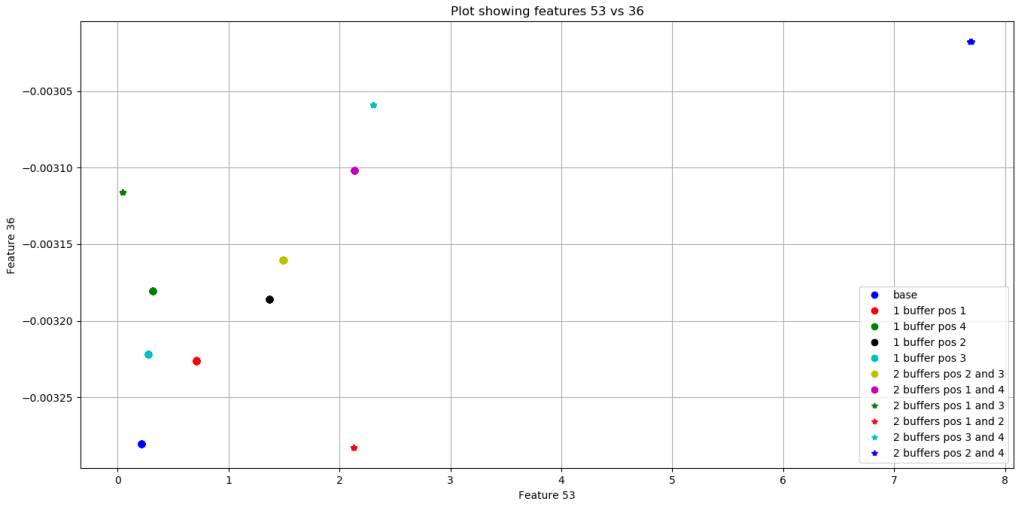

Figure 5-6 Plot showing the comparison between feature 53 and feature 36.

Finally, the experimental data was inserted in-to the trained FEM data classifier. This was not expected to classify well due to the inconsistencies in the dynamics of the physical vibratory screen. The final classification accuracy achieved for the experimental data was 18%. This was due to the classifier classifying all faults with 2 less stiff buffers at positions 1 and 3 correctly as well as all the faults where the less stiff buffers are at locations 2 and 4. The correlation between the features from then FEM model and the experimental results are show in figures 5-7 and 5-8 below. As expected, the results do not correlate.

Possible reasons to explain the poor correlation of results are the response of the screen not being symmetric for the base run. This translates to the remaining experimental results where the stiffness of the rubber buffers was changed. Another reason for the poor correlation of the two sets of data is that the FEM data has no noise in the signal as well as no effects from external sources. This is validated by the tight clusters formed by the different features of the FEM model in the figure 5-7 and 5-8 below.

One aspect that is noted from the below plots of the features was that the shapes of the FEM data and the experimental data produced are similar in nature. A good example of this interaction is figure 5-7 where the shapes produced are almost identical, only the FEM data is shifted down from the experimental data. It can also be seen that the data in the plots is only marginally different and that there are not any order of magnitude differences. This leads to show that the FEM model can somewhat replicate the physics of the vibratory screen. However, it is stipulated that there are large inconsistencies in the dynamics of the physical screen which are not able to be modelled in the FEM model.

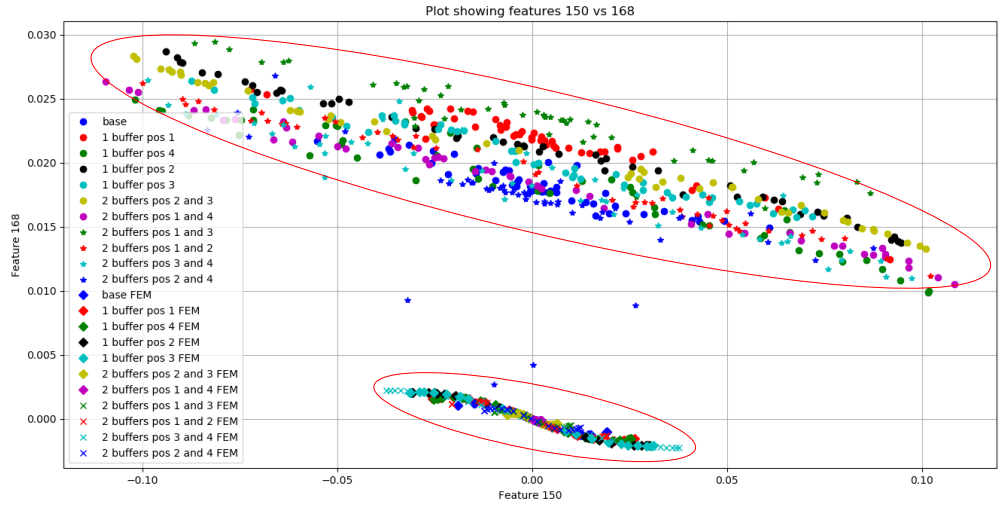

Figure 5-7 Plot showing the comparison between feature 150 and feature 168.

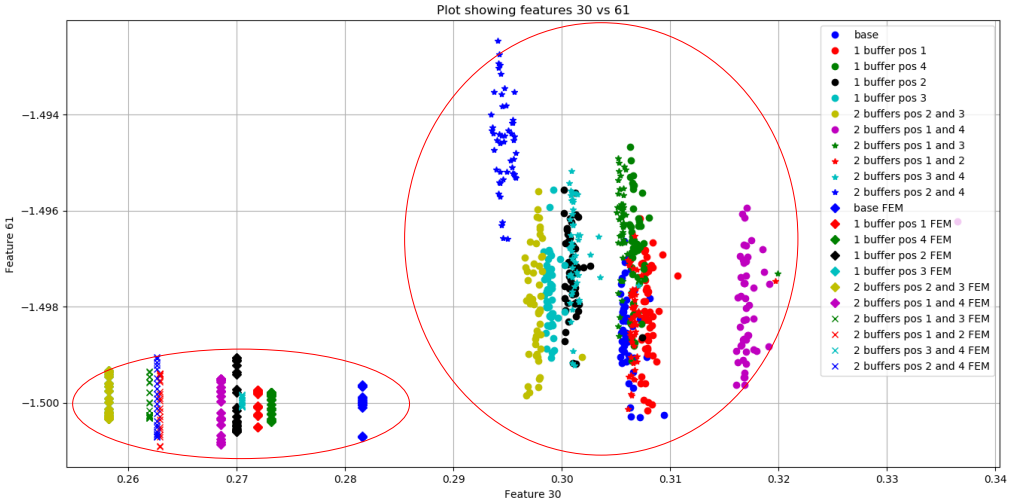

Figure 5-8 Plot showing the comparison between feature 30 and feature 61.

5.5. Conclusion

During the investigation of intelligent methods and their ability to classify faults induced on the screen, it was found that it is possible to classify the faults induced on the screen using the start-up, run-down, steady state and the FEM data. It was also found that it was possible to classify different material configurations on the screen as well.

The best classification method was found to be a non-linear Support Vector Machine as it was able to quantify the independent regions in feature space which are occupied by the different features.

The final part of the investigation of the intelligent methods involved training a system using the FEM data and then classifying the steady state experimental data. This investigation yielded poor results as there was a clear difference in the signals produced by the different signals between the FEM model and the physical screen.

6. Conclusion and Recommendations

6.1. Conclusion of Thesis

In this document a model of a vibratory screen was developed which could replicate the dynamics of a physical screen. The generated model was then calibrated and validated using different means.

The first stage was to characterise the rubber buffers which support the screen. This was done experimentally. It was found that the characterisation of the rubber buffers was an accurate representation of the characteristics of the rubber buffers in the normal and shear directions. The characterisation of the rubber buffers was also done for the two cut down rubber buffers. The stiffness characteristics of the rubber buffers were found to be near linear. Thus, the rubber buffers could be modelled using linear stiffness springs in ANSYS.

The calibration process of the model was broken up into two stages: the first stage was where the modal frequencies from the FEM model and the physical screen were investigated. This was done to see if the physical properties of the screen were the same as the FEM model. It was found that the FEM model and the physical model had similar modal frequencies. This showed that the FEM model was a good physical representation of the screen. it was also found that the mode shapes of the FEM model and physical screen were in the same directions and in the same order. The second stage of the calibration was to calibrate the loading conditions on the FEM model so that the displacements in the X and Y directions were the same. The final loading conditions which led to the same displacements in the X and Y directions were similar to the loads calculated from the physical properties of the eccentric weights. Upon comparing the displacement results from the FEM model under the different rubber buffer stiffness permutations to the results from the physical model under the same rubber buffer stiffness permutations, it was found that it was not possible to concretely determine whether the FEM model captured the dynamics of the screen for the different stiffness configurations.

It was decided to compare the FEM model of the screen with the physical model of the screen by training an intelligent system. The intelligent system was then trained using the FEM results and used to classify the physical screen data.

Before the FEM model could be classified on the system it was first necessary to validate that an intelligent system was capable of discerning and classifying different faults. This was done by training an SVM classifier using the run-up and run-down signals, steady state signals under different loading conditions and the steady state signal under different rubber buffer stiffness configurations. It was found that the intelligent system could classify the different faults and loading conditions well.

The final step was to validate the dynamics of the FEM model by classifying the experimental data using the intelligent system trained using the FEM results under the different rubber buffer stiffness configurations. It was discovered that the classification of the experimental data was not possible using a system trained using FEM data. This was due to large inconsistencies in the response of the physical screen due to the screen not being symmetric and containing manufacturing issues. However, it was shown that both the FEM model and the physical screen contain unique information. This allowed for the perfect classification of the different stiffnesses of the rubber buffers when the intelligent systems were trained and classified using only the FEM data or only the experimental data.

The FEM model of the screen is a good representation of the physical screen. However, due to inconsistencies in the response in the physical screen it was not possible to use the intelligent system trained using the FEM model to classify the same faults on the physical screen.

6.2. Recommendations for Future Work

The following recommendations are made for future work in the modelling of a vibratory screen in a FEM environment as well as the fault detection on a screen:

- In the thesis it was found that it was possible to detect and classify different stiffness rubber buffer configurations. It is proposed that the classification of rubber buffers be expanded by investigating a larger number of different rubber buffers with different stiffnesses. It is also proposed that steel springs be investigated as opposed to the rubber buffers as the steel springs offer a more consistent linear response in comparison to the rubber buffers which will be easier to investigate.
- During the experimental analysis it was discovered that the response of the screen was not symmetric at the feed and at the discharge side. It is suggested that the asymmetric response of the physical screen be captured using the FEM model, thereby making a specific model which is designed for the screen.
- To better investigate the intelligent fault detection, it is suggested that the features be optimised. This will make for the possibility of using such an intelligent method in the field to monitor as well as detect faults on a screen.

References

Andrew, L. (2018). *The Benefits of Nonlinear Pipe Stress Analysis Method*. [online] Bentley Communities. Available at: https://communities.bentley.com/products/pipe_stress_analysis/b/pipe_stress_analysis_blog/posts/the-benefits-of-nonlinear-pipe-stress-analysis-method [Accessed 9 Jul. 2018].

Bian, J. and Jing, X. (2017) 'Nonlinear passive damping of the X-shaped structure', *Procedia Engineering*. Elsevier B.V., 199, pp. 1701–1706. doi: 10.1016/j.proeng.2017.09.372.

Blekhman, I. I. and Sorokin, V. S. (2010) 'On the separation of fast and slow motions in mechanical systems with high-frequency modulation of the dissipation coefficient', *Journal of Sound and Vibration*. doi: 10.1016/j.jsv.2010.06.008.

Champion, R. and Champion, W. L. (2011) 'Departure from linear mechanical behaviour of a helical spring', *Mathematical and Computer Modelling*. Elsevier Ltd, 53(5–6), pp. 915–926. doi: 10.1016/j.mcm.2010.10.028.

Chang, C. C., Chang, T. Y. P., Xu, Y. G. & To, W. M. (2002) 'Selection of training samples for model updating using neural networks', *Journal of Sound and <ibration*, 249(5), pp. 867–883. doi: 10.1006.

Cronjé, J. M. *et al.* (2005) 'Development of a variable stiffness and damping tunable vibration isolator', *JVC/Journal of Vibration and Control*, 11(3), pp. 381–396. doi: 10.1177/1077546305048585.

Faiz, J., Ebrahimi, B. M., Akin, B. & Toliyat, H. A. (2009) 'Comprehensive eccentricity fault diagnosis in induction motors using finite element method', *IEEE Transactions on Magnetics*. doi: 10.1109/TMAG.2009.2012812.

Fuller, K. N. G., Gough, J. and Ahmadi, H. R. (1999) 'Predicting the Response of High Damping Rubber Bearings using simplified models and Finite Element Analysis'.

Gan, M., Wang, C. and Zhu, C. (2015) 'Multiple-domain manifold for feature extraction in machinery fault diagnosis', *Measurement: Journal of the International Measurement Confederation*. doi: 10.1016/j.measurement.2015.07.042.

Gómez, S. S. and Metrekine, A. (2017) 'Evaluation of the applicability of an energy method to calculate the damping in a lab-scale structure', *Procedia Engineering*. Elsevier B.V., 199, pp. 459–464. doi: 10.1016/j.proeng.2017.09.018.

Guo, N., Guo, S. and Luo, L. (2010) 'Modal characteristics and finite element analysis of screen box for ultra-heavy vibrating screen', in *ICIC 2010 - 3rd International Conference on Information and Computing*. doi: 10.1109/ICIC.2010.343.

Guo, N., Lin, J. and Huang, W. (2011) 'Development of 2YAC2460 super-heavy vibrating screen', in *2011 2nd International Conference on Mechanic Automation and Control Engineering, MACE 2011 - Proceedings*. doi: 10.1109/MACE.2011.5987160.

Guyon, I. and Elisseeff, A. (2006) 'Feature Extraction, Foundations and Applications: An introduction to feature extraction', *Studies in Fuzziness and Soft Computing*, 207, pp. 1–25. doi: 10.1007/978-3-540-35488-8_1.

He, W. F. and Xian, A. M. (2013) 'Statics and Modal Analysis for Large Vibrating Screen', *Applied Mechanics and Materials*, 380–384, pp. 136–139. doi: 10.4028/www.scientific.net/AMM.380-384.136.

HE, X. and LIU, C. (2009) 'Dynamics and screening characteristics of a vibrating screen with variable elliptical trace', *Mining Science and Technology*. doi: 10.1016/S1674-5264(09)60095-8.

'Intelligent maintenance solutions vibration analysis of vibrating screens' (2012).

Jiang, Q., Jia, M., Hu, J. & Xu, F. (2009) 'Machinery fault diagnosis using supervised manifold learning', *Mechanical Systems and Signal Processing*. doi: 10.1016/j.ymssp.2009.02.006.

K. Frolov and Goncharevich, I. (1992) '1992 Vibration Technology Theory and Practice', *Advances in science and technology in the USSR*.

Kan, M. S., Tan, A. C. C. and Mathew, J. (2015) 'A review on prognostic techniques for non-stationary and non-linear rotating systems', *Mechanical Systems and Signal Processing*. doi: 10.1016/j.ymssp.2015.02.016.

Kumar, A. and Kumar, R. (2017) 'Time-frequency analysis and support vector machine in automatic detection of defect from vibration signal of centrifugal pump', *Measurement*. doi: 10.1016/j.measurement.2017.04.041.

Lakhlani, B. and Yadav, H. (2017) 'Development and Analysis of an Experimental Setup of Spring - Mass - Damper System', *Procedia Engineering*, 173, pp. 1808–1815. doi: 10.1016/j.proeng.2016.12.223.

Lee, J. *et al.* (2014) 'Prognostics and health management design for rotary machinery systems -

Reviews, methodology and applications', *Mechanical Systems and Signal Processing*. doi: 10.1016/j.ymssp.2013.06.004.

Liu, C., Peng, L. and Li, F. (2011) 'Survey of signal processing methods and research on vibrating screen fault diagnosis', in *2011 2nd International Conference on Mechanic Automation and Control Engineering, MACE 2011 - Proceedings*. doi: 10.1109/MACE.2011.5987286.

Luo, R. K. (2017) 'Determination of rubber material properties for finite element analysis from actual products.'

Luo, R. K. and Wu, W. X. (2006) 'Fatigue failure analysis of anti-vibration rubber spring', *Engineering Failure Analysis*. doi: 10.1016/j.engfailanal.2004.10.012.

Luo, R. K., Wu, W. X. and Mortel, W. J. (2000) 'Effect of loading environment on rubber bolster springs used in railway vehicle bogies', *Plastics, Rubber and Composites Processing and Applications*, 29(2). doi: 10.1179/146580100101540824.

Mcmillan, G. J. & Papadopoulos, J. and Papadopoulos, P. E. (2011) 'Analysis of Vibratory Equipment Using the Finite Element Method'.

Mevada, H. and Patel, D. (2016) 'Experimental Determination of Structural Damping of Different Materials', *Procedia Engineering*, 144, pp. 110–115. doi: 10.1016/j.proeng.2016.05.013.

Milašinović, D. D. (2007) 'Rheological-dynamical analogy: Prediction of damping parameters of hysteresis damper', *International Journal of Solids and Structures*, 44(22–23), pp. 7143–7166. doi: 10.1016/j.ijsolstr.2007.04.001.

Mogensen 'Instruction Manual for Vibratory Plant', 44(0), pp. 1–26.

Du Plooy, N. F. and Heyns, P. S. (2001) 'using a vibration absorber to reduce vibratory screen structural loading', *Structural Engineering, Mechanics and Computation*, 2, pp. 1313–1317.

Ramatsetse, B., Mpofu, K. and Makinde, O. (2017) 'Failure and sensitivity analysis of a reconfigurable vibrating screen using finite element analysis', *Case Studies in Engineering Failure Analysis*. doi: 10.1016/j.csefa.2017.04.001.

Rodriguez, C. G. *et al.* (2016) 'Nonlinear model of vibrating screen to determine permissible spring deterioration for proper separation', *Shock and Vibration*. doi: 10.1155/2016/4028583.

Ronghua, S., Liuqing, Z. and Chenyu, P. (2011) 'CAE applied to dynamic optimal design for large-scale vibrating screen', in *Proceedings - 2010 1st ACIS International Symposium on Cryptography, and Network Security, Data Mining and Knowledge Discovery, E-Commerce and Its Applications, and Embedded Systems, CDEE 2010*. doi: 10.1109/CDEE.2010.67.

Wang, J. *et al.* (2016) 'A multi-scale convolution neural network for featureless fault diagnosis', in *International Symposium on Flexible Automation, ISFA 2016*. doi: 10.1109/ISFA.2016.7790137.

WANG, W. J. *et al.* (2001) 'the application of some non-linear methods in rotating machinery fault diagnosis', *Mechanical Systems and Signal Processing*. doi: 10.1006/mssp.2000.1316.

Xiao, S. *et al.* (2016) 'Bayesian Networks-based Association Rules and Knowledge Reuse in Maintenance Decision-Making of Industrial Product-Service Systems', in *Procedia CIRP*. doi: 10.1016/j.procir.2016.03.046.

Xiong, X., Yang, S. and Gan, C. (2012) 'A new procedure for extracting fault feature of multi-frequency signal from rotating machinery', *Mechanical Systems and Signal Processing*. doi: 10.1016/j.ymssp.2012.06.015.

Xue, G., Zhao, G. and Wu, S. (2011) 'Transfer function law and diagnosis method of large vibrating screen lower beam with crack flaw', in *Proceedings - 3rd International Conference on Measuring Technology and Mechatronics Automation, ICMTMA 2011*. doi: 10.1109/ICMTMA.2011.831.

Yuan, Y. and Liu, H. (2014) 'An iterative updating method for damped structural systems using symmetric eigenstructure assignment', *Journal of Computational and Applied Mathematics*. Elsevier B.V., 256, pp. 268–277. doi: 10.1016/j.cam.2013.07.047.

Yue-Min, Z. *et al.* (2009) 'Dynamic design theory and application of large vibrating screen', *PROEPS*, 1, pp. 776–784. doi: 10.1016/j.pro.

Appendices

A. Full Characterisation of the Rubber Buffers

To ensure the completeness of the characterisation the Young's modulus and shear modulus were calculated. Young's modulus and shear modulus were calculated by dividing the stress with the strain. The stresses and strains of the rubber buffer were calculated using the experimental data shown in figure A-1 and A-2 and equations A.1 and A.2 were used. The Young's modulus was then calculated using equation 2.11. The maximum and minimum values were used in the calculation to ensure that the answer was an average over the whole domain. The shear stresses and shear strains of the rubber buffer were calculated using equations 2.9 and 2.10. The shear modulus was then calculated using equation A.6 the maximum and minimum values were used in the calculation to ensure that the answer was an average over the whole domain. The Young's modulus was 3.05MPa and the shear modulus is 2.2MPa. It is noted that the shear modulus was lower than the Young's modulus this was expected as the stiffness in the normal direction was larger than the stiffness in the shear direction. The stress vs strain curve is shown in figure A-3 and the shear stress vs shear strain curve is shown in figure A-4. It is noted that the shapes of the curves are similar to the curves of the normal force vs displacement and the shear force vs displacement.

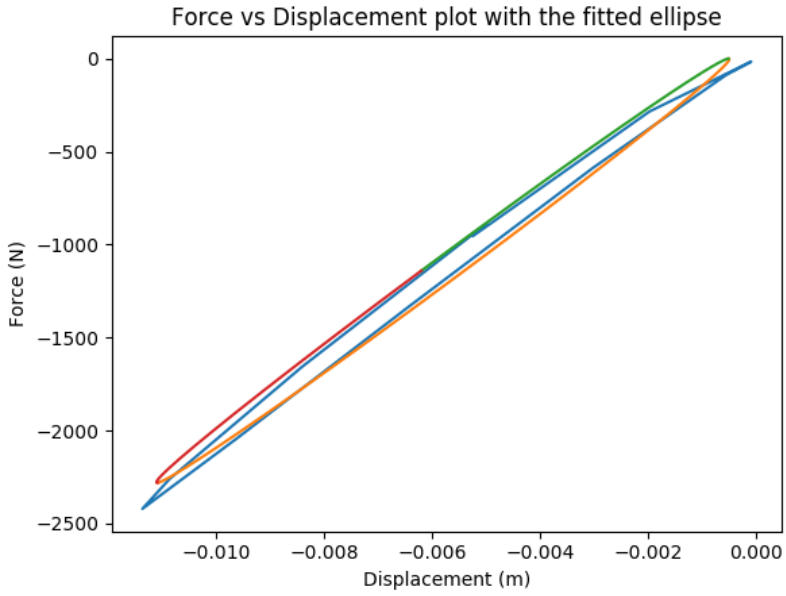

Figure 6 A-1 Plot showing the force-displacement data in the normal direction with an ellipse superimposed over the data.

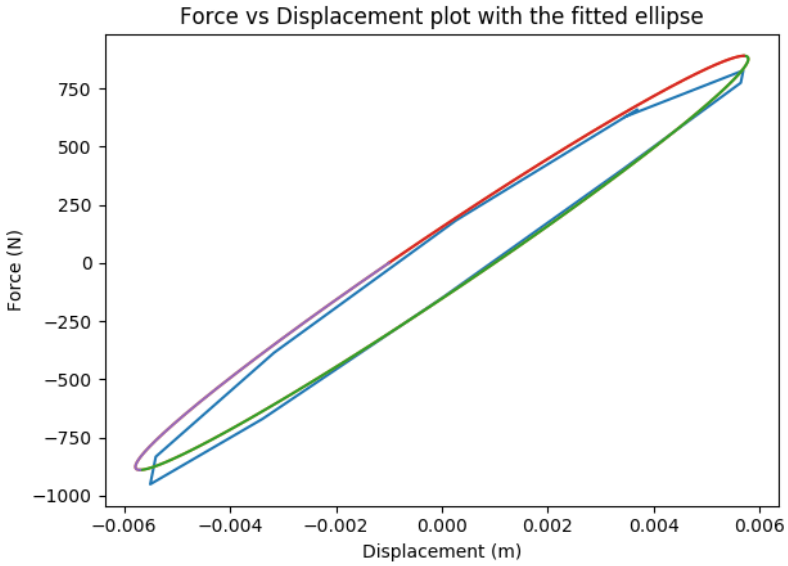

Figure 6 A-2 Plot showing the force-displacement data in the normal direction with an ellipse superimposed over the data.

$$\sigma = \frac{F}{A} \tag{A.1}$$

$$\epsilon = \frac{\Delta l}{l} \tag{A.2}$$

$$\tau = \frac{F}{A} \tag{A.3}$$

$$\gamma = \frac{\Delta x}{l} \tag{A.4}$$

$$E = \frac{\Delta \sigma}{\Delta \epsilon} \tag{A.5}$$

$$G = \frac{\Delta \tau}{\Delta \gamma} \tag{A.6}$$

$$E = \frac{0 - (-258275)}{0 - (-0.08469)} = 3\,050\,000\ Pa = 3.05\ MPa$$

$$G = \frac{95300 - (-91417)}{0.04222 - (-0.0424)} = 2\,940\,571\ Pa = 2.207\ MPa$$

With the characterisation of the rubber buffer in the shear and normal directions complete, the results could be inserted into the FEM and numerical model to validate the generated results. The physical properties of the rubber buffer are shown in table 8, these properties were used to simulate and validate the rubber buffer.

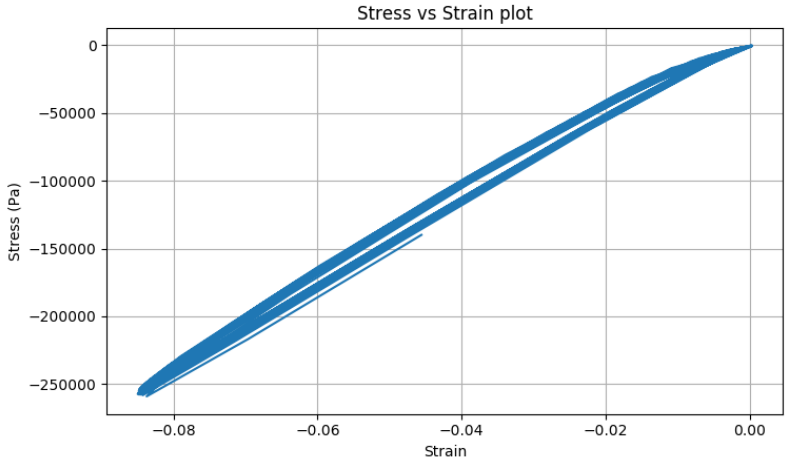

Figure 6 A-3 Plot showing the-stress strain data for the rubber buffer in the normal direction.

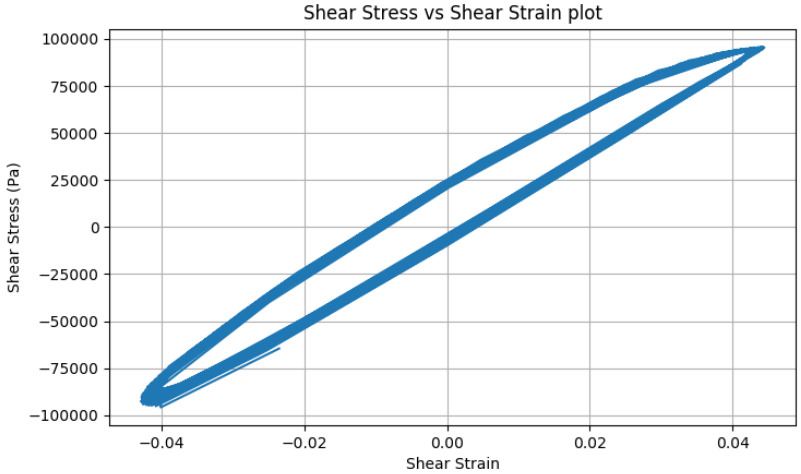

Figure 6 A-4 Plot showing the-stress strain data for the rubber buffer in the shear direction.

Table 8 Material properties of the rubber buffer.

Property	**Value**
Mass (kg)	1.377
Density (kg/m^3)	1106
Length (m)	0.135
Internal diameter (m)	0.052
External diameter (m)	0.121
Surface area of top face (m^2)	0.0093752
Volume (m^3)	0.001265
Stiffness in normal direction (N/m)	210 000
Stiffness in shear direction (N/m)	151 000
Damping in normal direction (Ns/m)	2081
Damping in shear direction (Ns/m)	4252
Poisson's ratio	0.4999
Young's modulus (MPa)	3.05
Shear modulus (MPa)	2.207

The stiffness of the rubber buffer was modelled using a Mooney-Rivlin material model in a FEM model. The investigation of the FEM model was done in both the normal and shear directions. The same loading conditions were used as in the experiments done on the rubber buffer.

Design of the FEM Model

There were several steps which needed to be followed to ensure that an accurate FEM model was constructed. The steps were: the design of the geometry, material properties, meshing, boundary conditions, loads, simulation parameters and results.

The design of the geometry was done in ANSYS using SpaceClaim. The model of the rubber buffer was drawn to the same size as the physical rubber buffer in accordance with the values in table 8. The model of the rubber buffer is shown in figure A-5.

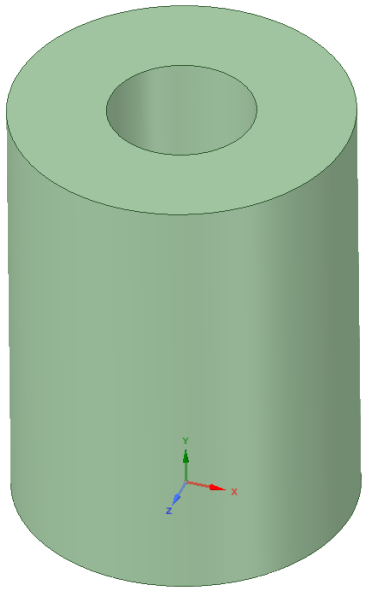

Figure 6 A-5 CAD drawing of the rubber buffer which was simulated in ANSYS.

Next the engineering data values were inserted into the model. The engineering data values used were the density, damping coefficient and the Mooney-Rivlin material coefficients. Equation A.7 shows the general equation for polynomial rubber elasticity potential, equation A.8 is the second order expansion of the general equation, equation A.8 is more commonly known as a two-point Mooney-Rivlin material model. The Mooney-Rivlin material model coeffects were calculate using the built-in calculator in ANSYS. Due to the linear nature of the stress-strain curve a 2 parameter Mooney-Rivlin hyperelastic material model was used.

$$\boldsymbol{W} = \sum_{i+j=1}^{N} C_{ij}(\boldsymbol{I}_1 - 3)^i(\boldsymbol{I}_2 - 3)^j + \sum_{i=1}^{N} \frac{K_i}{2}(j-1)^2 \quad \text{(A.7)}$$

$$W = C_1(\boldsymbol{I}_1 - 3) + C_2(\boldsymbol{I}_2 - 3) \quad \text{(A.8)}$$

The table method required 3 sets of inputs, namely; uniaxial, biaxial and shear test data. The uniaxial and shear test data were known and had been calculated in the sections above. The biaxial was not measured and was an unknown. The procedure of measuring the biaxial data was to apply tensile or compressive loads in two perpendicular directions to the rubber buffer. This was a very difficult task given the circular shape of the rubber buffer. It was decided to calculate the 2 Mooney-Rivlin parameters by trial and error.

The meshing procedure for the rubber buffer was simple. A Hex dominant method was used with face meshing. The face meshing was done by selecting all four surfaces of the rubber buffer. The complete meshed rubber buffer is shown in figure A-6, it is noted that the mesh used was coarse. The coarse mesh could be used due to the simplicity of the geometry and loading conditions. The coarse mesh also allowed for faster solving times.

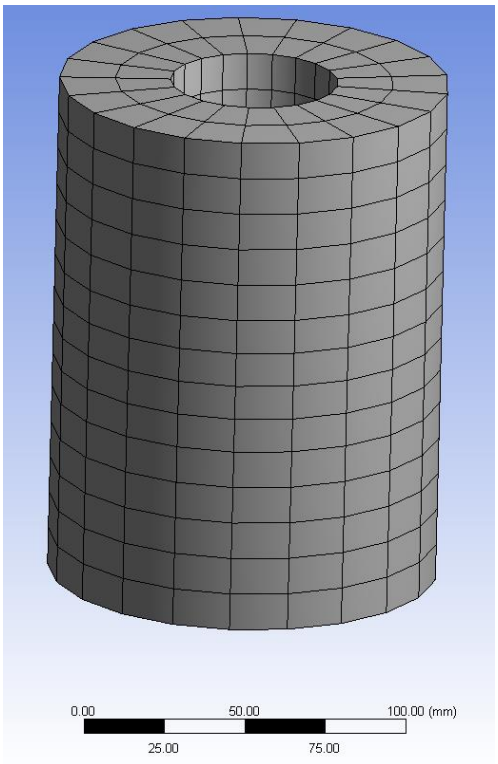

Figure 6 A-6 Meshed rubber buffer.

The next step was to add the loading and boundary conditions. There was only a single boundary condition which was to fix the base of the rubber buffer to the ground. This was done by creating a fixed support on one of the round surfaces. The loading conditions were added in terms of a pressure

applied to the other round face opposite the fixed face. The pressure applied was determined by the magnitude of the force applied in the experiments. The applied pressure was a function of time. The pressure values were equivalent to the normal and shear stresses in figure A-3 and A-4 above. The loads were applied using a sinusoidal function with a frequency of 1Hz. The pressure functions used for the normal and shear excitation are shown in equation A.9 and A.10. It is noted that the normal pressure value is negative, this was due to the force acting in a compressive manor thus the pressure acts towards the surface of the rubber buffer. The duration of the time frame was selected to be 10s as this allowed for the system to complete 5 loading and unloading cycles.

The shear model required a second boundary condition to ensure that the surface to which the load was applied remained on its original plane. This was done to ensure that the FEM model replicated the experiments precisely. This boundary condition was achieved using a displacement support and setting the X and Z degrees of freedom to free and the Y degree of freedom to a fixed displacement.

$$P_{normal} = -125085 \cdot \sin(2 \cdot \pi \cdot t) + \frac{125085}{2}\ Pa \quad \text{(A.9)}$$

$$P_{shear} = 93359 \cdot \sin(2 \cdot \pi \cdot t) + 3883\ Pa \quad \text{(A.10)}$$

The problem was solved using auto time stepping so that the solution could be found as fast as possible while negating computation time loss on poor results. The problem was simulated, and the total deformation of the rubber buffer was measured. The results of the investigation are shown in figure A-7 and A-8 with the experimental results superimposed. The Mooney-Rilvin material coefficients for the normal and shear investigation are shown in table 9. The FEM model can replicate the damping and the stiffness properties of the rubber buffer well. It is noted that figure A-7 and A-8 have discrepancies in their structures to the experimental data, these discrepancies are due to different starting points of the force and displacement conditions of the FEM model.

Table 9 Mooney-Rivlin material constants in the normal and shear directions.

Material constant	**C_{10}**	**C_{01}**	**D1**
Normal direction	6.414E5	0	6E-8
Shear direction	6.414E5	1.9414E6	6E-8

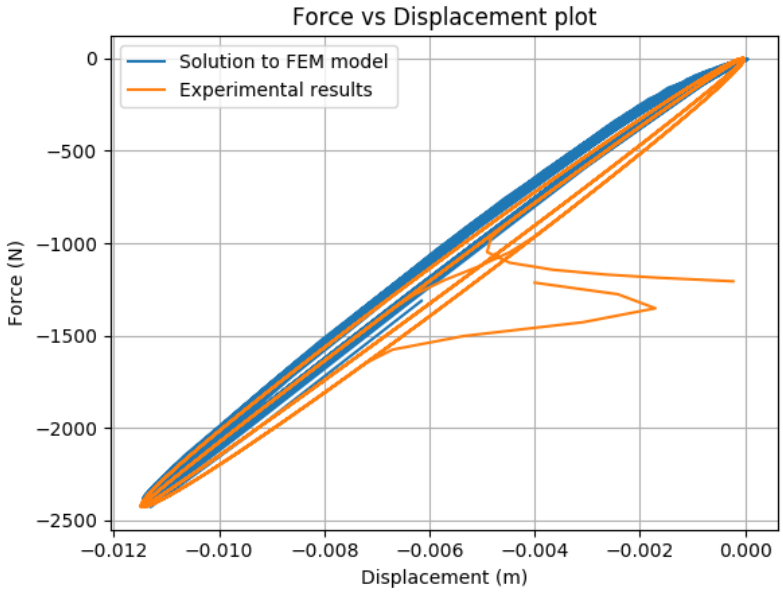

Figure 6 A-7 Plot showing the Mooney-Rivlin material model results superimposed over the experimental results in the normal direction.

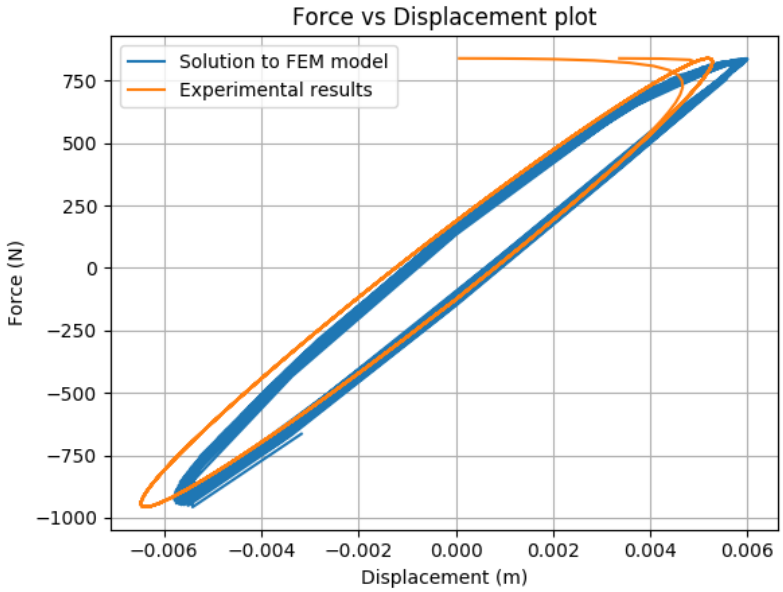

Figure 6 A-8 Plot showing the Mooney-Rivlin material model results superimposed over the experimental results in the shear direction.

Development of the Analytical Model

The solving of the analytical model was an important aspect in the validation of the measured rubber buffer characteristics. Equation A.11 was solved using the built in Ordinary Differential Equation (ODE) solver in Python. The force parameter in equation A.11 was varied in accordance with the loading in

the experiments on the rubber buffer. The mass, stiffness and damping inputs into the equation were the calculated values from table 1.

Before the response could be solved it was necessary to break up equation A.11 which is a second order ODE into two first order ODE. This process is shown in equations A.12 to A.18. The two new single ODEs shown in equations A.19 and A.20 were solved for the initial conditions shown in equations A.21 and A.22.

$$m\ddot{x}(t) + c\dot{x}(t) + kx(t) = f(t) \quad \text{(A.11)}$$
$$x(0) = 0 \quad \text{(A.12)}$$
$$\dot{x}(0) = 0 \quad \text{(A.13)}$$
$$\ddot{x}(t) = -\frac{c}{m}\dot{x}(t) - \frac{k}{m}x(t) + \frac{f(t)}{m} \quad \text{(A.14)}$$
$$let\ u(t) = x(t) \quad \text{(A.15)}$$
$$let\ v(t) = \dot{x}(t) \quad \text{(A.16)}$$
$$\dot{u} = \dot{x}(t) \quad \text{(A.17)}$$
$$\dot{v}(t) = \ddot{x}(t) \quad \text{(A.18)}$$
$$\dot{u}(t) = v(t) \quad \text{(A.19)}$$
$$\dot{v}(t) = -\frac{c}{m}v(t) - \frac{k}{m}u(t) + \frac{f(t)}{m} \quad \text{(A.20)}$$
$$u(0) = 0 \quad \text{(A.21)}$$
$$v(0) = 0 \quad \text{(A.22)}$$

The equations derived above were solved for the variable force in both the normal and shear directions. The results of the solution are plotted against the experimentally measured response, this is shown in figure A-9 and A-10. The analytical model can replicate the response of the rubber buffer well by reproducing the response caused by both the stiffness and the damping of the rubber buffer. It is also noted that the linear force-displacement approximation is valid for both the normal and shear directions. The damping values which were calculated were also a good representation of the damping in the physical rubber buffer.

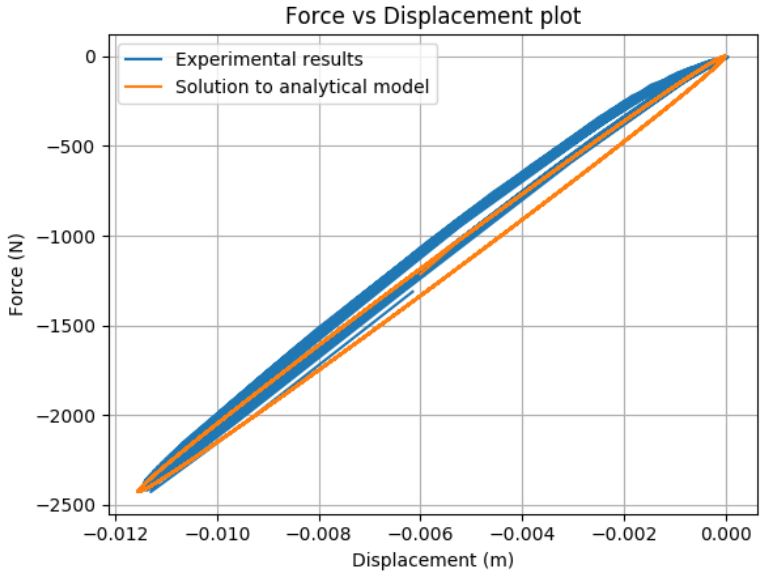

Figure 6 A-9 Plot showing the force-displacement data of the experimental and analytical model in the normal direction.

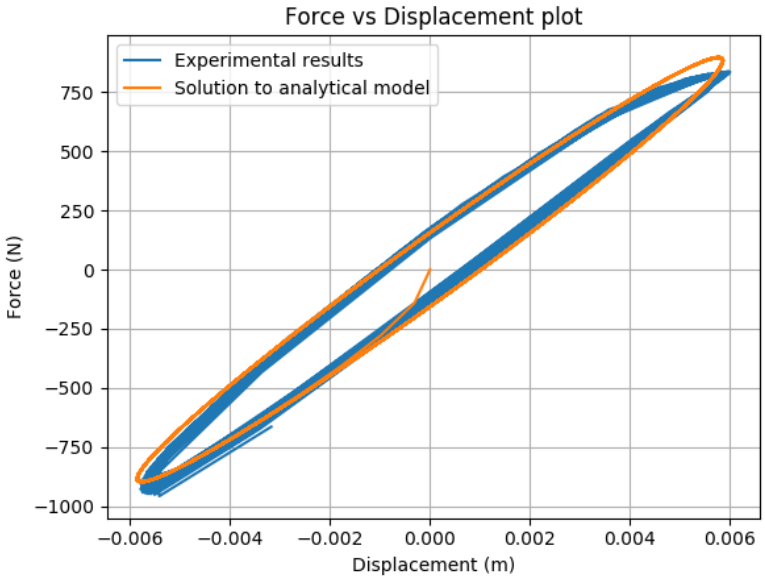

Figure 6 A-10 Plot showing the force-displacement data of the experimental and analytical model in the shear direction.

Conclusion

The characterisation of the rubber buffer was successful as the stiffness and damping properties of the rubber buffer were successfully measured. The results of the characterisation of the rubber buffer were then validated using a numerical and FEM model of the rubber buffer. The validation of the rubber buffer was done using the calculated characteristics of the rubber buffer. The validation was done in both the normal and shear directions. It was found that the numerical model was able to replicate the dynamics of the rubber buffer very well using the same loading conditions as in the experiments.

Appendix B

B. Calibration of the Displacement Data from the Dynamic Analysis

Apparatus:

1. Vibratory screen
2. 2x metal plates
3. CoCo-80X Dynamic signal analyser
4. Keyence Laser Displacement Transducer
5. Tripod

During the experiments, a large amount of accelerometer data was gathered this data needed to be double integrated to get displacements. It was expected that the accelerometer data would have some form of a DC offset when double integrated it was thus best to integrate in the frequency domain. It was also necessary to bandpass filter the signal to eliminate any external noise from experiments happening around the labs.

To ensure that the integration and filtering of the data was done correctly, and that no critical information was lost in the process it was necessary to validate the displacement data from the system. The validation of the displacement data was done by measuring the displacement of the screen and comparing this result to the integrated displacement. The displacement measurement was done using a laser displacement transducer.

Two sets of readings were conducted using the displacement transducer the first was with two of the steel plates on the deck of the vibratory screen and the second with the screen unmodified. Readings were measured in the Y direction and on the front side of the screen. The measurements were taken at the two locations on the plates above the rubber buffers. The experimental setup is show in figure B-1.

The procedure used for conducting the dynamic analysis on the vibratory screen with laser displacement transducer is as follows:

1. Place 1 metal plate in the middle of the screen and 1 metal plate at the discharge side of the screen and secure the plates to the screen using ropes.
2. Prepare the surface were the laser transducer laser will shine to ensure accurate results.
3. Secure the laser transducer by attaching it using a clamp to the tripod stand.

4. Ensure that the height of the laser transducer is 80mm above the measurement surface by lifting or lowering the location of the clamp.
5. Click record on the CoCo.
6. Switch on the screen.
7. Once the timer on the CoCo has reached 2 minutes turn the screen off at the wall.
8. Wait for the screen to entirely stop, this can be monitored on the display on the CoCo.
9. Once the screen has completely stopped save the data from the simulation.
10. Complete steps 2 to 8 for the two corners on the front side of the screen.
11. Once the data has been saved for the corners the next step is to remove the weights from the screen and perform the steps 2 to 10 again on the screen in its default configuration.

Figure 6 B-1 Experimental setup of the laser displacement transducer.

Calibration of the laser displacement transducer:

Apparatus:

1. CoCo-80X Dynamic signal analyser
2. Keyence Laser Displacement Transducer
3. Ruler
4. Fixed surface

Once the results were collected the next step was to calibrate the laser transducer. The calibration of the laser transducer was necessary as the output of the transducer was measured in volts as opposed to millimetres. It is noted that the maximum displacement that the laser displacement transducer can measure is ± 25mm from the neutral plane. The experimental setup of the calibration is shown in figure B-2.

The calibration of the laser transducer was done on a flat surface and pointing the laser at an object a known distance away. By repeating this procedure for several different known distances, a relationship between the voltage and the displacement was generated.

Figure 6 B-2 Experimental setup for the calibration of the laser displacement transducer.

The procedure used for conducting the dynamic analysis on the vibratory screen with laser displacement transducer is as follows:

1. Place the fixed surface of which will be used as the base from which the distance will be measured at the end of the ruler.
2. Set the laser transducer 85mm away from the fixed surface and take the base voltage reading from the CoCo.
3. Repeat the test by taking readings by moving the laser transducer closer to the plate by 3-5mm.
4. Continue taking readings moving the laser transducer closer to the fixed surface until the distance between the laser transducer and the fixed plate is 55mm.

Appendix C

C. Correlation of the Results from the Experimental and FEM Modal Analysis

This section covers the comparison of the FEM modal results with the experimental modal results. This was done to ensure that the results from the FEM modal analysis correlate with the results from the experimental modal analysis. This was done by comparing the modal frequencies and the modal shapes of the FEM model with the experimental results.

The comparison was done by plotting the responses from the experimental modal analysis for the different accelerometer and modal hammer impact locations. The validation was done by analysing which accelerometer and modal hammer impact locations resulted in a spike in the FRF. The FRF functions were plotted and the peaks were compared.

This approach was done for the 6 rigid body modes from the modal analysis, as it was too complicated to compare the rigid body modes by simply using the experimental modal analysis.

The section below is an example of the procedure followed to confirm the correlation of the mode shapes. This was done for all 6 rigid body modes. In conclusion it was found that all the rigid body modes and mode shapes correlated well between the FEM and the experimental results.

Mode 1

The first mode as found from the FEM model was a rigid body mode along the Z-axis with a frequency of 3.85Hz. It was thus expected that the first mode would show up in the physical modal analysis in the Z-direction. It was also expected from the mode shape from the FEM model that there would be some mode shape movement in the Y-axis.

Each of the different accelerometer locations as well as each of the different modal hammer impact locations were investigated. This was done by investigating all the frequency response functions in each of the three directions.

It was found that the mode shape produced by the FEM model and the experimental results are the same. The resonant frequency determined form the modal analysis in the Z-direction is 2.2Hz. There was a small discrepancy between the modal frequencies between the FEM model and that of the modal analysis.

Some of the key accelerometer directions will now be investigated in order to validate the direction and the frequency of the first mode.

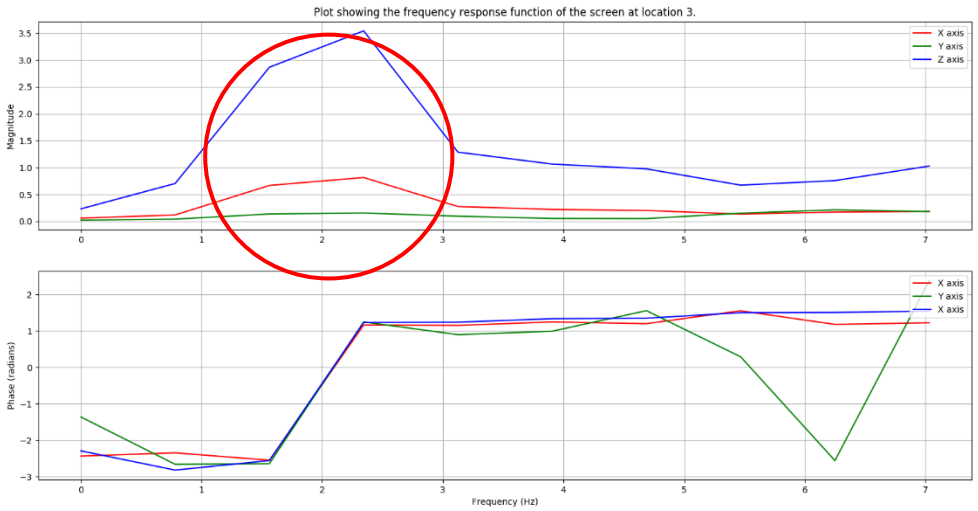

Figure 6 C-1 Plot showing the FRF of the vibratory screen when the accelerometer was at location 3 and the modal hammer impact in the Z direction just below the accelerometer.

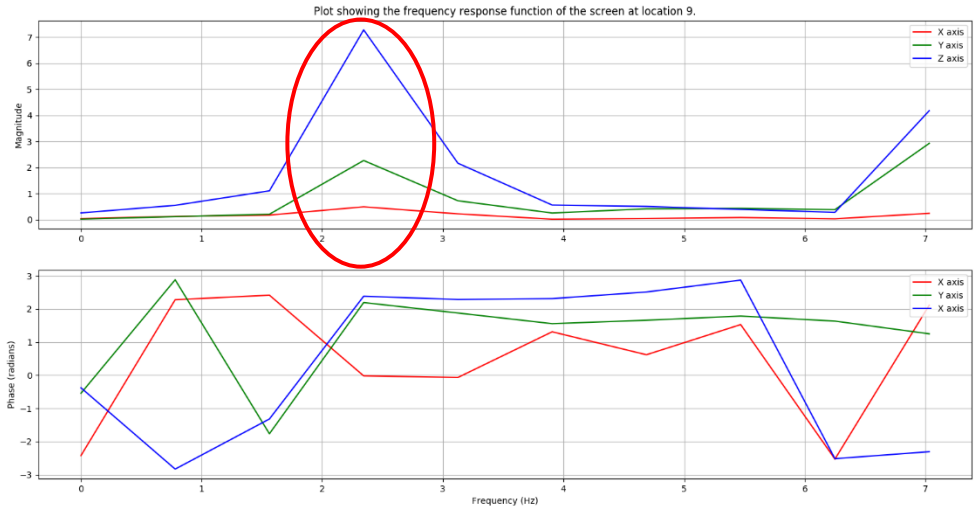

Figure 6 C-2 Plot showing the FRF of the vibratory screen when the accelerometer was at location 9 and the modal hammer impact in the Z direction directly above the accelerometer.

Discussion

By analysing all the FRF produced by the modal analysis for the first modal frequency. It was found that the first mode shape was a rigid body translational mode along the Z direction. Figures C-1 and C-2 are some of the most relevant figures in proving the nature of the mode shape. By looking at figure C-1 and C-2 the FRF has a spike at a frequency of 2.2Hz in the Z direction. There is also a phase change associated with the peak in the FRF as well.

N

One aspect seen was that a peak in the Z direction on the FRF was often associated with a modal hammer impact in the Z direction this is seen in figures C-1 and C-2. This was expected as more energy was applied into the mode by a modal hammer impact in the direction of the mode.